3-D Optical Waveguide Arrays for In-Vivo Optogenetics: Development and Application

by

Anthony N. Zorzos

S.M., Department of Aeronautics and Astronautics, Massachusetts Institute of Technology, 2009
Sc.B., Applied Physics, Brown University, 2007

Submitted to the Program in Media Arts and Sciences, School of Architecture and Planning, in partial fulfillment of the requirements for the degree of

Doctor of Philosophy in Media Arts and Sciences

at the

MASSACHUSETTS INSTITUTE OF TECHNOLOGY
June 2013

Author _____

Anthony N. Zorzos
Program in Media Arts and Sciences
May, 2013

Certified by _____

Prof. Edward S. Boyden
Leader, Synthetic Neurobiology Group
Associate Professor, MIT Media Lab and McGovern Institute,
Departments of Biological Engineering and Brain and Cognitive Sciences

Accepted by _____

Prof. Patricia Maes
Associate Academic Head
Program in Media Arts and Sciences

3-D Optical Waveguide Arrays for In-Vivo Optogenetics: Development and Application

by

Anthony N. Zorzos

Submitted to the Program in Media Arts and Sciences, School of Architecture and Planning, on May 24, 2013, in partial fulfillment of the requirements for the degree of Doctor of Philosophy in Media Arts and Sciences

Abstract

A key feature of neural circuits in the mammalian brain is their 3-dimensional geometric complexity. The ability to optically drive or silence sets of neurons distributed throughout complexly shaped brain circuits, in a temporally precise fashion, would enable analysis of how sets of neurons in different parts of the circuit work together to achieve specific neural codes, circuit dynamics, and behaviors. It could also enable new prototype neural control prosthetics capable of entering information into the brain in a high-bandwidth, cell-specific fashion. This dissertation work involves the development, characterization, and initial utilization of a technology capable of delivering patterned light to 3D targets in neural tissue.

Silicon oxynitride waveguide fabrication was optimized for integration onto insertable silicon probes. The waveguides have a propagation loss of ~0.4 dB/cm. Right-angle corner mirrors were fabricated at the outputs of the waveguides with losses measured to be 1.5 ± 0.4 dB.

Silicon MEMS techniques were developed to fabricate both single- and multi-shank probe geometries with integrated waveguides. Methods were developed to assemble the multi-shank probes into a 3D format using discrete monolithic silicon pieces.

Three coupling schemes were developed to couple light to both single- and multi-shank probes. For individual probes not assembled in a 3D format, ribbon cables were used. Modular connection schemes were developed based on ribbon cable connector technologies. Input coupling losses were measured to be 3.4 ± 2.2 dB. For probes which were assembled in a 3D format, two coupling methods were developed: projector-based and scanning-mirror-based. The losses associated with the projector-based system are 17.3 ± 1.8 dB. With a 1.5W 473 nm laser source, 100 μW is capable of being delivered from 300 separate waveguides. The losses associated with the scanning-mirror-based system are 11.9 ± 2.5 dB. With a 1.6 mW 473 nm laser source, 100 μW is capable of being delivered from an individual waveguide.

These fabrication, assembly, and coupling methods demonstrate a successful development of a technology capable of delivering patterned light to 3D targets in neural tissue. Initial biological experiments being performed on microbial-opsin expressing mice is presented. 3D patterned light is delivered to targets in the primary somatosensory cortex while electrical activity is recorded from the primary motor cortex.

Thesis Supervisor: Professor Edward S. Boyden
Title: Associate Professor, MIT Media Lab and McGovern Institute, Departments of Biological Engineering and Brain and Cognitive Sciences

3-D Optical Waveguide Arrays for In-Vivo Optogenetics: Development and Application

by

Anthony N. Zorzos

The following people will serve as readers for this thesis:

Thesis
Reader_____

Clifton G. Fonstad
Leader, Compound Semiconductor Research Group
Vitesse Professor of Electrical Engineering

Thesis
Reader_____

Ramesh Raskar
Leader, Camera Culture Group
Associate Professor of Media Arts and Sciences

Acknowledgements

I would like to take this space to acknowledge and thank all the people who have been such help and support over my time as a doctoral student.

First, I'd like to thank Professor Raskar for agreeing to be a committee member and thesis reader. He has provided very helpful feedback during the project development and the writing of this dissertation. Furthermore, in interacting with him and his students over the last few years on separate projects has proven very beneficial. Next, I'd like to thank all the members of the Boyden Lab. They have proven to not only be excellent resources for knowledge and support, but also a fun group to spend time with.

I'd also like to acknowledge all the help and support I've gotten over the years from the MTL research staff. I'd especially like to mention Dennis Ward, Kurt Broderick, Donal Jameison, Eric Lim, Paudely Zamora, Paul Tierney, and Vicky Diadiuk. They all drilled into me a practical and theoretical understanding of micro-fabrication methods, and for that I am deeply grateful.

There are three labmates I'd like to select out as having been especially supportive and helpful. First, to Dr. Justin Kinney I'd like to say it would be *haaaardaaaa* to find someone so able to balance intellectual brilliance, clarifying lucidity, and such a vulgar sense of humor: thank you. Next, to the intellectual heavy-weight Dr. Tim Buschman I'd like to say you have given me a first-hand glimpse into the world of neuroscience and the most sublimely humorous form of egotism: thank you. Finally, to Dr. Jorg Scholvin, you

have been more a mentor and guide than a labmate, and are brilliant enough to have made me feel like an idiot for three straight years: thank you. To all three of you: thank you.

The most important two figures during my time as a PhD student have been my co-advisors Professor Fonstad and Professor Boyden. I cannot thank you enough for your generosity, your time, your brilliance, your patience, your kindness, and your guidance. I feel deeply honored to have been so closely followed by such outstanding advisors. I have learned so very much over the last four years and look forward to maintaining our relationship for years to come. More importantly than passing to me intellectual material, you have been ideal role-models for character and conduct both as academics and human beings.

Finally, I want to thank a few close friends who have truly helped me over the years: Dan Courtney, Paulo Lozano, John Churchill, Chad Gilette, Josh Bartok, and Lama Willa Miller: thank you, thank you, thank you! My Smakula in-laws, my cousins, my aunts, my uncles, my Yiayia and Pappou. My sister, her husband, and my dearest, dearest nephew Stevie. To my parents, Steven and Pauline Zorzos, the father and the mother, the fire and the anvil, the upward and the downward, the outward and the inward, the becoming and the being, the freedom and the fullness: thank you!

Most importantly, I want express my Gratitude and Love for my wife, Kathleen Zorzos: you are my Heart.

Contents

Chapter 1: Introduction

1.1 Background

This doctoral work is motivated by a fundamental question in systems neuroscience: how do sets of neurons in different parts of the brain work together to achieve specific neural codes, circuit dynamics, and behaviors? The scale of modern research addressing this single general question is large (Buzsáki, 2006; Engel, Fries, & Singer, 2001; Miller & Buschman, 2013; Rieke, 1997). This dissertation provides a particular tool representing a contribution to systems neuroscience, whereby large-scale optogenetic 3D neural mapping becomes a possibility. Furthermore, this dissertation will extend beyond the development of the technology into its *preliminary* scientific utilization for mapping large-scale cortical networks.

Systems neuroscience is the study of how neural networks communicate and give rise to neural dynamics and behavior. The brain has a large number of neurons (~75 million

in a mouse, ~2 billion in a chimpanzee, and ~85 billion in a human) (Kandel, 2012). The complexity of these systems, directly related to the scale of the neural networks studied, is large. It is desirable, in approaching such a complex problem, to be equipped with the necessary technologies capable of teasing out the dynamics and relationships arising within said networks.

There are many different types of neural technologies, i.e. technologies seeking to address fundamental neuroscientific questions as well as potentially treat neuropathologies, (DiLorenzo & Bronzino, 2008; Frontiers Research Foundation., 2008; Katz, 2008; Maurits, 2012; Michael & Borland, 2007). These technologies include electrophysiological technologies (e.g. microelectrode arrays, patch clamping, etc.), neural imaging technologies (e.g. functional magnetic resonance imaging, magneto encephalography, etc.), drug delivery techniques technologies, etc.

This thesis develops a technology capable of affecting neural activity with resolution in space (i.e. many points in a volume of tissue), time (i.e. fast temporal dynamics), polarity (i.e. activate or deactivate neurons), and type (i.e. address different classes of neurons independently). The new field of optogenetics provides an optimal platform from which to develop such a technology.

Optogenetics enables the ability to delivery light into the brain for the purposes of controlling neural activity and other biological processes. As the name suggests, optogenetics involves the genetic manipulation of neural tissue so that it is subsequently made light-sensitive (i.e. can be controlled on the millisecond timescale with photonic stimulation). This is accomplished by introducing light-activated channels that allow for the

precise activation or deactivation of cellular activity. Cell-type resolution is accomplished through the use of specific targeting mechanisms. The microbial opsins most commonly used are channelrhodopsins (Boyden, Zhang, Bamberg, Nagel, & Deisseroth, 2005), halorhodopsins (Han & Boyden, 2007; F. Zhang, Wang, et al., 2007), and archaerhodopsins (Chow et al., 2010; Han et al., 2011). See Figure 1.

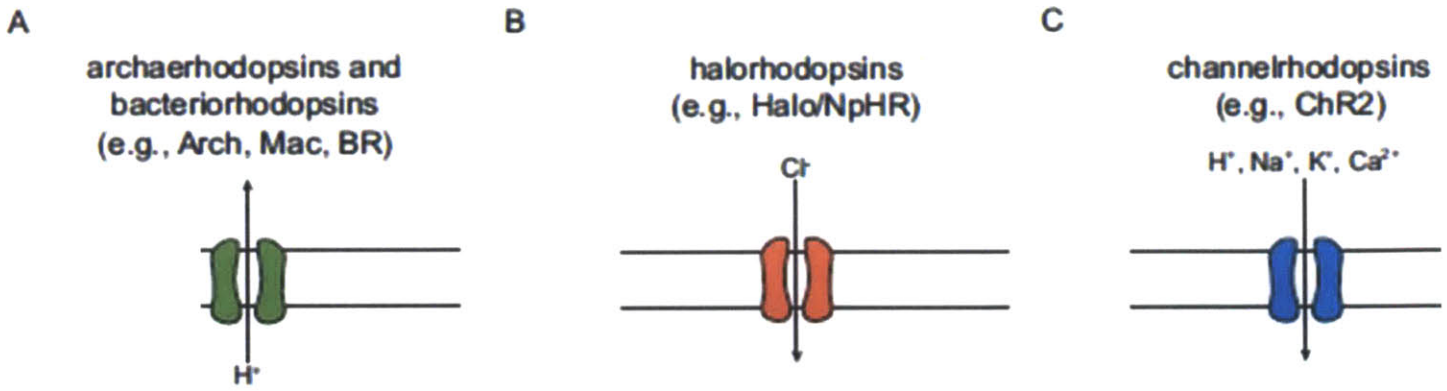

Figure 1 – (A) The archaerhodopsins and bacteriorhodopsins are light-driven outward proton pumps. (B) The halorhodopsins are light-driven inward chloride pumps. (C) The channelrhodopsins are light-gated inward nonspecific cation channels. Adapted from (Boyden, 2011)

As shown in Figure 1, the channelrhodopsins are light-gated inward nonspecific cation channels, the halorhodopsins are light-driven inward chloride pumps, and the archaerhodopsins/bacteriorhodopsins are light-driven outward proton pumps. Getting these microbial opsins to express in the cell membrane is an area of active research and development in molecular biology (Madisen et al., 2012). Strategies have largely involved cell-specific promoters and customized viruses for genetic targeting. There is also a growing use of germline transgenesis for permanent gene transfer. These 'transgenic mice', as they will be referred to throughout this work, avoid many of the costs and difficulties

associated with using viruses for opsin expression. Both expression methods are used in this work.

Structured illumination across the 2D surface of cortex has been used previously (Sakai, Ueno, Ishizuka, & Yawo, 2013) (Figure 2). As powerful as this approach may be, it is inherently limited by the 2D nature of the light delivery. Deep neural targets are impossible to reach given the opacity and optical properties of brain tissue (Johansson, 2010).

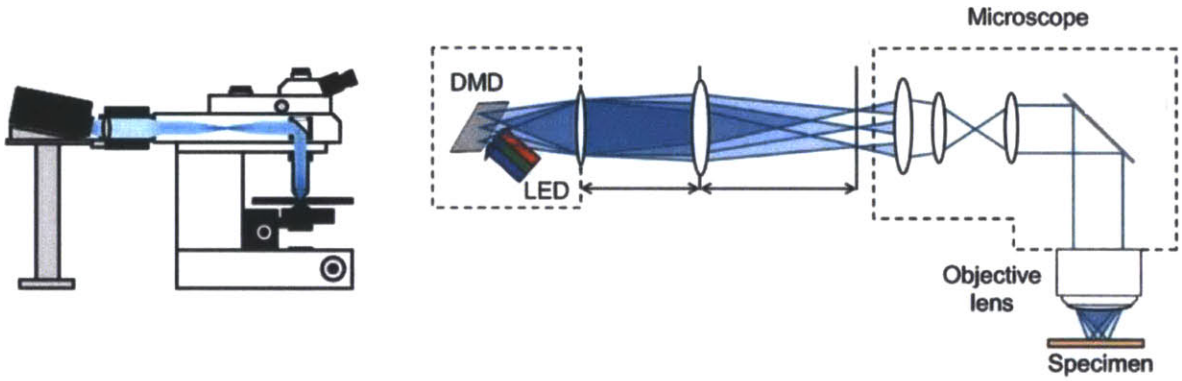

Figure 2 – DMD-based projector system used to project arbitrary 2D geometries onto cortex surface (Sakai et al., 2013). The LED is a light emitting diode array for DMD (digital micromirror device) illumination. The DMD is used to sculpt the light in arbitrary 2D patterns to be projected.

There is also work being done on adapting the technology of two-photon microscopy to optogenetics for stimulation at-depth (Oron, Papagiakoumou, Anselmi, & Emiliani, 2012). Two-photon microscopy, relying on two-photon absorption by fluorophores, is an imaging technique used to image tissue at depth. In adapting this technology for optogenetics, stimulation with depth resolution is possible. However, there are some inherent limitations to this technology. Because of scattering and absorption properties of neural tissue, it is

limited to a depth of ~ 1 mm. Although it can be used to illuminate different regions of a 3D space, it cannot provide illumination to arbitrary 3D geometries.

To date, numerous *in vivo* studies have used optical fibers to deliver visible light into brain targets in which neurons express opsins, but an optical fiber can target just a single region (Figure 3). Beyond simple light delivery, individual optical fibers have been adopted to use in complex behavioral experiments (Aravanis et al., 2007; Gradinaru, Mogri, Thompson, Henderson, & Deisseroth, 2009). Technologies have also been developed to avoid the use of optical fiber tethering altogether using wireless LED sources (Wentz et al., 2011). An implantable probe capable of delivering light to arbitrary points in a 3-dimensional volume would enable more versatile optical control, opening up the ability to deliver patterned light to manipulate neural activity in distributed brain circuits.

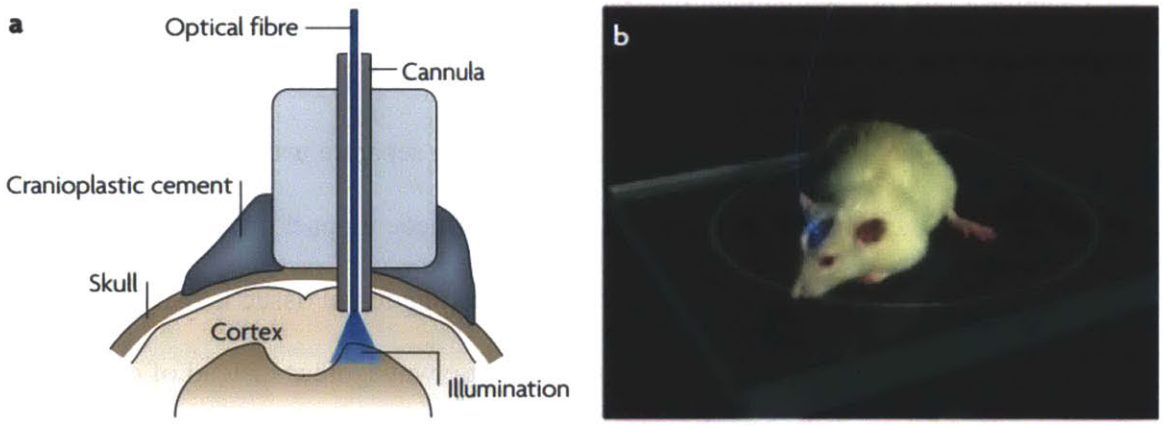

Figure 3 – The majority of optogenetics experiments to-date have involved single optical-fiber stimulation, adapted from (F. Zhang, Aravanis, Adamantidis, de Lecea, & Deisseroth, 2007). (a) is a schematic of a how a single optical fiber is usually implanted and attached to the skull. (b) shows a mouse, freely-moving, with a single optical fiber implanted.

Although a natural first step for optogenetics-based experiments, individual fibers do not allow for easily scaling to hundreds/thousands of individual delivery sites. This dissertation does not move away from the fundamental technology of fiber-optics, but utilizes the developments of integrated photonics and on-chip waveguide fabrication as a framework for fiber-optic miniaturization and scaling.

1.2 Overview

This dissertation presents and characterizes a technology, based on the advancements of integrated photonics, allowing for the delivery of illumination to arbitrary 3D geometries in brain tissue. Light is coupled from an external source to fiber optics which terminate at different depths along an array of implantable shanks.

Chapter 2 will present general theoretical considerations behind the technology. Specifically, the theory behind optical waveguides is presented, for both single-mode and multi-mode fiber optics. The coupling efficiency between separate waveguides is presented. Evanescent coupling and micro-bending loss, largely influencing packing density (of waveguides), is also discussed. Finally, the issue of heating neural tissue is discussed, an important theoretical consideration when choosing to use waveguides instead of direct source implantation.

In Chapter 3, the process of waveguide fabrication is presented. The waveguide loss characterization is shown and the different mechanisms discussed. The characterization allows for the fabrication of single-shank and multi-shank waveguide probes with minimal

size and subsequent tissue damage. These single- and multi-shank probe geometries are shown and characterized.

Chapter 4 describes the fabrication procedure and methods used to assemble multi-shank probes into full 3D probe arrays. The chapter also offers a characterization of how these assembly methods affect the geometrical alignment of the multi-shank probes.

Chapter 5 is a description of the different coupling methods used for the 3D probe arrays: a DMD-based system and a scanning galvanometer-based system. The loss mechanisms of the two systems are characterized, and a critique of the two systems is offered based on the performance results.

Chapter 6 is a conclusion chapter. This chapter both summarizes the developed technology and its performance, as well as provides an in-depth description as to how this technology can be improved and where it can lead to in terms of new research avenues. There is also a discussion of preliminary biological experiments being conducted.

Appendix A is a detailed process flow for the fabrication of on-chip waveguides. Appendix B is a detailed process flow for the fabrication of light-proof electrodes. Appendix C is the standard operating procedure for preliminary biological experiments. Appendix D is a description of work done on light-proof electrodes.

Chapter 2: Theoretical Considerations

The developed technology maintains the light source outside of the neural tissue (to mitigate heating issues) and guides the light along waveguides to deep neural targets. In this chapter, the basic theory of waveguide operation is developed and discussed, with emphasis given to planar dielectric waveguides. First fiber optics in general will be discussed. Then, planar dielectric waveguides followed by an extension to two-dimensional waveguides. Following this, the coupling efficiencies, propagation losses, micro-bending losses, and heating will be discussed. Heating of neural tissue is a particularly important consideration and the discussion in this chapter will clearly and quantitatively explain why optical waveguide were pursued in favor of direct illumination source implantation.

2.1 Fiber Optics

2.1.1 Electromagnetic Theory

Optical waveguides can be categorized by several classifiers: mode structure (single-mode, multi-mode), index profile (step, gradient), geometry (slab, strip, fiber), and material (glass, polymer, semiconductor). This section will seek to develop the theory behind a fiber-based geometry. Fiber waveguides are usually cylindrical in geometry (Figure 4) and are composed of a dielectric central core surrounded by an outer cladding. The core dielectric has a higher index of refraction relative to the cladding material. Speaking from a perspective of ray-based optics, light incident on the core/cladding boundary at angles greater than the critical angle (to be defined below) are totally internally reflected, and therefore 'guided' by the fiber. In the interest of completeness, this discussion of fiber optics will begin with a wave-based perspective and then lead us into the ray-based perspective when dealing with planar waveguides.

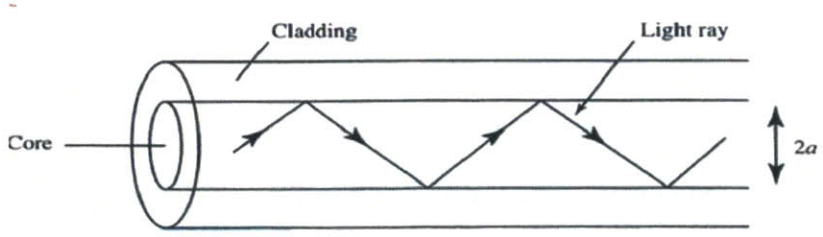

Figure 4 – Cylindrical dielectric step index waveguide, where 2a is the core diameter. (PhotonicsOnline)

Let us begin with the most generalized form (free space) of Maxwell's Equations,

$$\nabla \times H = \varepsilon_0 \frac{\partial E}{\partial t}$$

$$\nabla \times E = -\mu_0 \frac{\partial H}{\partial t}$$

$$\nabla \cdot E = 0$$

$$\nabla \cdot H = 0,$$

where E and H are the electric field and magnetic field respectively, and the constants ε_0 and μ_0 are the electric permittivity and magnetic permeability respectively. The electric field and magnetic field, forming an electromagnetic wave, must satisfy the above coupled set of differential equations. For E and H to satisfy Maxwell's equations, it is necessary that each of their components (E_x, E_y, E_z, H_x, H_y, H_z) satisfy the wave equation,

$$\Delta^2 u - \frac{1}{{c_0}^2} \frac{\partial^2 u}{\partial t^2},$$

where

$$c_0 = \frac{1}{\sqrt{\varepsilon_0 \mu_0}}$$

is the speed of light in vacuum. As mentioned, this set of coupled differential equations govern electromagnetic waves in free-space. Dielectric waveguides involve the propagation of light in a medium, so Maxwell's equations must be adjusted accordingly. Maxwell's equations in a medium (source-free) become,

$$\nabla \times H = \frac{\partial D}{\partial t}$$

$$\nabla \times E = -\frac{\partial B}{\partial t}$$

$$\nabla \cdot D = 0$$

$$\nabla \cdot B = 0,$$

where D is the electric flux density, B is the magnetic flux density, and both depend on the properties of the medium of propagation. Specifically,

$$D = \varepsilon_0 E + P$$

$$B = \mu_0 H + \mu_0 M$$

where P is the polarization density (expressing the density of electric dipole moments in a dielectric material) and M is the magnetization density (expressing the density of magnetic dipole moments in a magnetic material). The magnetization density can be assumed for this discussion to be zero, as any and all media addressed here are non-magnetic. If we assume a time-harmonic field with time dependence $e^{-j\omega t}$, where $\omega=2\pi\nu$ is the angular frequency, then Maxwell's equations become,

$$\nabla \times H = j\omega D$$

$$\nabla \times E = -j\omega B$$

$$\nabla \cdot D = 0$$

$$\nabla \cdot B = 0.$$

The time-harmonic field with time dependence is a safe assumption given the condition that the electromagnetic wave under analysis is monochromatic. For the purposes of this work,

the simplest case to consider (linear, nondispersive, homogeneous, and isotropic media) will be sufficient. Given this case, the vectors P and E are related as,

$$P = \varepsilon_0 \chi E,$$

where χ is the electric susceptibility. We can then relate D and E as $D = \varepsilon E$, where $\varepsilon = \varepsilon_0(1 + \chi)$ is the electric permittivity of the medium. With $D = \varepsilon E$ and $B = \mu_0$, Maxwell's equations can finally be written as,

$$\nabla \times H = j\omega\epsilon E$$

$$\nabla \times E = -j\omega\mu_0 H$$

$$\nabla \cdot E = 0$$

$$\nabla \cdot H = 0.$$

Because E and H satisfy the wave equation (above), all components of E and H (represented by $U(r)$) must satisfy the Helmholtz equation,

$$\nabla^2 U + k^2 U = 0,$$

where $k = \omega\sqrt{\varepsilon\mu_0} = nk_0$, n is the refractive index, and $k_0 = w/c_0$.

Using this developed electromagnetic theory, we can now look at how monochromatic light propagates in step-index fibers. As shown previously, each of the electric field and magnetic field components must satisfy the Helmholtz equation, where $n=n_1$ in the core and the index of refraction is n_2 in cladding (Figure 5). The cladding thickness is assumed to be of infinite extent. In a cylindrical coordinate system, the Helmholtz equation becomes,

$$\frac{\partial^2 U}{\partial r^2}+\frac{1}{r}\frac{\partial U}{\partial r}+\frac{1}{r^2}\frac{\partial^2 U}{\partial \varphi^2}+\frac{\partial^2 U}{\partial z^2}+n^2{k_0}^2U=0$$

The solutions to this equation will take the form of waves traveling in the z direction with propagation constant β.

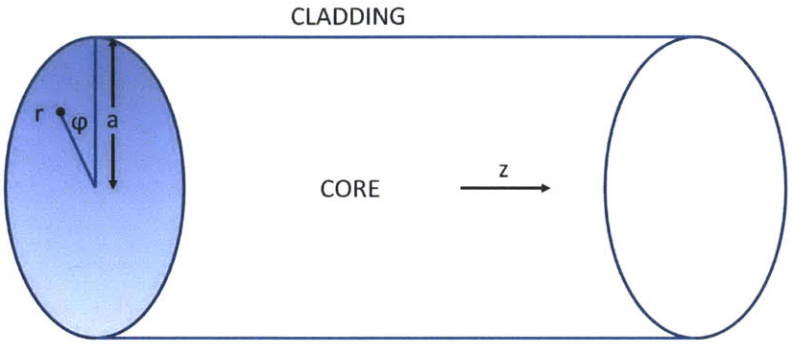

Figure 5 - Basic schematic of fiber showing geometric parameters. The cladding is taken as infinite in extent.

U must be a periodic function in φ, so we can substitute the separated equation,

$$U(r,\varphi,z)=u(r)e^{-jl\varphi}e^{-j\beta z},\ \ l=0,\pm1,\pm2,....$$

into the above cylindrical-form of the Helmholtz equation to get the following ordinary differential equation for *u(r)*,

$$\frac{d^2u}{dr^2}+\frac{1}{r}\frac{du}{dr}+\left(n^2{k_0}^2-\beta^2-\frac{l^2}{r^2}\right)u=0.$$

The wave is bound (or guided) by the fiber if the propagation constant, β, is less than the core wave-number (n_1k_0). However, depending on the propagation constant and material wave-number, two separate equations can be written for the core and cladding,

$$\frac{d^2u}{dr^2}+\frac{1}{r}\frac{du}{dr}+\left({k_T}^2-\frac{l^2}{r^2}\right)u=0,\ \ r<a\ (core)$$

$$\frac{d^2u}{dr^2}+\frac{1}{r}\frac{du}{dr}-\left(\gamma^2+\frac{l^2}{r^2}\right)u=0,\ \ r>a\ (cladding),$$

where ${k_T}^2={n_1}^2{k_0}^2-\beta^2$, and $\gamma^2=\beta^2-{n_2}^2{k_0}^2$. For guided waves ${k_T}^2$ and γ^2 are positive and k_T and γ are real. Bessel functions are the solutions to the above differential equations. Specifically, we have,

$$u(r)\propto\begin{cases}J_l(k_Tr), & (core)\\ K_l(\gamma r), & (cladding)\end{cases}.$$

These solutions, or 'modes', represent the set of possible cross-sectional field profiles in a fiber (given the set of constraints utilized in the refinement of Maxwell's equations). The cladding solution, $K_l(\gamma r)$, a modified Bessel function of the second kind and order l, represents the evanescent penetration of the given mode into the cladding (Figure 6).

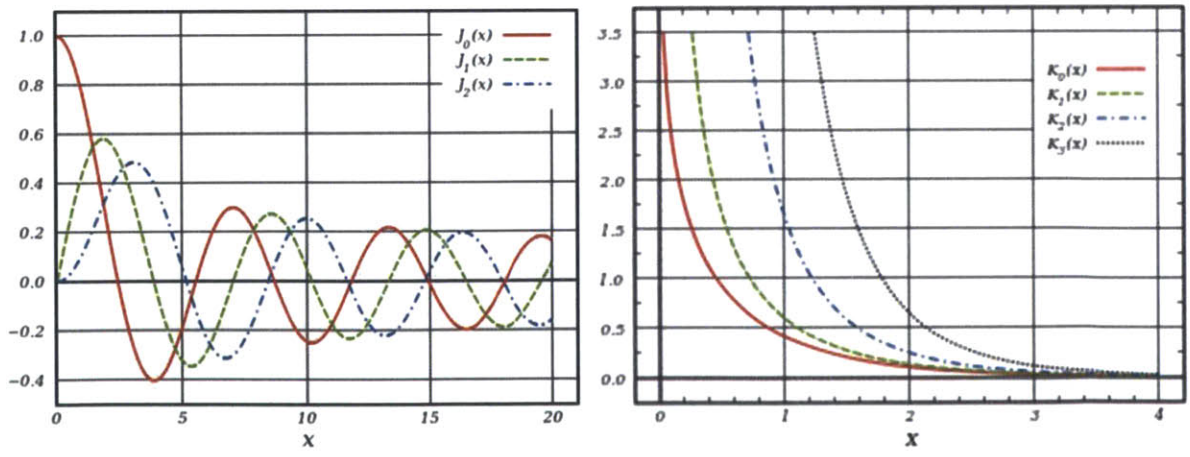

Figure 6 – Solutions to the Helmholtz equation for both the core (left) and cladding (right). The solution for the core is a Bessel function of the first kind, and the solution for the cladding is a modified Bessel function of the second kind. The different orders for each solution represent different modes for the fiber.

If we normalize the parameters k_T and γ by the fiber core radius, a, then we can define what is known as the V-number,

$$V^2 \equiv a^2\left({k_T}^2 + \gamma^2\right).$$

Plugging in the defined values of k_T and γ, we see that V is a conserved quantity,

$$V = 2\pi\frac{a}{\lambda_0}({n_1}^2 - {n_2}^2)^{1/2} = 2\pi\frac{a}{\lambda_0}NA.$$

This is an important parameter to define in classifying a fiber as single-mode or multi-mode, a consideration which we will return to later in this work. Recalling the substituted relation for the components of E and H,

$$U(r,\varphi,z) = u(r)e^{-jm\varphi}e^{-j\beta z},\ \ m = 0,\pm1,\pm2,\ldots.,l = 0,\pm1,\pm2,\ldots.$$

we now have a spatial profile, for any given location z, in terms of r and ϕ. The different modes are usually denoted LP_{lm}. A graphic showing a small number of the different modes and their corresponding amplitude profiles (for a fiber with a V-number of ~12) is shown in Figure 7 below (Paschotta, 2011).

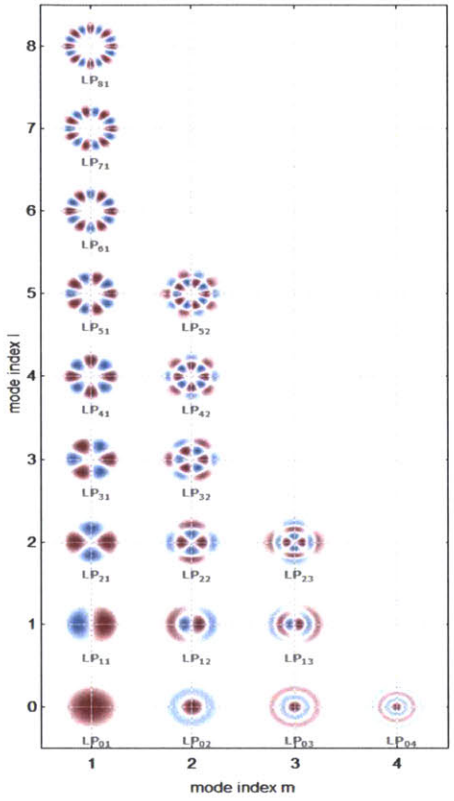

Figure 7 - LP modes for a step-index cylindrical optical fiber (Paschotta, 2011). The different colors represent different polarity electric field solutions. How many modes are supported by an individual optical fiber depends on the light wavelength and fiber characteristics (size and indices of core and cladding).

How many modes are supported by an individual optical fiber depends on the wavelength of interest and fiber characteristics (size and refractive indices of core and cladding respectively). This is reflected in the V-number defined above. Note that there are discrete modes, i.e. not a continuum of solutions, because the eigen-solutions to the Helmholtz equation are discrete (above).

2.1.2 Ray-Based Theory

Now that a basic wave and electromagnetics-based understanding and theory of fiber optics have been established, the more specific case of planar dielectric waveguides can be addressed. Because planar waveguides, defined by their geometry, do not have a rotational symmetry like fiber waveguides (cylindrical), the Maxwell-based solutions are significantly more complex. It is for this reason a ray-based approach is usually utilized to derive waveguide modes, number of modes, field distributions, etc. for planar waveguides. Considering first a 2-D condensation (slab waveguide) of the 3-D general case, we first look at the internal field distribution (the field distribution in the core material (Figure 8)).

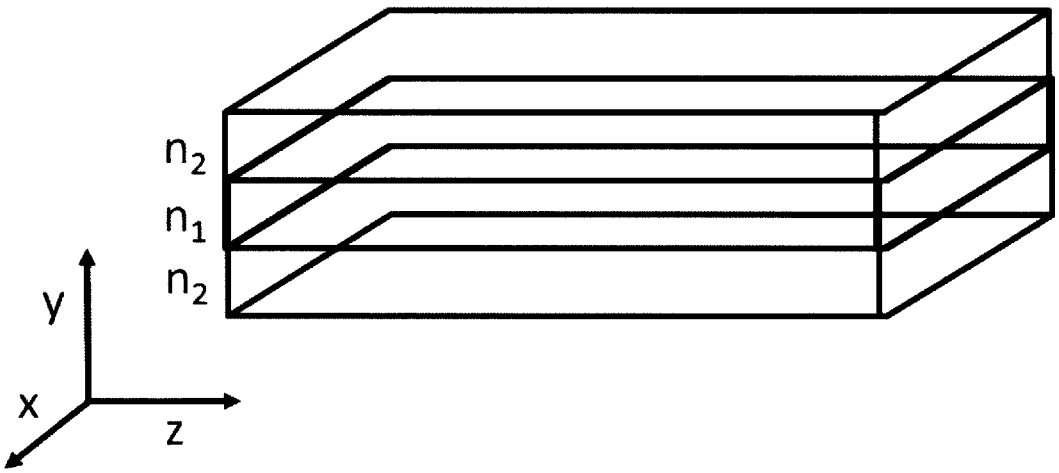

Figure 8 - Slab dielectric waveguide with two separate refractive indices.

As the more-fundamental and complete electromagnetics discussion has already been made with regards to cylindrical fiber optics (above), we can here skip the detailed ray-based and less fundamental derivation of the transverse electric-field amplitude (Saleh & Teich, 2007),

$E_x(y,z) = a_m u_m(y) \exp(-j\beta z)$, where $\beta_m = n_1 k_0 \cos\theta_m$ is the propagation constant (as before), a_m is a constant,

$$u_m(y) \propto \begin{cases} \cos\left(\frac{2\pi \sin\theta_m}{\lambda} y\right), m = 0,2,4,\ldots \\ \sin\left(\frac{2\pi \sin\theta_m}{\lambda} y\right), m = 1,3,5,\ldots \end{cases} \quad -\frac{d}{2} \leq y \leq \frac{d}{2},$$

and $\lambda=\lambda_0/n_1$. In the derivation of this transverse field, θ_m is the angle of the TEM plane wave incident in the slab waveguide. As with the electromagnetics-based derivation, there are discrete solutions reflecting discrete modes. In this ray-based derivation, the included solutions are those which do not result in the necessary path lengths for destructive interference (Kasap, 2013). For the external field (the field distribution in the cladding), we have,

$$u_m(y) \propto \begin{cases} e^{-\gamma_m y}, y > \frac{d}{2} \\ e^{-\gamma_m y}, y > \frac{d}{2} \end{cases}$$

The extinction coefficient, γ_m, can be defined as,

$$\gamma_m = n_2 k_0 \sqrt{\frac{cos^2\theta_m}{cos^2\theta_c} - 1},$$

where θ_c, is the critical angle.

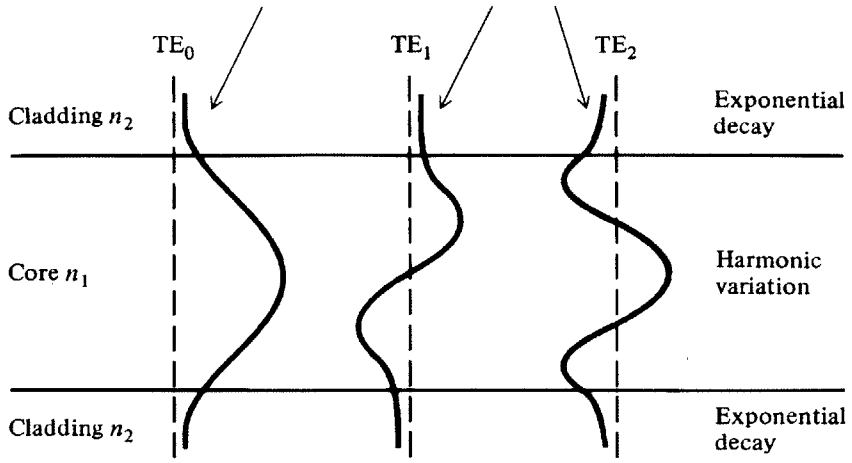

Figure 9 – Transverse electric-field amplitude for several 1D dielectric slab waveguide modes (Keiser, 2011).

As with the electromagnetics-based derivation for a cylindrical optical fiber, the number of modes possible depends on the numerical aperture, the wavelength, and the size of the fiber. Increasing the core radius or refractive index increases the number of modes, while increasing the wavelength or cladding refractive index lowers the number of modes. As the number of possible modes drops to 1, the optical waveguide becomes a single-mode fiber, i.e. it can only sustain the fundamental mode. For instance, by decreasing the core radius, the number of modes decreases. At some radius, only the fundamental mode can be sustained. The core can be decreased in size even further while sustaining the fundamental mode, however the evanescent penetration will increase in the cladding.

Note that as the mode number, m, increases, the extinction coefficient decreases, yielding an evanescent wave with longer spatial penetration into the cladding. This is important to keep in mind when we design the waveguide as we are trying to keep optical

confinement to a maximum and want to avoid evanescent coupling (into either the substrate or neighboring waveguides).

2.1.3 Coupling

There are many methods for coupling light to a waveguide, either from a light source or another waveguide (Hunsperger, 1991). These methods include free-space coupling, butt-coupling, and diffraction-coupling, to name a few (Figure 10).

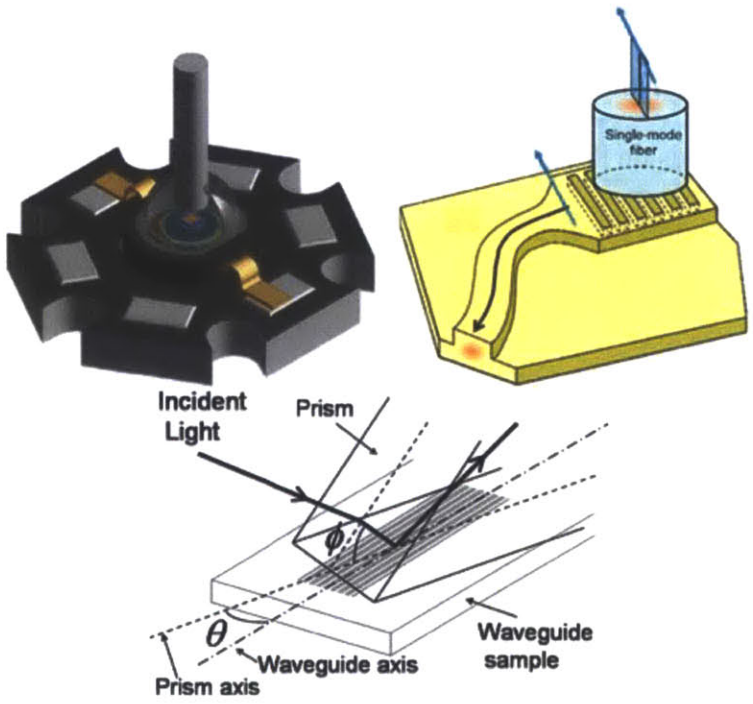

Figure 10 – Examples of various coupling methods: butt coupling (upper left), diffraction coupling (upper right), and prism coupling (bottom).

Briefly, as has been previously discussed, the optical field spatial profile is a superposition of modes,

$$E(y,z) = \sum_m a_m u_m(y) e^{-j\beta_m z},$$

where m is representative of the mode 'number' (symbols defined in previous section). The relative composition of this superposition depends on the light source used to 'excite' each mode. We can write that for a source of arbitrary distribution, *s(y)*, the amplitude of each excited mode g, is,

$$a_g = \int_{-\infty}^{\infty} s(y) u_g(y) dy.$$

This amplitude coefficient, a_g, is representative of the 'overlap' between the source distribution and the mode of interest. As will be further described in Chapters 3 and 5, the chosen method of coupling is butt-coupling from a fiber-optic source. Furthermore, the input fiber is a single-mode fiber. Therefore, the 0^{th} mode is the primary mode being excited for the final fiber arrays, yet to be described. There is the possibility of what is known as upward mode coupling. This involves the transfer of power between modes of lower order to modes of higher order. This can occur in any number of ways, including micro-bending and scattering events. So, even though initial coupling might excite predominantly the fundamental mode, the higher modes of the fabricated fiber can still be utilized.

As was already alluded to, evanescent penetration is a potential problem in the design constraints. In the case of evanescent penetration into substrate (higher index material), that results in what is known as evanescent loss. In the case of evanescent

penetration into a neighboring waveguide (equal index to core, and, more importantly, a lower index than the cladding), that results in what is known as evanescent coupling. Even though evanescent coupling does not, theoretically, involve the loss of power, in this case it can be treated as such. This will be directly addressed in Chapter 4.

2.1.4 Bend Loss

As briefly described in the introduction, the goal of the technology developed is to deliver light laterally along the length of an insertable shank. Although not the only conceivable method, the approach taken is to redirect the propagating light 90° relative to the direction of insertion. Redirecting optical waveguides at right angles is an important area of research in integrated photonics (Espinola, Ahmad, Pizzuto, Steel, & Osgood, 2001; Lin, Lin, Chen, & Li, 2009). Specifically, the important question is how to create optical waveguides with 90° low-loss small radius-of-curvature bends. This is important because the smaller the radius of curvature (for some given allowable loss), the higher the available packing density for optical interconnects.

An intuitive analytical approach for addressing the minimum bend radius involves the *radiation caustic*. Consider the phase front of a fundamental mode propagating through a bend radius of R_b in a slab waveguide (Figure 11).

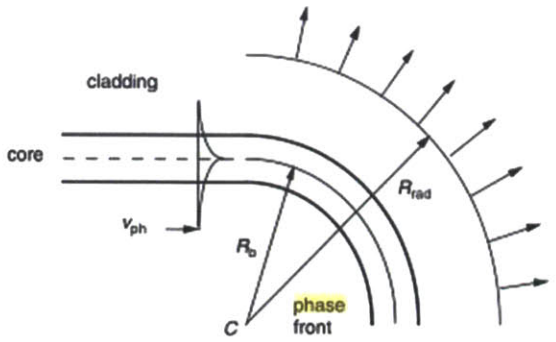

Figure 11 - Phase front for the fundamental mode in a bent slab waveguide

The angular velocity of the phase front, relative to the center (C), is taken to be Ω. The phase velocity at the beginning of the bend must be equal to the phase velocity at the end of the straight input section,

$$R_b\Omega = \frac{\omega}{\beta},$$

where ω is the frequency, and β is the propagation coefficient. Solving for Ω and substituting in for ω and β,

$$\Omega = \frac{c}{R_b n_{eff}},$$

where c is the speed of light in vacuum, and n_{eff} is the effective index of the fundamental mode. A radius, R_{rad}, is defined as the radius, relative to C, at which the phase velocity of the wave front equals the speed of light in the cladding,

$$\Omega R_{rad} = \frac{c}{n_{cl}},$$

where n_{cl} is the cladding index of refraction. Solving for R_{rad},

$$R_{rad} = \frac{n_{eff}}{n_{cl}} R_b.$$

As the phase velocity in the cladding cannot exceed the speed of light in the cladding, at R_{rad}, the penetrating evanescent tail radiates into the cladding. This interface is the *radiation caustic*. Because the evanescent tail is has an exponential decay, there is always some radiated power for any given bend radius. However, as R_b decreases, R_{rad} becomes smaller and smaller, leading to an increase in bend loss. It should also be noted that this relation also holds for higher-order modes. However, as was shown in the previous sub-section, the evanescent penetration into the cladding is larger for higher-order modes. Therefore, the bend loss is even more severe for higher-order modes. Another way of seeing this is that the effective index for higher order modes is lower, meaning R_{rad} is smaller and subsequently more bend loss. Therefore, for a given waveguide structure, the least bend loss occurs for the fundamental mode and the most bend loss occurs for the highest-order modes.

The theoretical bend loss for a given fiber optic was worked out by Dietrich Marcuse in 1976 (Marcuse, 1976),

$$\gamma = \left(\frac{\pi\rho}{R_b}\right)^{1/2} \frac{V^2 W^{1/2}}{2\rho U^2} exp\left[-\frac{4}{3}\Delta\frac{R_b}{\rho}\frac{W^3}{V^2}\right],$$

where γ is related to the bend loss by $P(z) = P(0)e^{-\gamma z}$. *P(z)* is the power at any given point along the bend, *P(0)* is the power at the beginning of the bend, z is the distance along the bend, and γ is defined above. R_b is the bend radius, ρ is the waveguide diameter (cylindrical geometry assumed), $\Delta = \frac{n_{co} - n_{cl}}{n_{co}}$, n_{co} is the core index of refraction, n_{cl} is the

cladding index of refraction, the V-number is previously defined, and U, as well as W, are modal parameters elsewhere defined in terms of fiber characteristics (Saleh & Teich, 2007),

$$U = k\rho\left({n_{co}}^2 - {n_{eff}}^2\right)^{\frac{1}{2}}$$

$$W = k\rho\left({n_{eff}}^2 - {n_{cl}}^2\right)^{\frac{1}{2}}.$$

By substituting the modal parameters into the Marcuse bend-loss relation, an analytic equation relating bend loss to bend radius is derived (derivation not shown),

$$\frac{P_1}{P_0} = exp\left[-\left(\left(\frac{\pi k}{R_b}\right)^{\frac{1}{2}}\left(\frac{(n_{co}-n_{cl})n_{co}\left({n_{eff}}^2-{n_{cl}}^2\right)^{\frac{1}{4}}}{{n_{co}}^2-{n_{eff}}^2}\right)exp\left(-\frac{4}{3}kR_b\frac{\left({n_{eff}}^2-{n_{cl}}^2\right)^{\frac{3}{2}}}{n_{co}(n_{co}-n_{cl})}\right)\right)\left(\frac{\pi R_b}{4}\right)\right].$$

This is specifically derived for a right-angle, hence the ${\pi R_b}/{4}$ term in place of z. With this analytical relation, the bend radius can be solved for any given power loss. The following figure is a plot of the bend radius of curvature as a function of core index for several throughputs (50%, 60%, 70%, and 90%). The cladding index is held at 1.46. Note, this plot is for the fundamental mode, and therefore is an optimistic estimate of bend loss. Higher order modes will require even larger bend radii for the same loss.

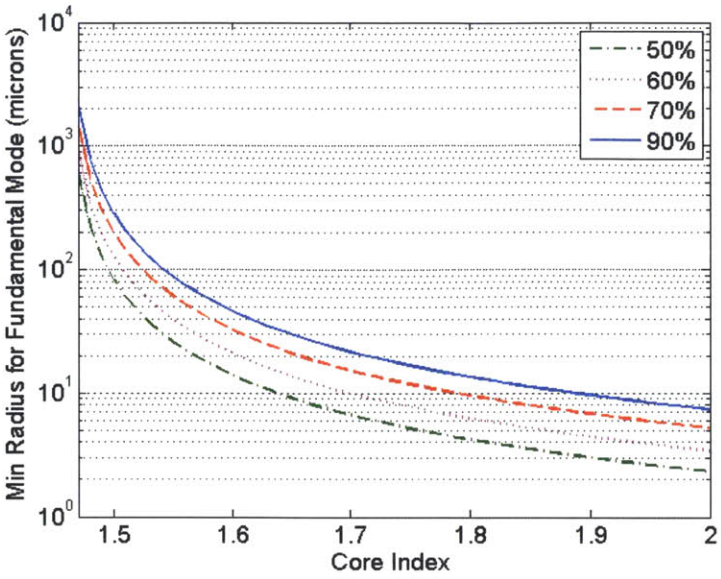

Figure 12 - Bend radius of curvature for a right-angle bend as a function of core index for several throughputs. The cladding index is held at 1.46.

This is an important calculation to make because the packing density must be made as high as possible. Figure 13 is a schematic illustrating why the bend radius is such an important consideration.

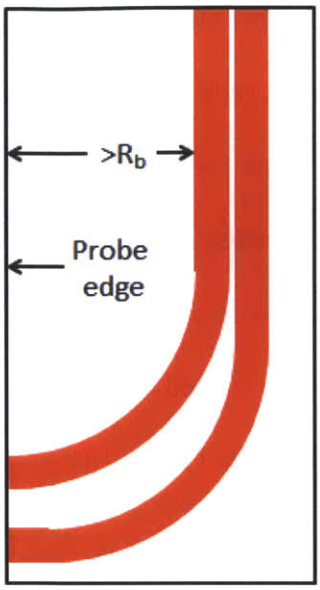

Figure 13 – The distance between the outermost waveguide and the substrate edge is at least the bend radius in length.

The distance between the outermost waveguide and the edge of the substrate is at least the radius of curvature for the 90° bend. This is an extremely important consideration for a this technology because the larger the size of the inserted shank, the more damage is done to the tissue. Keeping the size of the shank at an absolute minimum is paramount. For reasons which will be discussed in greater detail in the next chapter, the silicon oxynitride film deposited cannot go above an index of ~1.6. This has to do with the scattering and absorption properties of the silicon oxynitride films when there is a large nitride content. As can be seen from the theoretical work summarized in Figure 12, the bend radius must be at least ~50 μm for a loss of 80%. Also, this is for the fundamental mode, and therefore is a best-case scenario. Higher modes will have even higher losses.

The method taken to avoid this problem entirely is through the use of local mirrors. At the point in the waveguide when the right angle is to be introduced, a sharp 90° bend is introduced. The 90° bend does not allow for mode confinement. In fact, based on the theory developed above, even the fundamental mode is not confined. So, regardless of whether the waveguide is single-mode or multi-mode, all modes are upward coupled to radiation modes. The light, no longer confined to the core, is reflected off of a local mirrored surface at the abrupt junction (see Figure 14).

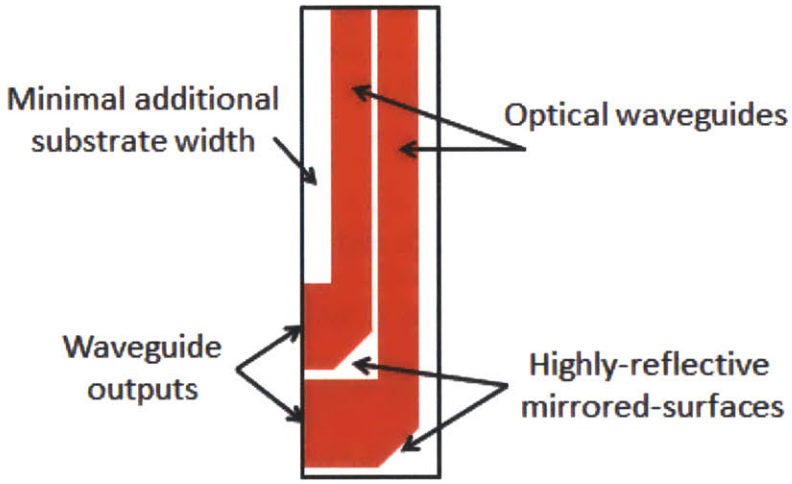

Figure 14 – Right-angle highly-reflective mirrored surfaces provide a way to avoid the unwanted extra space necessary in maintaining mode confinement in 90° curved bends.

The minimum additional substrate width is ~5 μm given the tolerances of deep RIE silicon etching. The reason the outputs are wider than the optical waveguide main body will be discussed in subsequent subsections. This mirrored surface is accomplished by simply depositing a thin metal surface over the waveguide outer cladding. The processes by which

these right-angle mirrors are fabricated, as well as their loss characterization, is outlined in the next chapter.

2.2 Power Requirements

As already discussed, the developed technology is an integrated array of waveguides out of which light is delivered. This delivered light is scattered and absorbed by the neural tissue. The main issue to considered is: how much light is needed to perturb a certain volume of neural tissue

A portion of the absorbed light provides the energy necessary to activate the light-sensitive opsins being cellularly expressed. The threshold irradiance at which the opsin proteins likely cause a neural response is ~1 mW/mm^2 (Boyden et al., 2005). Obviously, this lower irradiance activation threshold depends on opsin type, expression levels, illumination wavelength, etc. The volume of brain tissue over which there is an irradiance level of 1 mW/mm^2 or higher is determined by the total amount of optical power delivered. The more power delivered the larger the volume, the less power delivered the smaller the volume. Monte Carlo simulations have been conducted which show 6.25 mW of 593 nm light delivered from a 200 μm diameter fiber in neural tissue provides an irradiance of 1 mW/mm^2 over a volume of ~1.4 mm^3 (Chow et al., 2010). We can say that 6.25 mW is spread out over a sphere of radius ~700 μm, corresponding to an irradiance of 1 mW/mm^2 at the sphere surface. Instead of emitting light from a single fiber to control a single region, however, the technology here developed is designed to emit light from many different fibers to control multiple regions simultaneously. For this technology, the target radius over which

an irradiance of 1 mW/mm^2 is delivered was ~100 μm (as opposed to the 700 μm above). Using the same logic, the necessary output power can be back-calculated as ~100 μW (i.e. 100 μW spread out over a sphere of radius 100 μm corresponds to an irradiance of 1 mW/mm^2).

The waveguide core thickness is set at 9 μm (see Chapter 3 for fabrication reasons). The output aperture width is set at 60 μm. Therefore, the necessary output power of 100 μW corresponds to an irradiance at the output aperture of 200 mW/mm^2.

2.3 Heating

It is important to here discuss the question of heating. When this dissertation work was begun, the question of illumination source location was considered. Specifically, can the light sources (light-emitting diodes, edge-emitting laser diode, vertical-cavity surface-emitting laser, etc.) be implanted into neural tissue directly? The conclusion reached was that, no, the light sources cannot be implanted directly as tissue heating is of paramount concern (Elwassif, Kong, Vazquez, & Bikson, 2006). Aside from optical absorption, any energy not converted to photon generation or conducted away (a significant ratio for modern light source technologies (Ohno, 2004)) is delivered to the neural tissue. The scattering and absorption coefficients of neural tissue have been characterized previously (Kienle et al., 1996). Strongly wavelength-dependent, the light absorption is a further source of heating. This light absorption sets upper limitations on the intensity of light which can be delivered to a target. Put simply and precisely, it can be said that,

$$Q_T = Q_a + Q_s - Q_c,$$

where Q_T is the total heat delivered to target, Q_a is the heat delivered from photon absorption, Q_s is heat delivered from source inefficiency, and Q_c is the heat removed from the tissue's cooling mechanisms. It is important to note that the light delivery is not a steady-state, and most optogenetic experiments are performed with delivery pulses of low duty cycle. A more detailed mathematical description of this tissue heat flow is given by the Bio-heat equation,

$$\rho c \frac{\partial T}{\partial t} = \Delta(k\Delta T) + \frac{\partial q_a}{\partial t} + \frac{\partial q_p}{\partial t} + \frac{\partial q_m}{\partial t},$$

where ρ is tissue density, T is tissue temperature, k is the coefficient of heat conductivity, q_a is the heat flow from photon absorption, q_p is the heat flow due to blood perfusion, and q_m is heat generated from metabolic activity. This relation takes into account the two main sources of tissue cooling: conduction and blood perfusion. For the purposes of this study, the q_m term can be ignored. Also, instead of heat flow from photon absorption, heat flow from source inefficiency (heat directly conducted into tissue) is taken into account. Writing out the perfusion term and simplifying,

$$\rho c \frac{\partial T}{\partial t} = \Delta(k\Delta T) + \frac{\partial q_s}{\partial t} + \omega \rho_b c_b (T_a - T),$$

where q_s is the heat flow due to source heating, ω is the volumetric flow rate of blood, ρ_b is the density of blood, c_b is the specific heat of blood, and T_a is the average arterial blood temperature (here taken to be 310 K) (Nyborg, 1988). This differential equation was solved numerically using finite-element-analysis (comsol).

The simulation is of a 40 μm diameter LED on the end of a silicon shank of equal diameter. The silicon is taken to have thermal conductivity 149 $W / (m\,°C)$, a specific heat of 700 $J / (kg\,°C)$, and a density of 2300 kg / m^3. The LED is implanted in ~ 1 mm^3 of neural tissue, where the outer boundaries are held at 310 K. The tissue is taken to have thermal conductivity 0.5 $W / (m\,°C)$, a specific heat of 3650 $J / (kg\,°C)$, and a density of 1000 kg / m^3. The arterial blood parameters are taken to be ρ_b = 1000 kg / m^3 and c_b = 4200 $J / (kg\,°C)$ (Nyborg, 1988). The initial geometry and boundary conditions are shown in Figure 15.

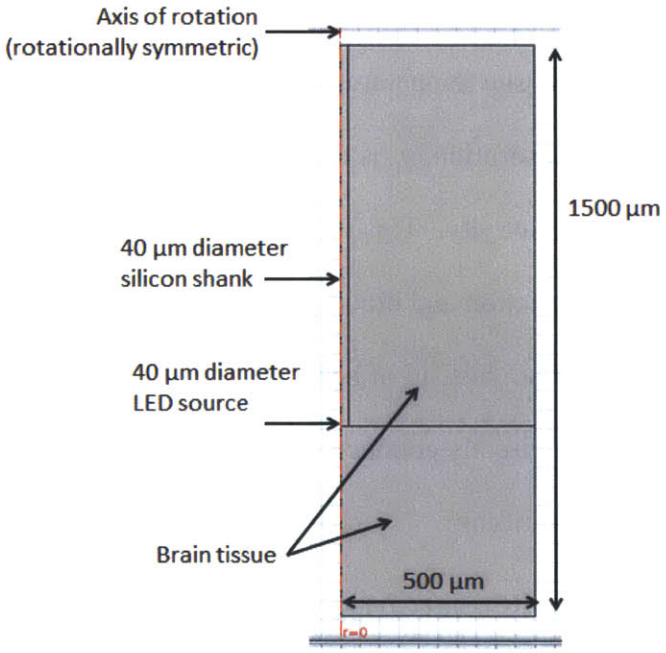

Figure 15 - Initial comsol simulation geometry. Two separate materials are defined: brain tissue and silicon. The heat source is a 40 μm diameter LED source. The model takes into account cooling due to blood flow in the brain tissue.

There is assumed to be zero thermal resistance between the LED and the silicon shank. At t=0 all boundaries and domains are set to 310 K. Based on the modern processing capabilities of GaN-based micro-LEDs (McAlinden et al., 2013), the LED efficiency range studied is 2% to 15%, and the range of irradiances studied is 10 mW/mm^2 to 100 mW/mm^2. 15% is a quite optimistic efficiency for microLEDs and 2% is more reasonable (McAlinden et al., 2013; Tian et al., 2012). 15% is simulated in anticipation of improving microLED technologies. An example result is shown in Figure 16, where this is a steady-state condition for an LED with a heat flux of 1000 mW/mm^2 (as a point of orientation, for an LED with 2% efficiency, this corresponds to 20 mW/mm^2 irradiance).

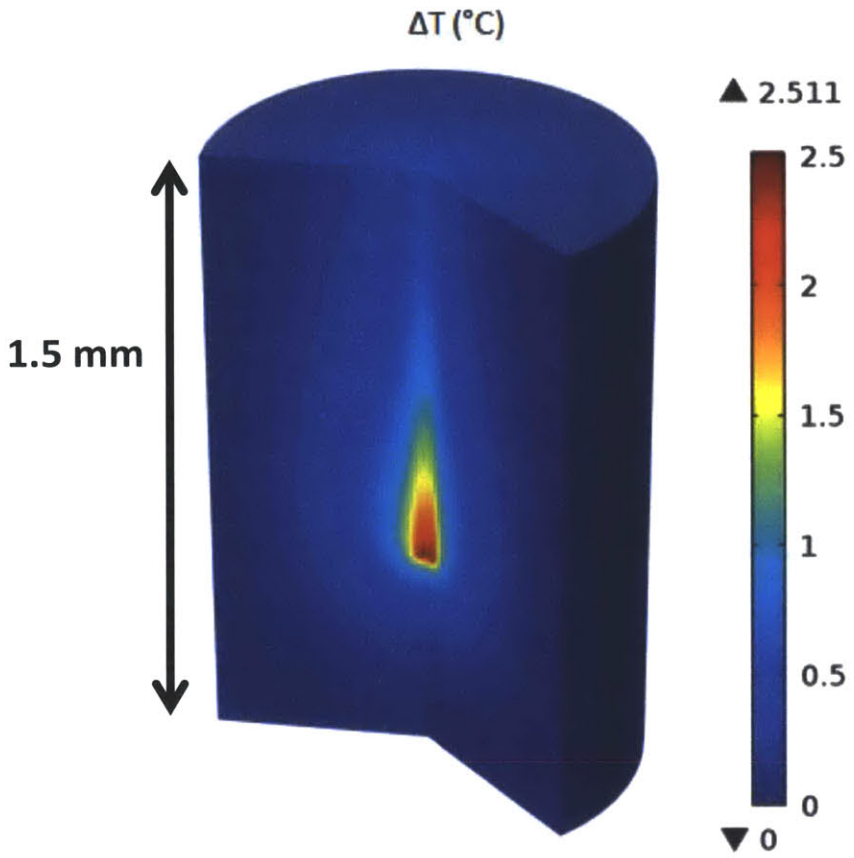

Figure 16– Cross-sectional 3D temperature plot (relative to 310 K). The height of the tissue modeled is 1.5 mm and the diameter 1 mm. Notice the heat flow bias along the silicon shank. This is due to silicon's significantly higher thermal conductivity. The temperature differential gets as high as 2.5 °C.

Figure 16 is a cross-sectional plot of the calculated temperature map (relative to 310 K). Notice the heat conduction path bias along the silicon shank. This is an important result, and is to be expected. Because the silicon has a significantly higher thermal conductivity, heat is correspondingly preferentially conducted. The body of the shank, then, serves somewhat as a heat sink for the illumination source. Notice very close to the emission site there is a rise in tissue temperature of 2.5°C. In quantifying to what extent neural heating is

acceptable, let us rely on the work of (Andersen & Moser, 1995) where a temperature differential of 1°C is presented as a maximum tolerance. So, the calculated rise of 2.5°C will surely cause damage. Figure 17 is a plot of the maximum neural tissue temperature change as a function of heat flux for the implanted LED.

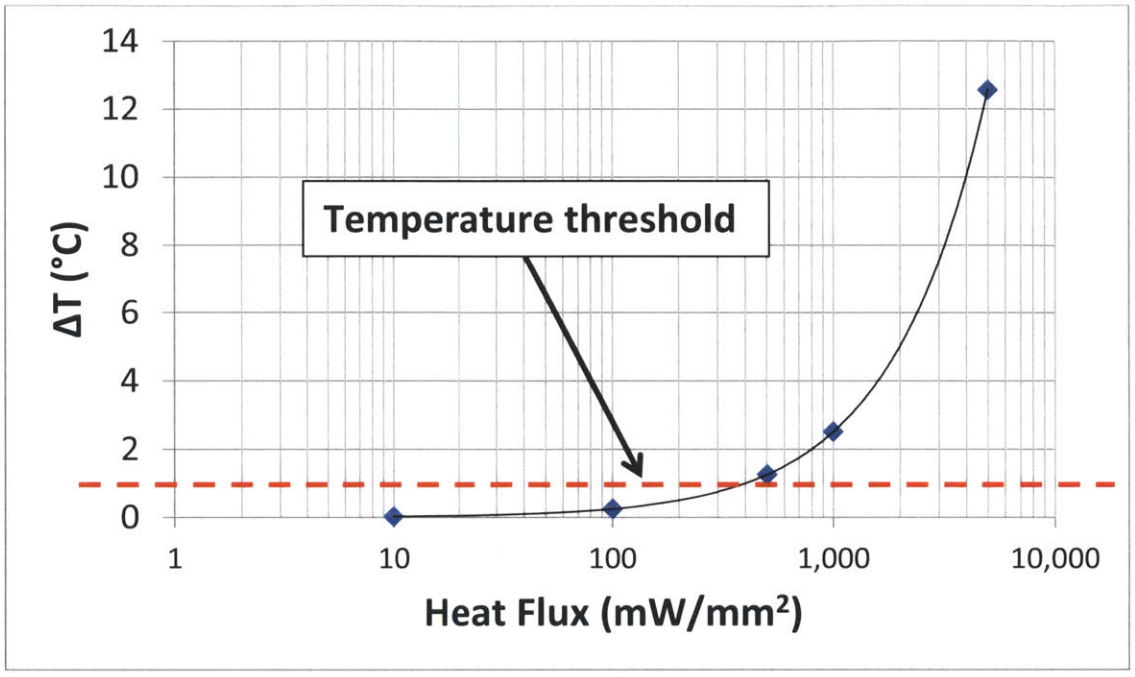

Figure 17 – Change in temperature as a function of heat flux at the LED site. What percent of this energy is converted to light power depends on the LED efficiencies. The temperature change exceeds the 1 °C threshold labeled by the red line.

The shown data is for the system in steady state after 2 seconds of CW LED operation. As can be seen from the data, for the system simulated, the maximum heat flux allowable is ~300 mW/mm^2, corresponding roughly to light output irradiance of 6 mW/mm^2 for an LED of 2% efficiency. These results reveal why waveguides were pursued over source implantation. The goal was to be able to deliver light output irradiance of upwards of 200

mW/mm^2 in CW mode. These results are conservative estimates of heating, as they ignore the effects of photonic absorption (which does set an upper limit on the power output of the optical waveguides, as discussed in the previous sub-section). The reason the photonic absorption affects can be ignored is that they are common to both methods. So, in simulating the viability of source implantation, if a zero-absorption-case does not yield acceptable results, then source implantation is surely not possible. With that said, comsol provides an optimal platform to simultaneously numerically simulate the heating and optical absorption/scattering properties of the system in the future.

There is, however, the possibility of tuning the duty cycle of stimulation so that less net energy is delivered to the system, and a lower *average* temperature is reached over time. Figure 18 shows simulation results for maximum tissue temperature differential as a function of time, where different plots are presented for different duty cycles. The simulation results presented thus far are for steady-state conditions; what follows is a presentation of simulation results for pulsed illumination. The frequency of stimulation is held at 20 Hz and the supplied heat flux (when on) is 600 mW/mm^2. This corresponds to 20 Hz stimulation with an output optical irradiance of 12 mW/mm^2 for a source with 2% efficiency; these are within the normal stimulation parameters used in optogenetics experiments. 2% is a reasonable efficiency estimate for microLEDs given the sourcesizes an current densities necessary for the irradiances being studied (McAlinden et al., 2013; Tian et al., 2012).

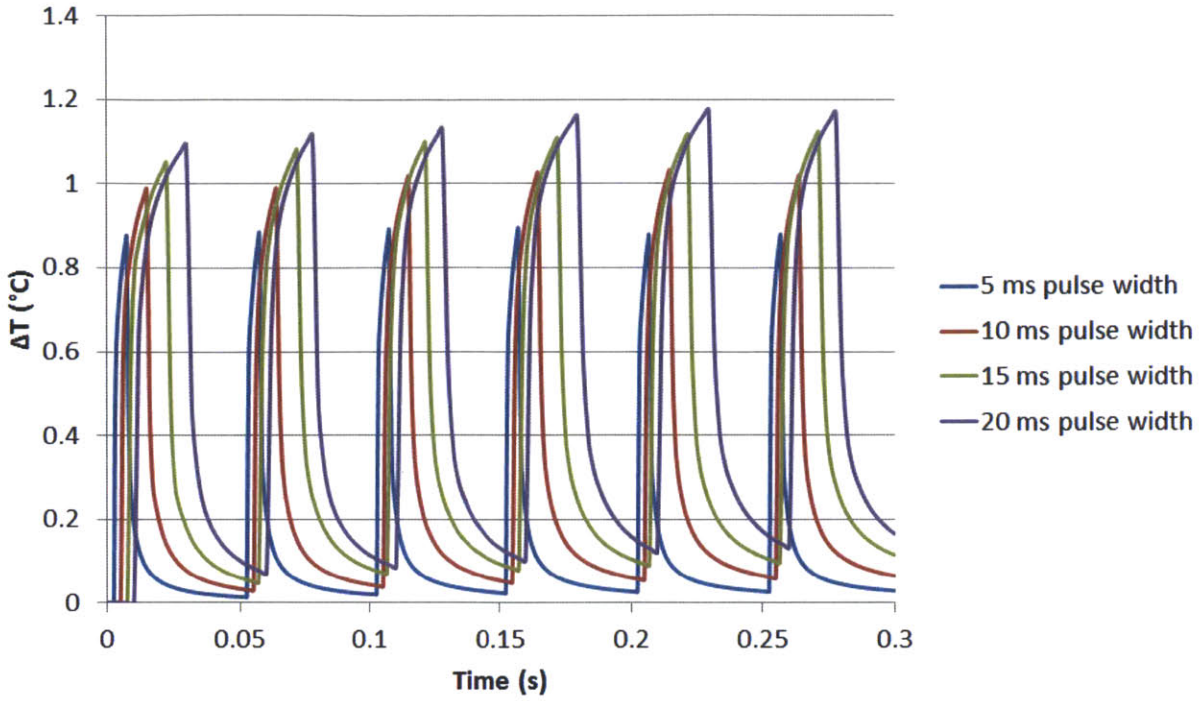

Figure 18 – Temperature change as a function of time for pulse trains of different pulse widths. The maximum temperature is lower for shorter pulse widths.

Note that as the pulse duration decreases, the maximum tissue temperature reached also decreases. For the data shown, the maximum temperature differential never exceeds 1°C only for the pulse width of 5 ms (opsins operate on a millisecond-timescale and will therefore respond for a pulse of this duration). The longer pulse widths cause the tissue temperature to rise beyond the acceptable range. Another parameter of interest for optogenetics is stimulation frequency. Shown in Figure 19 is the maximum temperature differential plotted as function of time for several stimulation frequencies.

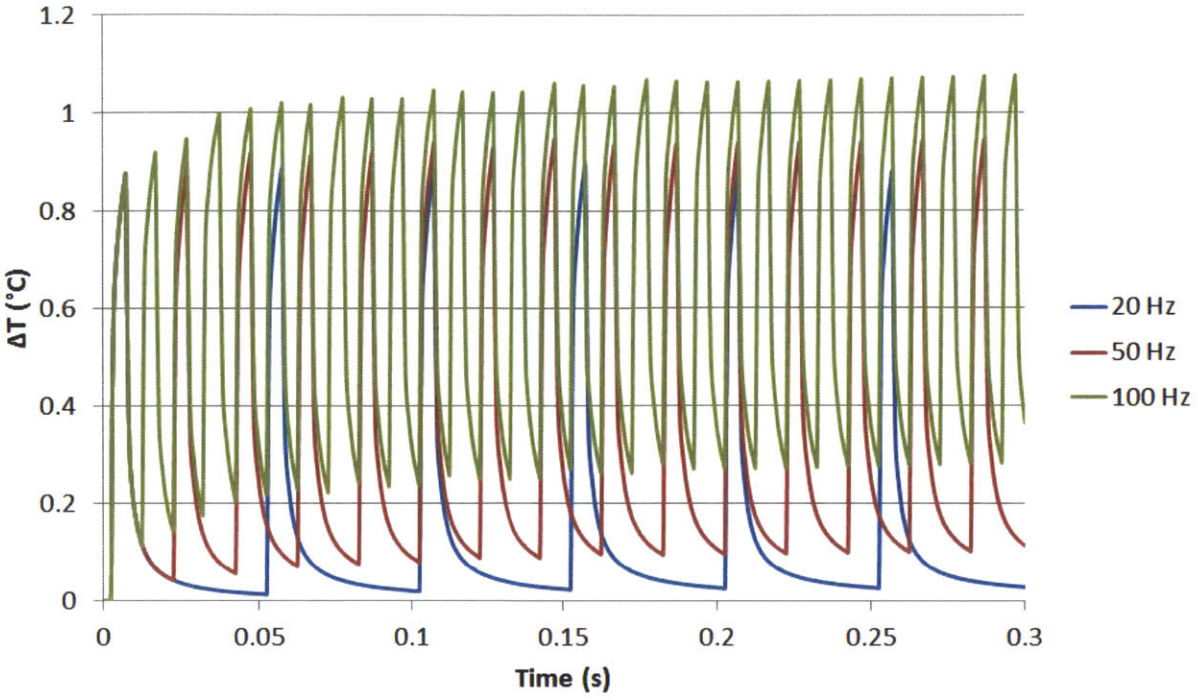

Figure 19 – Temperature change as a function of time for pulse trains of different frequency. The pulse width is set at 5 ms. The maximum temperature reached increases with increasing frequency.

The pulse width is 5 ms and the heat flux is again 600 mW/mm^2. Notice how at the 100 Hz and higher there is an upward trend to the average temperature. This causes the temperature to rise above threshold for these higher frequencies. At 20 Hz and 50 Hz, however, the thermal relaxation time of the system is short enough so that there is not an average rise in temperature and the tissue temperature has time to return to ~310K. Being restricted to delivery frequencies below 100 Hz is not an issue because the temporal kinetics of brain functioning is well below 100 Hz.

This model provides a means by which the effect a variety of different parameters have on tissue heating can be explored: shank dimensions, shank material, effect of blood

flow, integration of photonic absorption/scattering (comsol multiphysics), LED efficiency, etc. The purpose of presenting this analysis is to simultaneously explain why this dissertation avoided the pursuit of source implantation while demonstrating quantitatively how, given certain delivery constraints, source implantation remains a possibility to be explored.

A parameter sweep was conducted, varying the source optical irradiance, the illumination efficiency, the pulse duration, total pulse train duration, and the source diameter. For this model, instead of the heat flux being varied, the optical irradiance is varied for several different illumination efficiencies (what percent of supplied power is converted to optical power). A summary of the parameters tested are shown in Table 1.

Source Radius (μm)	**10, 15, 20**
Optical Irradiance (mW/mm^2)	**10, 50, 100**
Illumination Efficiency	**0.02, 0.05, 0.15**
Pulse Duration (ms)	**10, 20, 50**
Pulse Train Duration (s)	**0.1, 0.2, 0.3**

Table 1 – The different parameters used for the parameter sweep being described.

For all simulations, the stimulation frequency was held at 10 Hz. A series of summary plots showing various relationships between parameters follows. The variable, eta, refers to

illumination efficiency (ratio of electrical power delivered to source which gets converted to optical power). Obviously, all parameter combinations are not plotted.

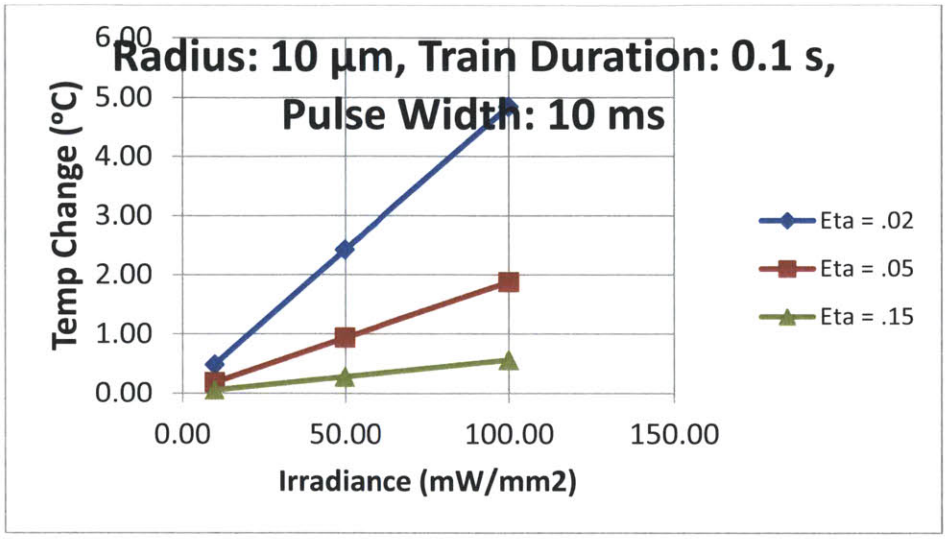

Figure 20 - Temperature change as a function of irradiance for several illumination efficiencies. As would be expected, as the illumination efficiency decreases, the temperature change increases (for any given irradiance).

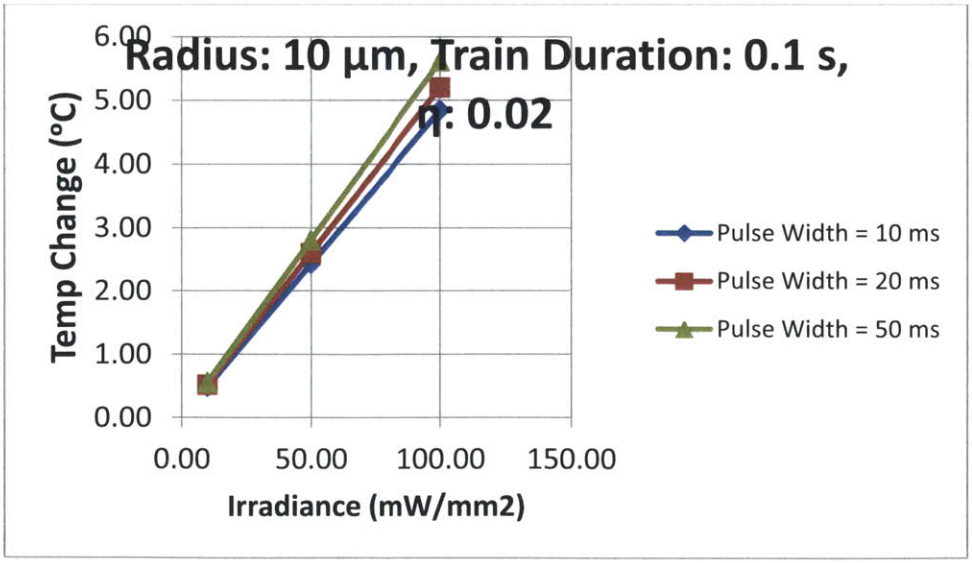

Figure 21 - Temperature change as a function of irradiance for several pulse widths. Although not a strong effect, as the pulse width decreases (for any given irradiance), the temperature change decreases as well. This is simply a function of the tissue's thermal relaxation time.

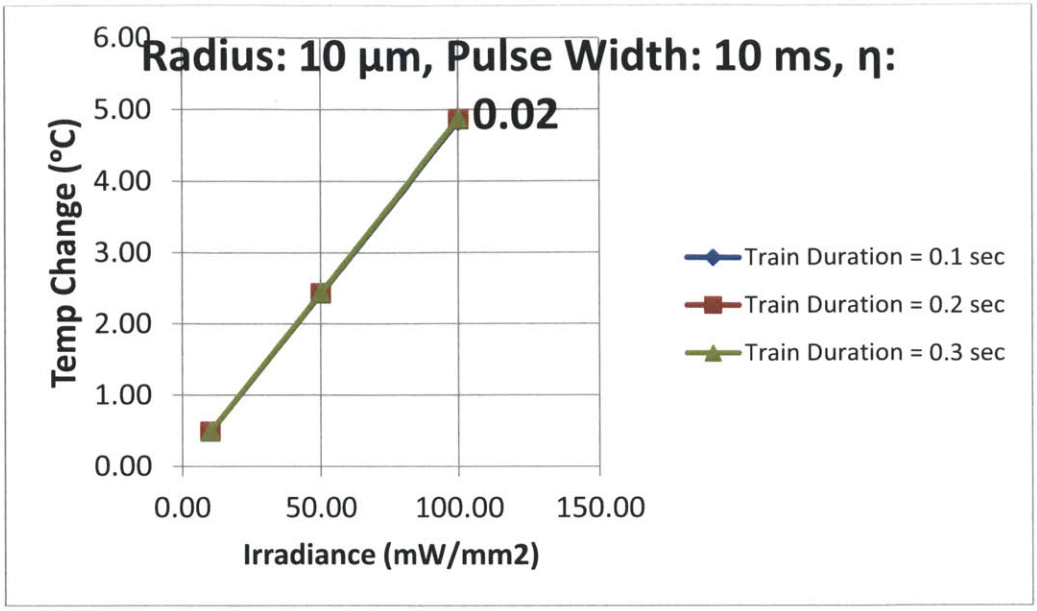

Figure 22 - Temperature change as a function of irradiance for several train durations. There is no significant change in temperature change as the total train duration is changed.

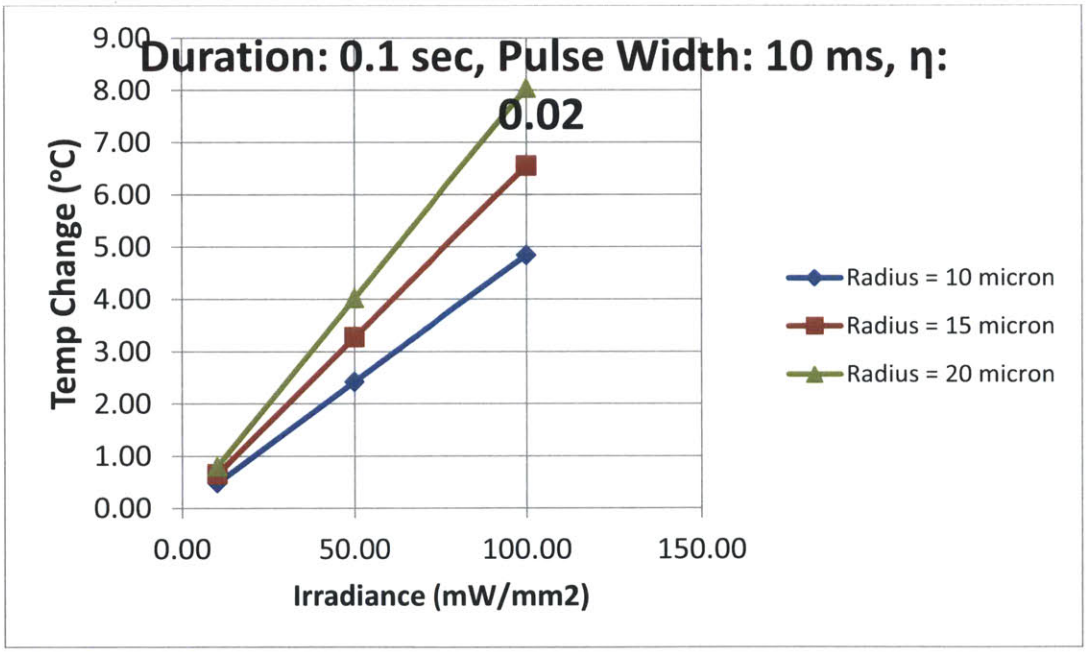

Figure 23 - Temperature change as a function of irradiance for several source sizes. As the radius decreases, the temperature change decreases (for any given irradiance). There are competing trends with this scaling: a smaller shank provides less heat conduction, but a smaller LED provides less heat flux.

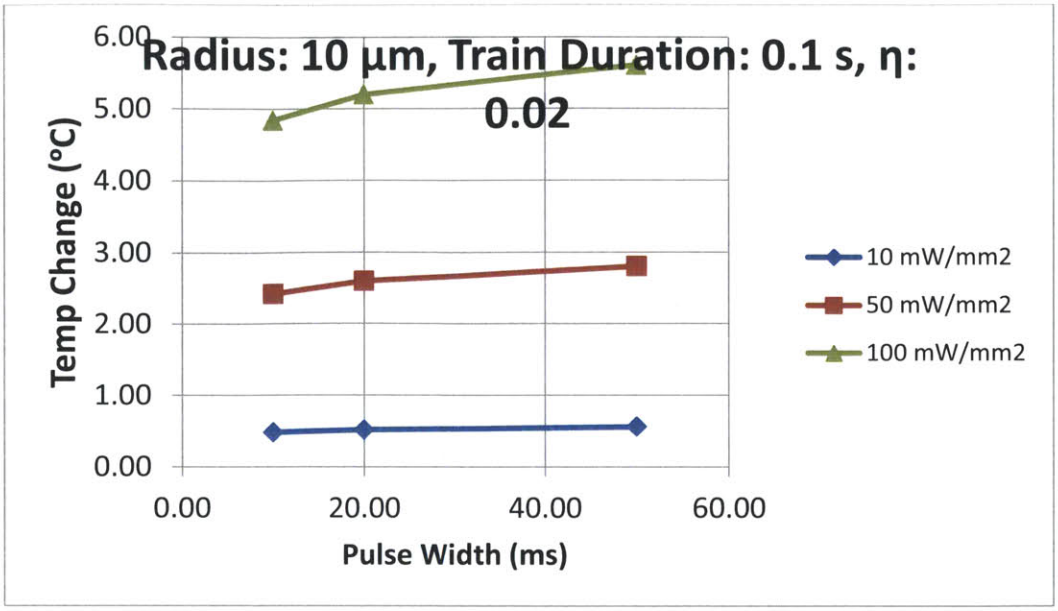

Figure 24 - Temperature change as a function of pulse width for several irradiance values. Consistent with the results shown in Figure 21, the effect pulse width has on temperature change (for any given irradiance plot) is not significant, although noticeable. As the pulse widths are decreased further, the different trends must converse at 0.

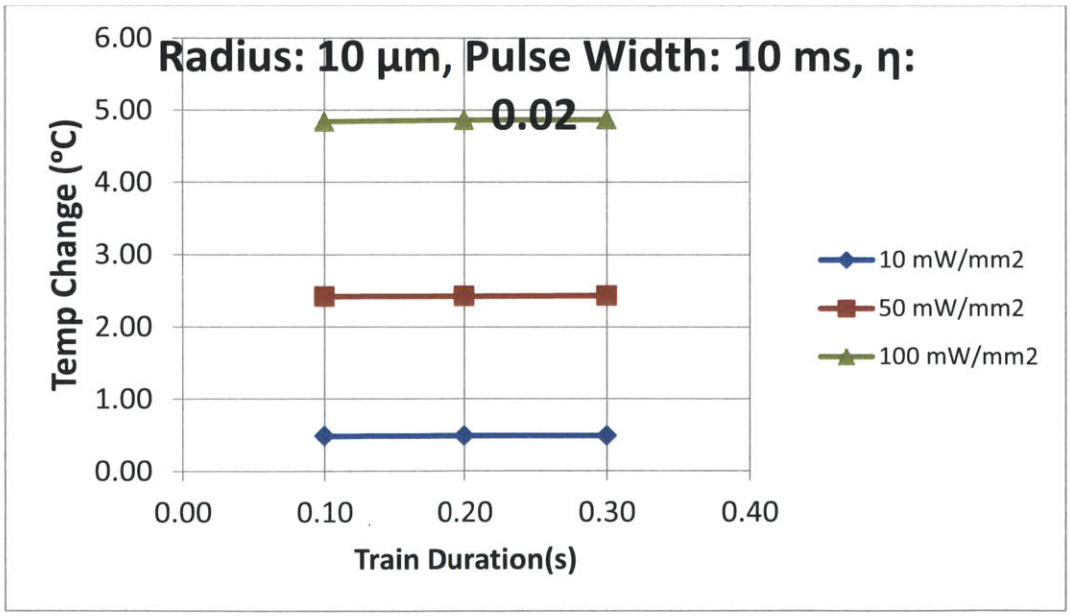

Figure 25 - Temperature change as a function of total train duration for several irradiance values. Consistent with Figure 22, there is no detectable temperature change for different train durations (for any given irradiance trend). Obviously, as with the pulse duration, as the train duration approaches 0, the temperature change must also converge to 0. However, at scales considered above, there is no discernible change.

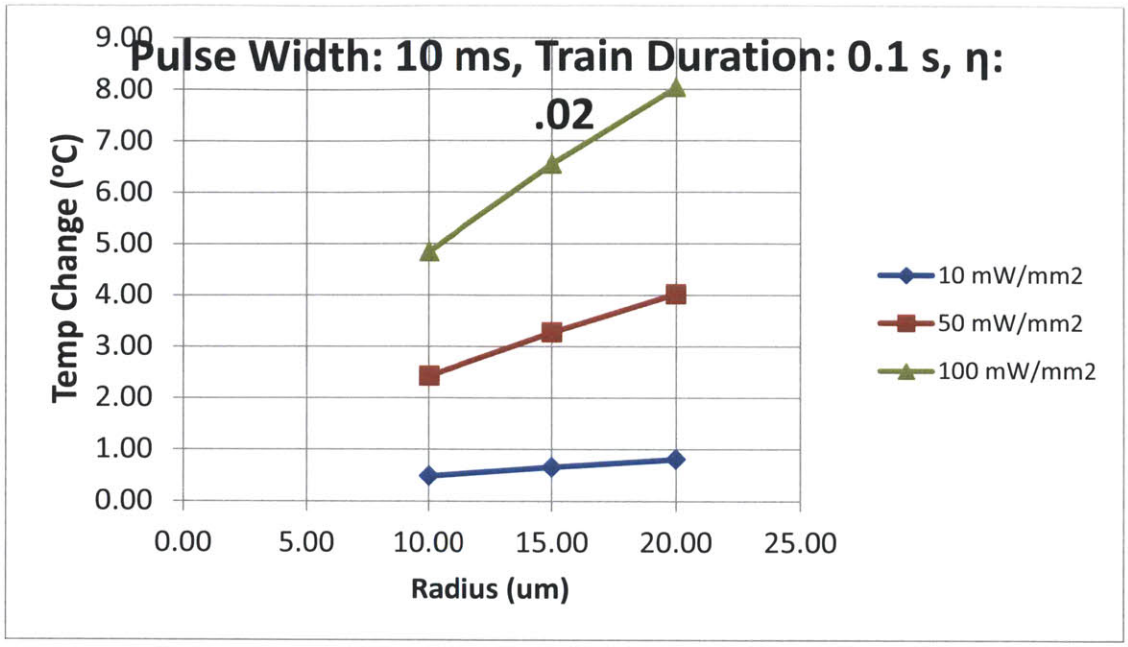

Figure 26 - Temperature change as a function of source radius for several irradiance values. Consistent with Figure 23, as the radius increases (for a given irradiance), the temperature change increases.

As stated before, the temperature change presented in Figures 20-26 are spatially located directly next to the LED in tissue. As can be seen in figures 18 and 19, the temperature changes over time in response to the stimulation pulse train. The temperature changes presented for figures 20-26 are the maximum over this stimulation time, and therefore represent the maximum temperature the tissue reaches. This model is for a single LED source in tissue. If there were multiple adjacent sources, the heating effect would be additive, and heating effects would be even more prevalent.

It should be noted that the temperature rises here presented are larger than the temperature rises presented in recent published work (McAlinden et al., 2013). The most likely reason for this is that the model matches the shank diameter with the LED diameter,

whereas the referenced work involves a significantly larger shank. In this work the LED area to shank cross sectional area is 1, whereas in (McAlinden et al., 2013) the same ratio is ~0.15. The relatively large shank cross section allows for improved heat conduction away from source, and by extension decreased temperature changes in tissue.

Although there are other potential issues with direct source implantation (inadvertent electrical stimulation, contamination of recording electrode, toxicity, etc.) it is worth noting there are sets of experiments subsequently made possible. In particular, because electrical power/signal connections are all that is necessary, it is the case that large-scale freely-moving optogenetics-based behavioral experiments would be made much easier. It will probably be the case, as these technologies develop, at least in the mid-term time-scale, that one technology will not satisfy all delivery and experimental requirements. Given a certain scale, desired illumination paradigm, etc., one particular technology will have its advantages and disadvantages.

Aside from what has already been discussed, another advantage of direct implantation of the illumination source is scaling. An important consideration is what volume of neural tissue is displaced in inserting the illumination probes. Because of the fabrication considerations the waveguide probes scale differently than the direct-source implantation. Specifically, the interconnects leading to the illumination sites have different minimum widths. As will be shown and validated in later chapters, the minimum waveguide pitch with acceptable loss characteristics is found to be 10 μm. This is simply for the current level of optimization conducted for the waveguides. This could conceivably be decreased, however the comparison below is for the technology as it stands now. Using

standard optical photolithography methods, metal interconnects can easily be fabricated to have a pitch of 1 μm. If assume the source being implanted is an LED, a reasonable assumption of LED size is 40 μm (chosen because of modern micro-LEDs being fabricated with this size (McAlinden et al., 2013)). With these parameters, how the cross-sectional area (for given shank thicknesses) of the inserted shank varies with number of illumination sites can be quantified (Figure 27).

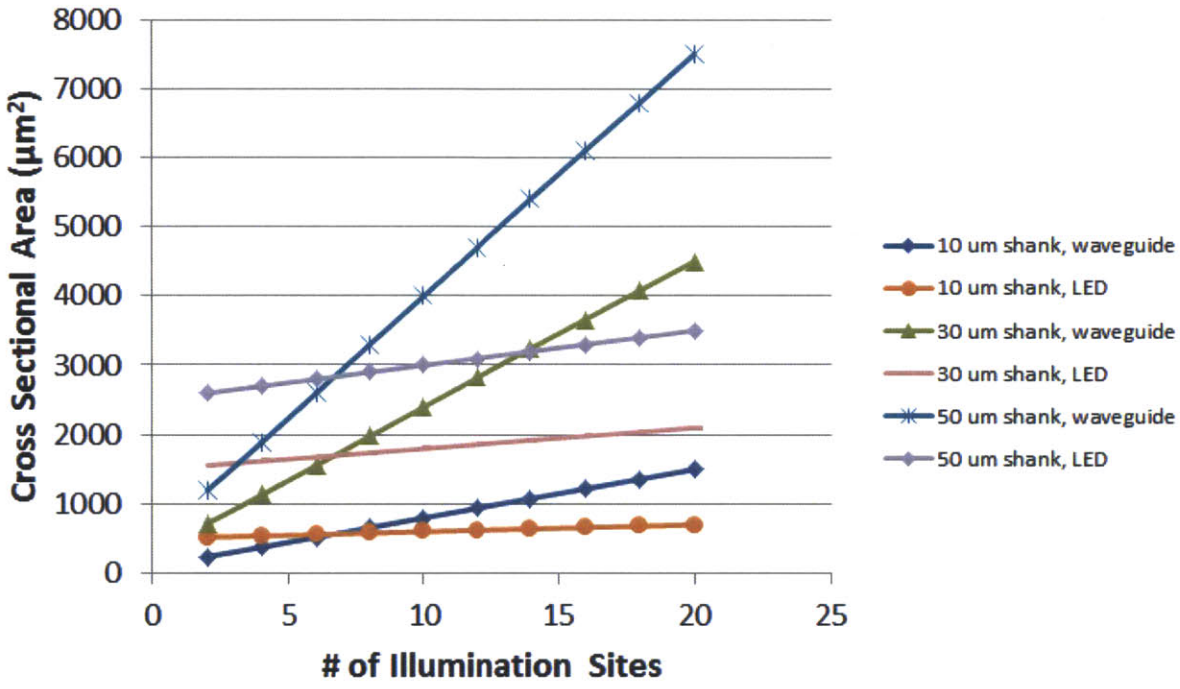

Figure 27 – Relationship between cross sectional area and # of illumination sites for different sized shanks and delivery technologies (i.e. waveguide vs. on-shank LED).

Given the parameter assumptions made, there is a range of illumination sites where keeping the illumination sources outside of neural tissue is advantageous (with regards to tissue damage considerations).

As a final point of comparison between direct illumination source implantation and optical waveguide, fabrication complexity and cost must be considered. The material cost of fabricating optical waveguides is negligible, where a standard 150 mm SOI wafer used is ~$100. By comparison, the material cost of fabricating GaN-based LEDs (or laser diodes) is large, where the stock 75 mm III-V wafer is in the thousands of dollars in cost.

Chapter 3: Waveguide Probe Fabrication and Characterization

3.1 On-chip waveguide fabrication background

The basic theory of optical waveguides has been covered from several perspectives for several basic geometries. Although much of the drive behind the development of fiber optics has been large-scale telecommunication and computer networking applications (Agrawal, 2010; DeCusatis, 2008), modern fiber optics research is increasingly geared towards integrated photonics (Wong, Filip, Wong, & Chung, 2007), specifically the photonic integrated circuit (Ristic, Bhardwaj, Rodwell, Coldren, & Johansson, 2010). A large part of the integration of photonics and silicon-based integrated circuit technologies involved developing optoelectronics integration methods (London, Loomis, Ahadian, & Fonstad, 1999) to create quasi-monolithic systems combining source and photonics circuitry

and devices. As the majority of integrated photonics research has targeted wavelengths in the IR, it has tended to use silicon core waveguides (Almeida, Barrios, Panepucci, & Lipson, 2004). However, all opsins used in optogenetics respond to the visible spectrum (Boyden, 2011), and silicon waveguides are opaque in the visible. Fortunately, silicon oxynitride based waveguides have also been studied for many years (Offrein, Germann, Bona, Horst, & Salemink, 1998; A. L. Zhang & Chan, 2003), and they are capable of propagating light from the UV through the IR, providing the flexibility and range needed for the current application.

We should here take a step back and look from a higher perspective why silicon oxynitride was chosen as the core material. The first options considered for a core material were polymer-based compounds. Specifically, an SU8-based waveguide system was developed initially. SU8 is a light-sensitive (UV) photo-definable polymer used in the microfabrication industry for a variety of purposes (Hong, Holmes, & Heaton, 2004; Seidemann, Rabe, Feldmann, & Buttgenbach, 2002). The results gathered from these waveguides were promising. There were two main reasons a SU8 core material was abandoned, and polymer-based waveguides in general. First, coating the high-aspect ratio SU8 core material with a low-index material posed some difficult challenges. When attempting to coat with a low-index polymer, getting full sidewall coverage for a high-aspect ratio waveguides is difficult. When attempting to coat with a low-index silicon-oxynitride the adhesion between core and cladding led to a severe amount of delamination (most likely due to thermal mismatch and humidity-induced flexing, a significant problem when designing a technology for tissue-implantation). The second reason polymer-waveguides

were abandoned was that we wanted to take full advantage of the fabrication technologies available for silicon-based integrated circuit fabrication. The fabrication facility utilized (MIT's Microsystems Technology Laboratory Integrated Circuit Lab and Technology Research Lab) is largely targeted towards silicon integrated circuits. With that said, there could be several advantages to pursuing polymer-based waveguides in the future iterations of this technology (Ma, Jen, & Dalton, 2002; Oh, Chu, Kim, & Kim, 2011). For one, there are many polymers which are either photosensitive, or much easier to etch. In either case this greatly simplifies the lithographic procedure. Also, because of the etching mechanisms, the sidewalls of polymer waveguides tend to be significantly smoother than their silicon-based counterparts. As will be shown soon, there is a strong dependence on sidewall roughness for propagation loss. Finally, there is a series of research demonstrating the extent to which scar tissue forms around neural implants is governed by the mismatch between the Young's modulus of the implant and the modulus of tissue (Polikov, Tresco, & Reichert, 2005). Although not yet conclusive, if this proves to be true, polymers tend to have a lower modulus, and would therefore induce less damage at equivalent spatial scales.

Within the chosen fabrication-friendly silicon-based core materials, there are several materials to choose from: silicon dioxide, silicon nitride, silicon carbide, and silicon oxynitride. Assuming the core/cladding combination is going to be some permutation of the above compounds, silicon dioxide cannot be a core choice, as it has the lowest index of refraction (see Table 2).

Name	Chemical Formula	Approximate Index of Refraction
Silicon Dioxide	SiO_2	1.46
Silicon Nitride	Si_3N_4	2.05
Silicon Carbide	SiC	2.6
Silicon Oxynitride	SiO_xN_y (can widely vary)	1.46-2.05

Table 2 – List of silicon-based compounds, their chemical formulae, and an approximate index of refraction. The index of refraction is for a 'standard' PECVD system and a wavelength of 532 nm.

As can be seen from Table 2, depending on its relative composition, silicon oxynitride has a variable index of refraction. This is a desirable attribute when designing a waveguide system because it allows for the adjustment of the index step between the waveguide core and cladding. There are two main consequences of a higher index step. First, the evanescent penetration into the cladding is limited, allowing for smaller spatial scales. Secondly, upward mode coupling due to micro-bending losses is limited (Saleh & Teich, 2007). The smaller the index step, the larger the losses associated with a given waveguide bend. Therefore, the larger the index step, the smaller the allowable radius of curvature for a waveguide bend and certain acceptable loss. This is an important design constraint. This argument would lead to the assumption that a larger index step is desirable. However, it is not without cost. That cost is mainly due to sidewall scattering losses (Lee et al., 2000). The Tien model (Jang et al., 2003) can be utilized to gain some insight into how the scattering losses depend on a variety of parameters,

$$\alpha_s = \frac{\sigma^2 k_0 h {E_z}^2 (\Delta n)^2}{\beta \int E^2 dx},$$

where σ is a parameter representing the surface roughness, k_0 is the free-space propagation constant, h is the transverse propagation constant, $(E_z/\int E^2)$ is the normalized optical intensity at the core-cladding interface, Δn is the index step, and β is the longitudinal propagation coefficient. As we can see, the scattering coefficient is strongly dependent on the surface roughness *and* the index step; an increase in index step engenders an increase in scattering losses. Therefore, a tunable index step between cladding and core material is highly desirable because it allows for an optimized location in parameter space between optical confinement and scattering losses. The core composition and index settled upon will be described and explained later in this chapter.

3.2 Waveguide Fabrication

The first step in fabricating the silicon oxynitride based waveguides lies in fabricating a test structure. The test structure we began with (Figure 28) contained a series of waveguides with a variety of geometries. The waveguides were of different width, taper angle, bend radius, and right-angle profile.

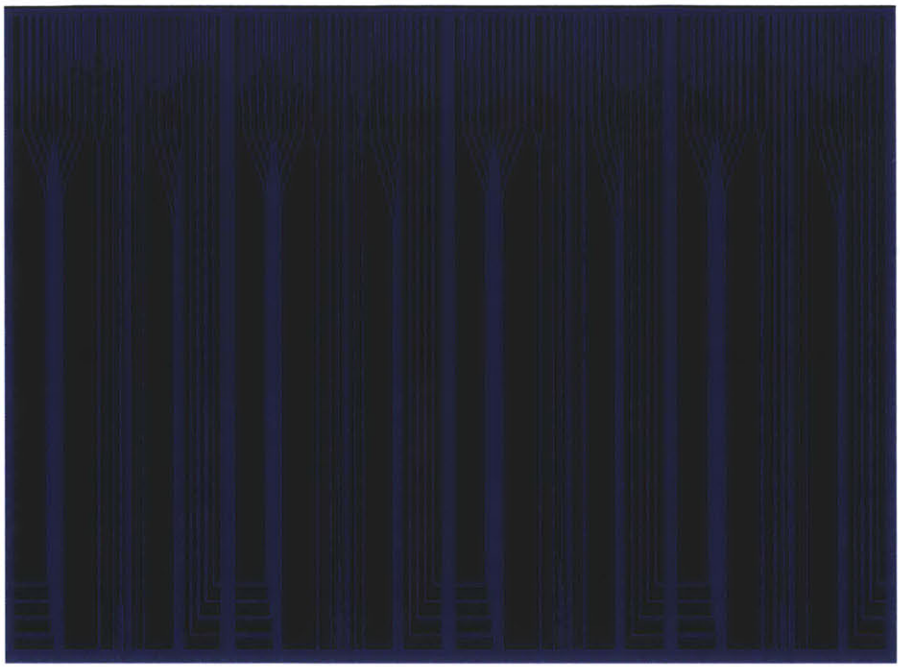

Figure 28 –A waveguide test structure used to quantify the propagation losses for different geometries.

We will now discuss the fabrication procedure, look at some of the preliminary results, and motivate some of the iterative improvements made in the fabrication procedure.

All fabrication was done on 150 mm silicon wafers. The first step in the fabrication procedure is to clean the wafer of all organics (piranha solution) and strip the native oxide (1:50 hydrofluoric acid dip). Note, as will be further described in Chapter 4, the starting substrate is a silicon-on-insulator (SOI) wafer. The wafer structure is shown in Figure 29.

Figure 29 – Cleaned 150 mm diameter SOI wafer

The lower cladding layer is then deposited (Figure 30). The material of choice is silicon dioxide (n~1.46 at 532 nm). The technology we utilized for depositing the silicon dioxide is plasma-enhanced chemical vapor deposition (PECVD). The gas chemistry used is a combination of silane, nitrous oxide, and nitrogen (see Appendix A for further details). The thickness of this lower cladding layer was chosen to be 3 μm so it is thick enough so the light propagating in the core does not interact with the underlying Si. This will be confirmed experimentally and theoretically later in this chapter.

Figure 30 - Lower cladding deposited

The next fabrication step is to deposit, with the same PECVD system the core material, in this case silicon oxynitride (Figure 31). The composition of silicon oxynitride is variable between that of a pure silicon dioxide and that of a pure silicon nitride.

Figure 31 - Core (silicon oxynitride) deposited

Selecting the correct chemistry and PECVD recipes involved iteratively fabricating test structures and testing waveguide performance. The film composition settled on has an index of refraction of ~1.53 at 532 nm. This choice will be further discussed in the following sub-section on waveguide characterization. The thickness of this core material is 9 μm. For a silicon oxynitride waveguide, a 9 μm core is very large. Silicon oxynitride waveguides in the integrated photonics community are usually less than a micron thick because those applications require single mode waveguides. We do not have that restriction and can make them thick to make coupling light into them easier. This will become more clear in Chapter 5.

The core and first cladding material are patterned in the waveguide geometry with a photolithographic etching step (Figure 32).

Figure 32 - The core and lower cladding are lithographically defined

A thick resist (AZ P4620) is patterned on the surface. It is necessary that this be a thick photoresist (8 μm thickness target) and well post-baked to withstand the aggressive and long etch step which follows. The etch is conducted in an Applied Materials oxide reactive ion etch (RIE) system (see Appendix A for details). The gas chemistry is CHF_3 based and

anisotropic. See Figure 33 for a cross-sectional SEM micrograph showing the details of the etch.

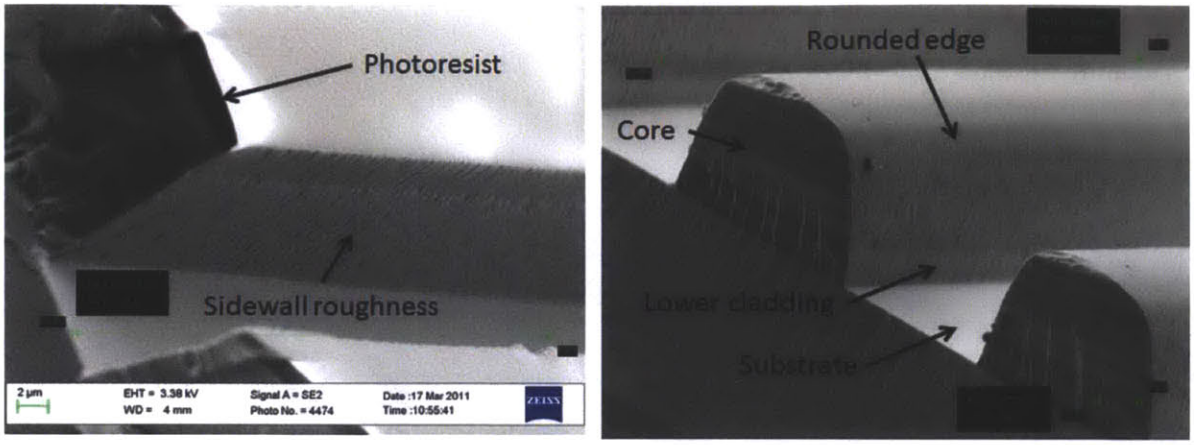

Figure 33 – Etched silicon oxynitride core test structures.

Note in Figure 33 the rounded edge of the core structure on the rightmost micrograph. If the photoresist mask is not sufficiently hardbaked in its development, it will result in a reflow of the photoresist during the aggressive subsequent plasma etch step. This will result in distorted features. Further details on the necessary temperature and time for post-baking the photoresist can be found in Appendix A. The photoresist is then removed. Because the photoresist has undergone a rather aggressive and long-term plasma environment (necessary due to the unusually thick silicon oxynitride layer), it is extremely difficult to remove. Through trial-and error, we settled on the following cleaning steps: two consecutive piranha etches (3:1, sulfuric acid:hydrogen peroxide) followed by an oxygen-based high-power 'ashing' step. A single piranha etch is 10 minutes long and begun immediately after mixing the sulfuric acid and hydrogen peroxide at room temperature. The ashing is done in an oxygen plasma (200W, 0.5 torr) with the wafer held at 80°C for 4 minutes. Verification that

the photoresist was totally removed was obtained with a fluorescence microscope. The fluorescence of photoresist under certain illumination wavelengths provides an easy and efficient method for determining to what extend the photoresist has been removed. (Kimura & Takami, 1988).

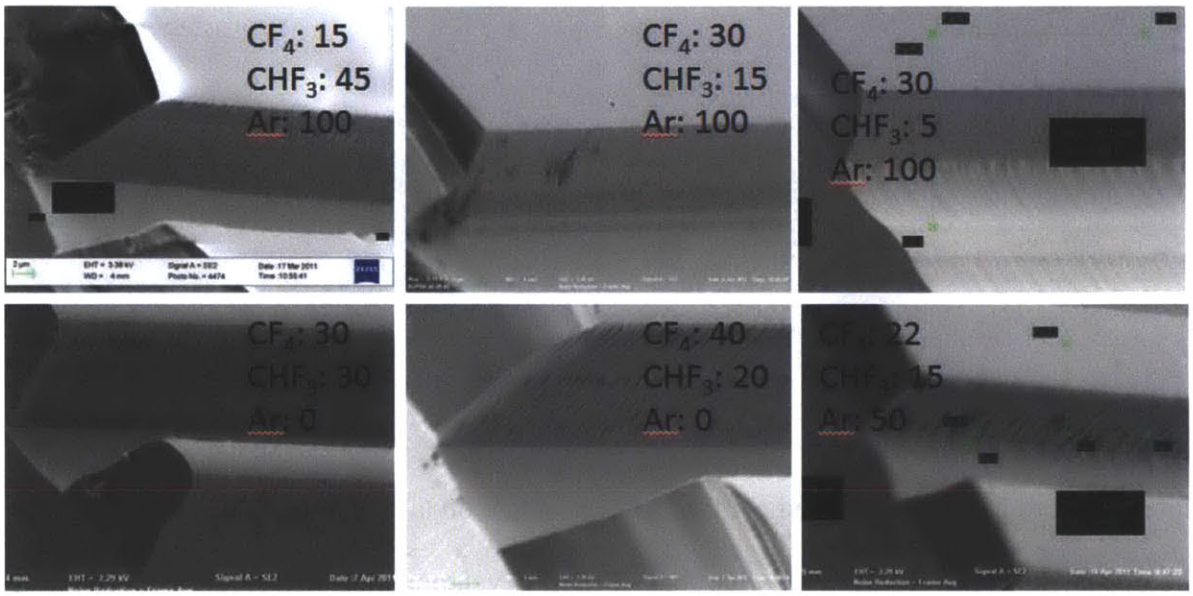

Figure 34 - SEM micrographs of test structure sidewalls for a variety of different etch recipes. Values next to gasses in sccm units.

See Figure 34 for a more detailed view of the sidewall roughness of the waveguide core. Although this roughness was not quantified, an iterative sweep of different etch chemistries, powers, masks, etc. was performed to see (qualitatively) what affect it would have on the roughness. In addition to sidewall roughness, this SEM-based assessment also revealed how aggressive different recipes were to the photoresist mask. The thinner the photoresist, the easier it is to photo-lithographically define a given feature size. Therefore, the thinnest possible photoresist must be targeted for a given etch. Of the above six plasma etch recipes

tested (see Appendix A for remaining details), the recipe with gas flow values of CF_4=30 sccm, CHF_3=15 sccm, and Ar=100 sccm was determined to be the least aggressive to the photoresist and provide the smoothest sidewalls.

The upper cladding layer is then deposited at a thickness of 3 μm (Figure 35). Obviously, it is important all sides of the core material are covered by the upper cladding, silicon dioxide. Because of the mechanism of deposition, PECVD, the sidewall coverage is quite complete. This is a well-known and documented advantage to PECVD deposition technologies (Archard, Giles, Price, Burgess, & Buchanan, 2010).

Figure 45 - Upper silicon dioxide cladding is deposited

The final step (before packaging considerations) of the waveguide test-structure is to deposit a top metal layer (Figure 36). As discussed at length in Chapter 2, the metal layer serves as a reflection surface in the case of right-angle bends. The metal chosen is titanium (0.5 μm) and the deposition technology chosen is sputtering.

Figure 36 - A layer of titanium is sputtered to provide highly-reflective surfaces off which light can reflect in the case of corner-mirrors.

It is extremely important the metal sidewall coverage be complete in this region. The sputtering technology is chosen because it is has a far superior sidewall coverage relative to the more common electron-beam deposition. This is for two reasons. First, electron-beam deposition requires a very low-pressure chamber, which increases the mean-free-path, which makes it statistically less likely metal atoms will be incident on the sidewall at angles significantly different from 90°. Secondly, the electron-beam source is held at a greater distance and is much smaller, whereas sputtering targets are upwards of 10" and held <1cm from wafer.

At this point, the waveguide stack is complete, and all that is left to couple to the test structures is to remove them from the handle wafer. The approach we take is to first diesaw out the test structures and then polish the end faces (both input end and output end). The final polishing compound used is a 1 μm aluminum oxide slurry applied to a felt pad on a polishing wheel.

3.3 Waveguide Characterization

For the purposes of this work, the most important waveguide characteristic is surely power loss. The three mechanisms of loss for the optical waveguides being fabricated are: input loss, propagation loss, and corner-mirror loss. The input loss is the loss associated with coupling the illumination source to the waveguide. The propagation loss is the loss resulting from any number of mechanisms along the length of the waveguide (e.g. bend loss, Rayleigh scattering, absorption, sidewall scattering, etc.). The corner-mirror loss can be considered a sub-set of propagation loss, and is the loss associated with the 90° mirror used at the output. All loss measurements in this work are reported in logarithmic units of dB. Specifically,

$$Loss\ in\ dB\ between\ A\ and\ B\ \equiv -10\ log\left(\frac{P_A}{P_B}\right),$$

Where P_A is the power at point A and P_B is the power at a point B.

Two methods were used to characterize the waveguide loss performance: the cut-back method and the out-scattering method. Light was coupled to the input end of the waveguides by butt-coupling from a single-mode fiber with a mode-field diameter of 5 μm. The butt coupling was accomplished by using a 3-axis stage assembly to control the position of the fiber output while the waveguide system is held steady with a vacuum grip. A drop of index-matching fluid is applied between the fiber output and the waveguide input. The cut-back method involves measuring the throughput at progressively shorter lengths of the waveguide, where the waveguide is being cleaved to shorter and shorter lengths between

measurements. Example results of this method are shown in Figure 37. These results are for a straight waveguide with a width of 20 μm and a thickness of 9 μm.

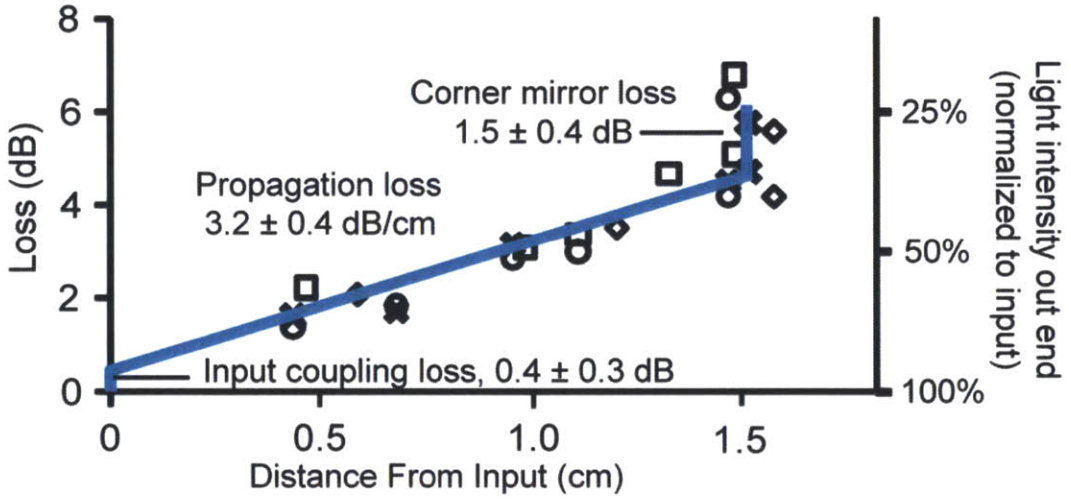

Figure 37 - Example results for the cut-back method. Loss measured via measurement of light out of end of probe, after cut-back to various lengths. This method gives the coupling loss, the propagation loss, and the corner mirror loss. Each data icon type represents a different waveguide.

Note that the propagation loss and corner mirror loss measured to be 3.2 ± 0.4 dB/cm and 1.5 ±0.4 dB, respectively. Also note that the input coupling loss can be inferred to be 0.4 ± 0.3 dB. The input coupling inference is gathered simply by tracing the fit trend-line to an input distance of zero. The corner mirror loss is measured by cleaving the waveguide just prior. The input coupling loss is inferred by tracing the loss to zero distance from the input.

The out-scattering technique (Skorka, Meyler, & Salzman, 2004) is based on a very simple assumption: that the intensity of light scattered at each point along a waveguide is directly proportional to the intensity of the light in the waveguide at that point. Implicit in

that assumption is that the scattering properties are independent of power and are uniform along the length of the waveguide. With an image taken of a waveguide with light coupled to the input end, we can get a scattering intensity as a function of distance. As that scattering intensity is assumed to be directly proportional to the power, we can measure the propagation loss using this image analysis technique. See Figure 38 for the out-scattering results.

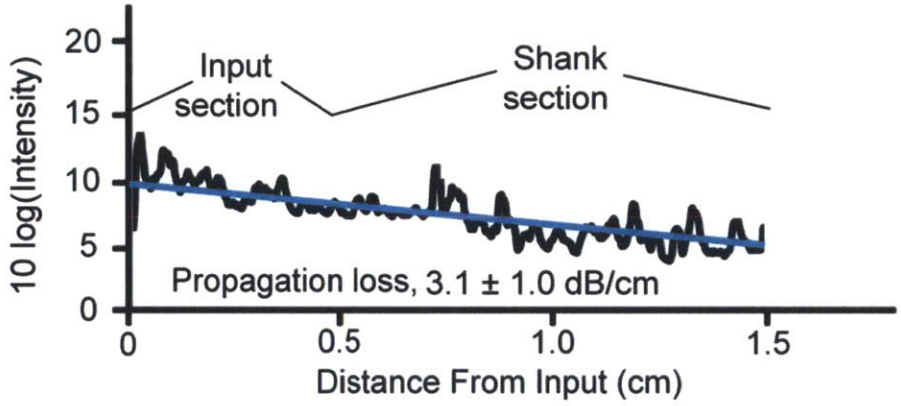

Figure 38 - Example results for the out-scattering technique. Light scattered out through top surface of probe after the titanium has been stripped off. This technique only gives the propagation loss.

Note the propagation loss is measured to be 3.1 ± 1.0 dB/cm. This is in good agreement with the measurement results for the same straight waveguide (9 μm x 20 μm) using the cut-back method.

To assess what the optimal core index of refraction is, the propagation loss was measured for a series of different core refractive indexes. The ability to tune the index of

refraction of silicon oxynitride is, as discussed previously, precisely the reason this material is so desirable. The index of refraction of silicon oxynitride lies between that of silicon dioxide (~1.46 at 532 nm) and that of silicon nitride (~2.05 at 532 nm) depending on the relative content of the material. The usual manner in which silicon oxynitride content is controlled is through variation of the gasses used in the PECVD growth. The gasses used in silicon dioxide growth are nitrous oxide (N_2O) and silane (SiH_4). The gasses used in silicon nitride growth are silane and ammonia (NH_3). All three gasses (nitrous oxide, silane, and ammonia) are used for silicon oxynitride growth. The relative portion of the nitrous oxide and ammonia are what dictates the content of the silicon oxynitride film. Five separate recipes were created yielding refractive indices of 1.47, 1.53, 1.69, 1.91, and 2.01. See Appendix A for details on these recipes. These refractive indices were measured using an ellipsometer at a wavelength of 633 nm. The test structure measured was a straight 20 μm wide waveguide with a thickness of 9 μm. The cladding was a pure silicon dioxide and had a thickness of 5 μm. Losses in excess of 25 dB/cm were measured for the refractive indices of 1.47, 1.91, and 2.0. The core of 1.47 was nearly identical to the silicon dioxide cladding. Although not beyond the resolution of the ellipsometer used, this small index step did not allow for modal confinement. It is not certain why the higher refractive indices mentioned (1.91 and 2.0) yielded large loss measurements. One potential explanation is sidewall scattering. As discussed previously, sidewall scattering is exacerbated by large index steps. Another explanation could be the absorption properties of the deposited core material. The propagation losses measured for the waveguides with core refractive indices of 1.53 and 1.69 were 3.1 dB/cm and 5.3 dB/cm respectively. Of the different composition silicon

oxynitride cores measured, therefore, the core with an index of 1.53 yielded minimum propagation loss characteristics. This, in turn, was the core material chosen.

With this core/cladding choice, the numerical aperture is ~0.46. Because of this large numerical, the waveguides have a high light-collection capability. It is for this reason fibers in imaging bundles tend to have high numerical apertures (upwards of 0.6). Therefore, it is conceivable that this technology could be used also as an optical detector. Not quantified in this work, the possibility of successful imaging or detection depends on source brightness (whether neurons are fluorescently tagged or an electro-optical transducer applied to the aperture), aperture density, aperture size, etc.

Next, the propagation loss was measured for the same straight waveguide structure (and core refractive index of 1.53) but variable lower cladding thickness. The propagation losses were measured for lower cladding thicknesses of 1 μm, 2 μm, 3 μm, and 5 μm. As is shown in the results (Figure 39), the propagation loss no longer decreases as the thickness is increased beyond ~3 μm, indicating that this thickness is sufficient to eliminate interaction between the guided modes and silicon substrate.

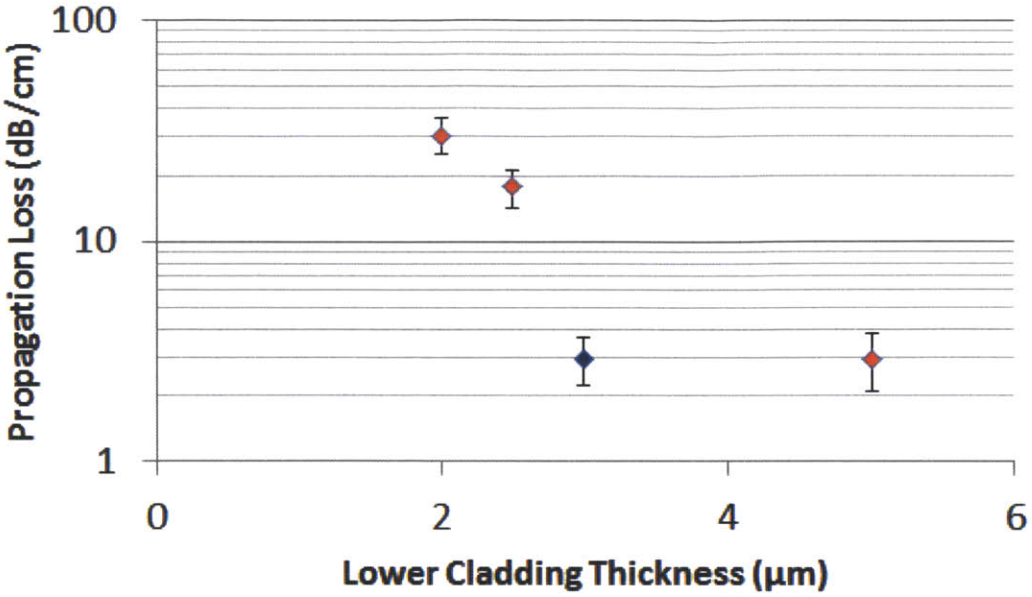

Figure 39 - Propagation loss measured as a function of lower cladding thickness. The propagation loss stops decreasing as the lower cladding thickness reaches 3 µm.

This means the negative effect lower cladding has on propagation loss is erased at that thickness, 3 µm. This empirical result fits well with the theoretical work done by Ed Barkley in Figure 40.

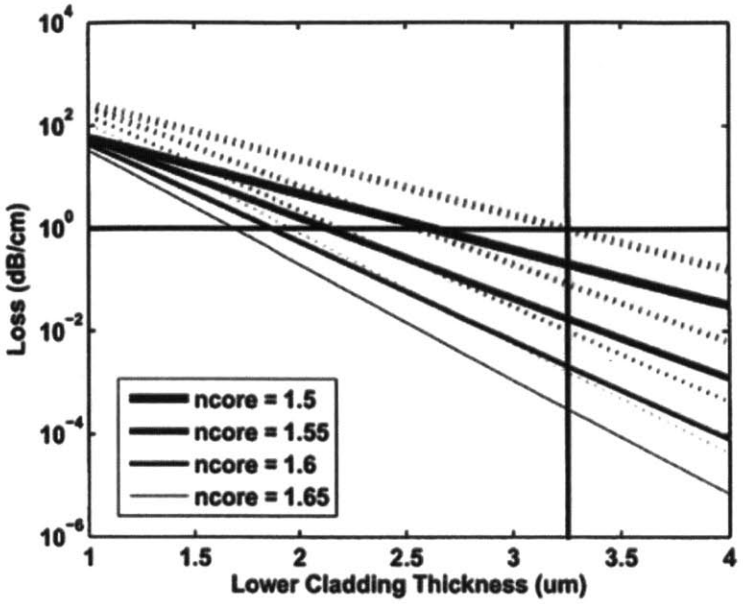

Figure 40 - Loss from substrate evanescent coupling as a function of lower cladding thickness. Dashed lines TM polarization, solid lines TE polarization. This plot was made by Ed Barkley (Barkley, 2007) based on (Nishi et al., 2010).

The figure shows the propagation loss as a function of lower cladding thickness for TM and TE polarizations and different core indices. The vertical line shows where the TM polarization with a core of 1.5 intersects a loss of 1 dB/cm.

Using both the cut-back and out-scattering methods, the loss associated with three separate bend radii were measured: 500 μm, 750 μm, and 1000 μm. No measurable loss was detected using either technique for any of the three curvatures. Given the large index step chosen, this is to be expected (see Chapter 2 for an in-depth discussion of bend loss). The reason the curvatures measured were so large is that large radius bends are needed in the design to re-direct the waveguides from a large-pitch input region to a small-pitch insertion

shank region (see Chapter 4 for geometric outline). There is plenty of substrate space available for this, so there is no need for small curvature bends in this part of the layout.

The 3dB/cm loss is for a waveguide width of 20 μm. As packing density along an insertable shank will be depend on the photonic interconnect pitch, the smaller the waveguide width, the better. Although the test structure shown in Figure 28 does contain several different straight waveguides of different width, it was not sufficient for testing widths down to 5 μm, so a separate test structure with a series of waveguide widths was created. The widths tested were (5, 6, 7, 8, 10, 12, 14, 16, 18, and 20 μm) and all waveguides were straight (i.e. there were no 90° bends) and 9 μm thick. The results from these measurements are shown in Figure 41.

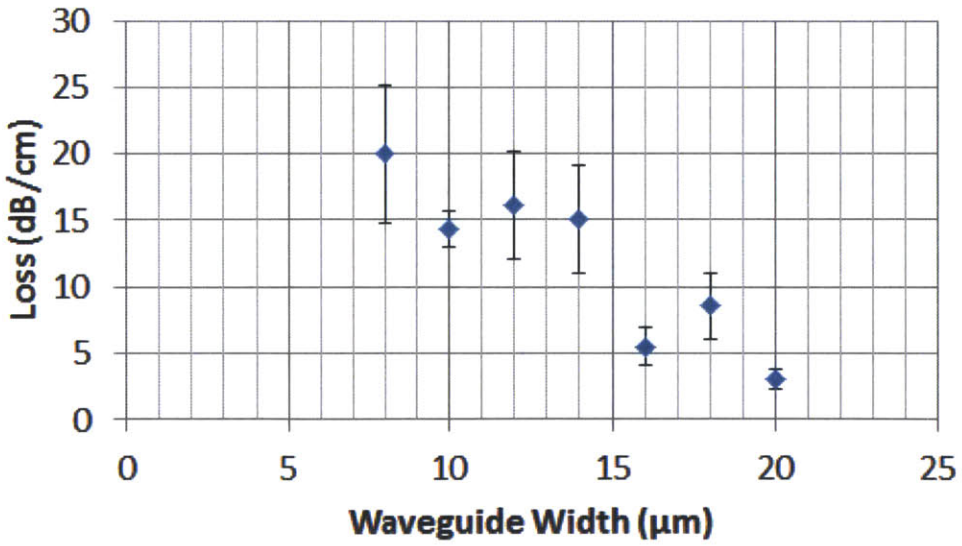

Figure 41 – Propagation loss as a function of waveguide width.

As can be seen from Figure 41, at widths below 15 μm the propagation losses are unacceptably large. Pure silicon oxynitride contains no hydrogen atoms. PECVD deposited

silicon oxynitride does, however, contain a certain amount of hydrogen content because of the gas chemistries used (see Appendix A for more details). The gases used are silane, ammonia, and nitrous oxide. The hydrogen contamination is an unavoidable consequence of using gaseous silane and ammonia for deposition. The hydrogen content in the oxynitride core engender nano-scale fluctuations in the index of refraction (Worhoff, Klein, Hussein, & Driessen, 2008). These nano-scale fluctuations lead to a rayleigh-type scattering loss. An effective way to drive the hydrogen content down in oxynitride films is an annealing step (Denisse, Troost, Habraken, Vanderweg, & Hendriks, 1986). Consequently it was decided to see if an anneal like this would reduce the losses in the probe waveguides. In the fabrication process, after the core silicon oxynitride film was deposited, it was annealed in a nitrogen ambient at 1000°C for 3 hours before continuing the fabrication sequence. Figure 42 shows the subsequent results for the test structure.

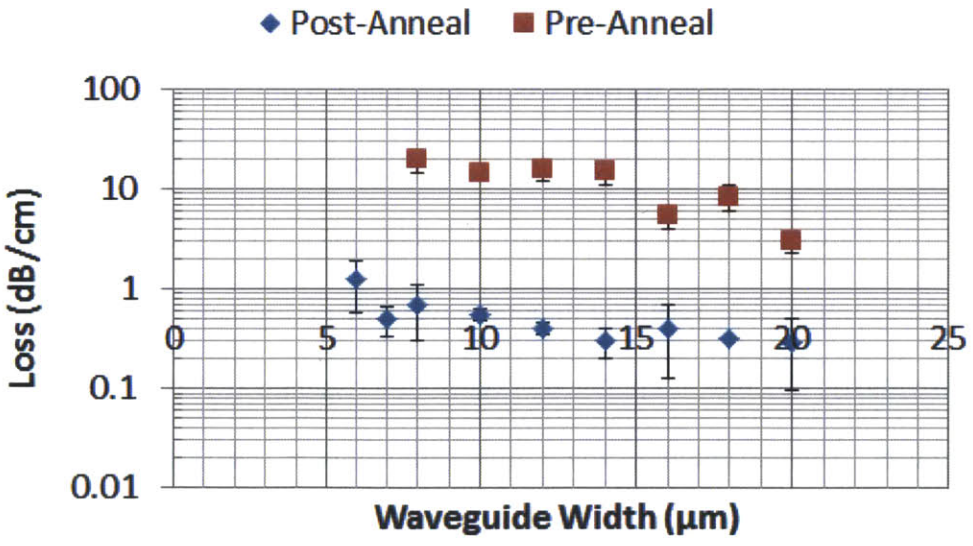

Figure 42 – Propagation loss as a function of waveguide width with and without an anneal step.

As can be seen, whereas ~3 dB/cm was the loss for a 20 μm wide waveguide pre-anneal, post-anneal, the loss in a 20 μm wide guide is 0.3 dB/cm and it is less than 1 dB/cm for guides as narrow as 7 μm wide. Of the loss mechanisms, the only one tested after annealing was the propagation loss. It was not necessary to test the input coupling loss and corner-mirror loss because Rayleigh scattering does not affect these.

The measurements presented are all for waveguides of 9 μm core thickness. This thickness is chosen to make coupling easier. The method of butt-coupling (simply pushing two fibers together and mode-matching the input and output) is the easiest of the coupling methods presented in Chapter 2. Because commercially available fiber assemblies (see Chapter 5 for explanation) utilize fibers of ~7 μm minimum mode-field diameter, the core thickness was chosen to be slightly larger (i.e. 9 μm). Given the data presented in Figure 42, the waveguide width was chosen to be 7 μm. Below 7 μm, there are too many defects from the difficulties of patterning such high aspect-ratio features. Therefore, the lengths of the waveguides were chosen to have a cross section of 7 μm X 9 μm. Theoretically, this cross section can be reduced to scales on the order of the diffraction limit in dielectric media. Below this scale, however, the localization of the electromagnetic waves to nanoscale regions would be impossible, resulting in poor waveguide performance (Chung et al., 2002). As stated previously, this was not pursued because of the complexity involved in coupling to such waveguides. The waveguides can be further miniaturized, well below the diffraction limit, using nanoplasmonics (Gramotnev & Bozhevolnyi, 2010). Relying on nano-scale metallic-dielectric boundary features, this allows for a much more localized field

distribution on scales far below the diffraction limit. The coupling necessary for this technology is even more complicated and, therefore, was also not pursued.

Chapter 4: Probe Definition and Assembly of Arrays for 3D Illumination

4.1 Single-shank Probe Fabrication

The fabrication of single-shank waveguide probes builds upon the previously described waveguide fabrication. The added fabrication steps involve silicon MEMS techniques used to define and release the probe from the substrate wafer. Before describing these fabrication steps, the target geometry for the waveguide layout will first be discussed here.

As will be described in greater detail in Chapter 5, the light-coupling path pursued for single-shank probes involves the use of multi termination push-on (MTP) fiber optic cables. MTP fiber optic cables are densely packed linear arrays of individual fiber optics.

The layout of MTP cables varies greatly (pitch, size, number, mode, etc.). For our purposes, single mode MTP cables (to match the mode-field diameter to the input aperture size) with a pitch of 250 μm were used (Figure 43). This pitch is standard for MTP cables.

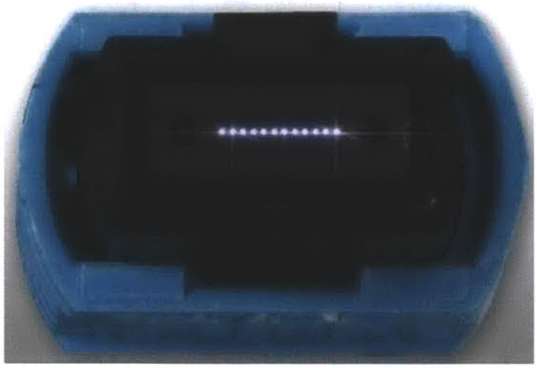

Figure 43 - MTP cable edge. This MTP cable (shown with light coming out of each fiber) is composed of 12 fibers with a center-to-center pitch of 250 μm between fibers.

The waveguide layout for single-shank probes involves an input region and a shank region (see Figure 44) (Zorzos, Boyden, & Fonstad, 2010). The input region is designed to maximally couple light from the source (via a MTP cable). The pitch of the 12 waveguides in the input section is 250 μm. The waveguide width at the input region is 15 μm. The waveguides taper to a width of 7 μm over a length of 300 μm. The waveguides converge in the input region to the densely-packed shank region. The radius of curvature for the waveguide bends is 750 μm (see Chapter 2 and 3 for theory and measurements behind bending loss). Along the length of the shank, the waveguide width is maintained at 7 μm and the pitch 10 μm (i.e. 3 μm of cladding between the guides).

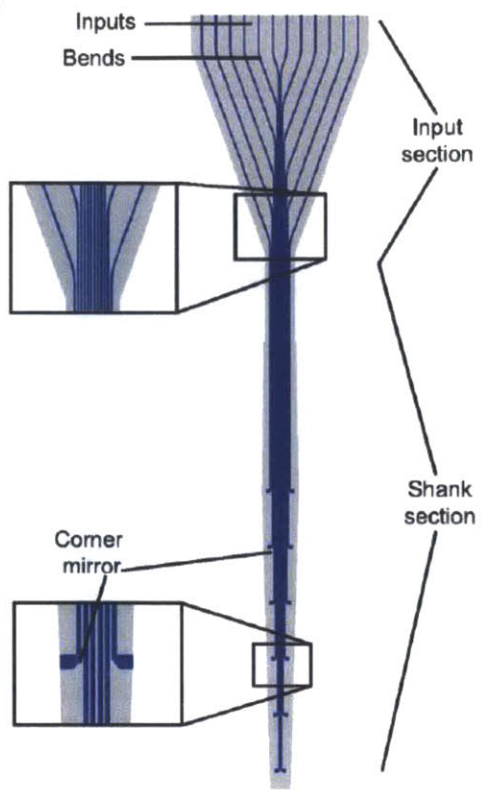

Figure 44 - Single-shank geometry with input section and shank section. Input region, converging bends, and corner mirrors are all labeled.

The 3 μm spacing between waveguides is determined to be large enough to avoid evanescent coupling between waveguides (see Chapter 3). At 10 μm pitch, the width of the shank body is ~10*N μm, where N is the number of waveguides. This value is approximate because there will necessarily be some small distance between the outer edge waveguides and the shank body edge. This is typically 5 μm on each edge.

Along the length of the shank, the waveguides terminate at right-angle bends (labeled as corner-mirrors). These right angle bends were described in great detail in Chapters 2 and 3. They serve to reflect light laterally from the shank at different depth locations.

After the waveguides are fabricated (via the process developed and discussed in the last chapter), the next steps are to define and remove the probe from the wafer substrate. A double-thick layer (20 μm) of AZ P4620 resist is deposited and patterned to open the last 5 μm of the input aperture and output apertures. The 0.5 μm layer of titanium is then etched in a hydro-fluoric acid-based solution (see Appendix A). This titanium removal is to allow for optical access to the waveguides for coupling and illumination delivery (Figure 45). The resist must be greater than 15 μm thick to insure complete coating of the waveguides, which have a height of 15 μm. As a single-thick layer of AZ P4620 is 10 μm, two layers are necessary (hence the 20 μm thickness).

Figure 45 - Titanium removed on sidewalls corresponding to inputs and outputs of the waveguides.

All fabrication is done on silicon-on-insulator (SOI) wafers. SOI wafers have a device layer and a buried oxide layer on a handle wafer. The handle wafer is a thick silicon wafer (usually ~650 μm thick for 150 mm diameter wafers), the buried oxide layer is a silicon dioxide typically on the order of several microns thick, and the device layer (top layer) is a uniform thin layer of silicon with a thickness selected depending upon the application. The SOI wafers used for single-shank probes have a device layer of 30 μm.

The reason for using SOI wafers is that they provide both a well-defined and uniform thickness and an etch stop layer (the buried oxide) to work with in silicon plasma etching.

A double-thick layer of resist is patterned, as before, opening a 50 μm wide trench, or 'halo', structure around the probe body. This halo shape defines the outline of the final probe geometry while significantly reducing etching non-uniformity caused by pattern dependent etching effects (Madou, 2012). The titanium layer is then etched away as before (Figure 46).

Figure 46 - The titanium is etched away within the halo-trench structure along the probe perimeter.

The 3 μm thick silicon dioxide layer (the top-cladding layer) is etched in a buffered-oxide-etch solution. The device layer is etched through to the buried oxide layer in an anisotropic plasma-based (sulfur hexafluoride) silicon etching tool (Figures 47 and 48).

Figure 47 – The 3 μm thick top-cladding layer is etched in a buffered-oxide etch solution.

Figure 48 – The device layer it etched through to the buried oxide layer.

A double-thick layer of P4620 is patterned on the backside of the wafer (back-side aligned) as a mask for etching through the handle wafer. This step is to thin the probes to an appropriate thickness (the device layer thickness) for tissue insertion. The SOI wafer is then reverse-mounted on a dummy-quartz wafer for further delicate handling and processing. Using a similar etch recipe as for the halo, the handle layer is through etched to the buried oxide layer (Figure 49).

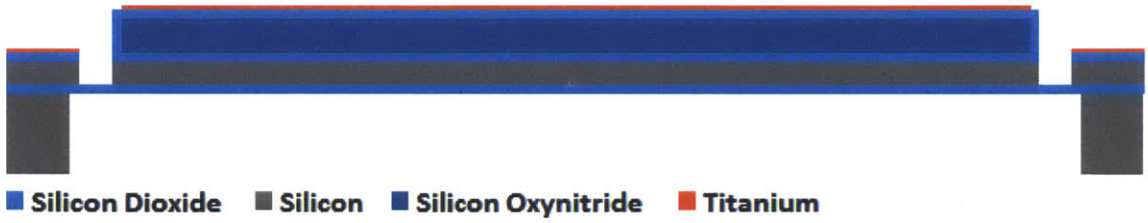

Figure 49 - The handle wafer is etched through to the buried oxide layer.

The probes are attached to the handle wafer from the buried oxide layer (largely untouched by the silicon etching) and the thick layer of resist used to mount the SOI wafer to the quartz wafer. First, the buried oxide layer is removed by holding the SOI wafer 1 cm from a 49%

hydro-fluoric acid bath for 30 minutes. This is to avoid submerging the bonded wafers in an oxide etching liquid bath, which would yield considerable undercutting and likely damage the waveguides. The mounted wafer is then submerged in an acetone solution over-night to remove the thick layer of photoresist holding the wafer to the handle (Figure 50). The probes are not floating in acetone at this point because of small, 100 um wide attachment bars between the bulk device layer and the probe. These are designed so that the probes remain attached, but can easily be removed mechanically without being damaged.

Figure 5 - The buried oxide layer is etched in a hydro-fluoric acid vapor. The wafer is subsequently released in a solvent bath.

4.2 Multi-shank Probe Fabrication

The fabrication of multi-shank probes is a simple extension of the fabrication procedure for single-shank probes. As you can be seen in the layout diagram in Figure 51, the waveguide layout for multi-shank probes is fundamentally similar to the layout for single-shank probes, the only main difference being multiple terminations and a multi-shank halo-structure.

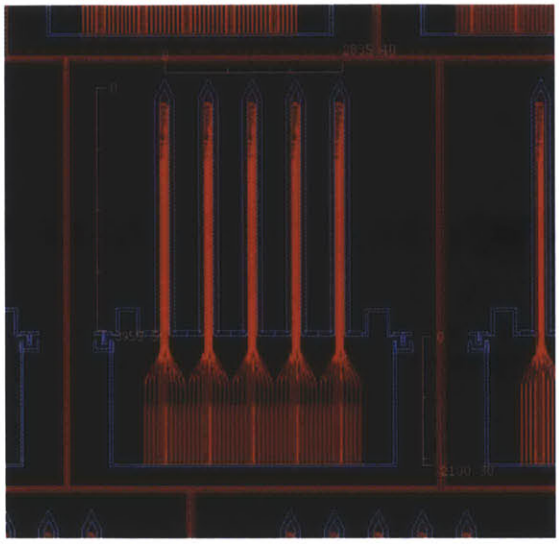

Figure 51 - CADENCE layout diagram for multi-shank probe (courtesy of Jorg Scholvin).

As will be seen in the following chapters, the spacing between shanks is a very important design constraint when fabricating multi-shank probe structures (whether they are linear arrays or 2D arrays). The damage ratio is here defined as the ratio of displaced tissue volume to the total volume of neural tissue being illuminated (assuming full illumination coverage). The displaced tissue volume is simply the total volume occupied by the shanks. Assuming the array is designed for full coverage, the volume of the neural tissue being illuminated can be taken as the volume spanned by the waveguides. The upper limit set for the damage ratio in the design was 0.01. Therefore, the minimum spacing between shanks on an individual multi-shank probe is entirely dependent on the spacing *between* multi-shank probes in the 3D array, the thickness of the probe, as well as the number of waveguides integrated onto a single shank. The prototype array being used for initial experiments has multi-shank probes separated by 300 μm, where each probe is 30 μm thick. The shanks along each probe are separated by 700 μm and there are 7 waveguides integrated

on each shank, yielding an individual shank width of 70 μm. This array, then, has a damage ratio of 0.01.

4.3 Assembly of Multi-shank Probes for 3D Illumination

An important goal of this dissertation is to provide a technology capable of arbitrary 3D illumination. The single-shank probes provide illumination along a single line (quasi-1D) and the multi-shank probes provide illumination along a single plane (quasi-2D). By assembling the multi-shank probes in a stacked format, the 2D illumination can be extended to a 3D illumination. This assembly method was largely developed by Dr. Jorg Scholvin in his development of 3D recording electrodes and was adapted as needed for waveguide probe assembly.

There are three required pieces for the assembly. First, as has already been described fully, there are the multi-shank probes. Second, a plate is needed to receive and support the multi-shank probes; this will be called a baseplate. Finally, there are a pair of alignment pieces to secure the probes to the baseplate and hold them vertically (Figure 52).

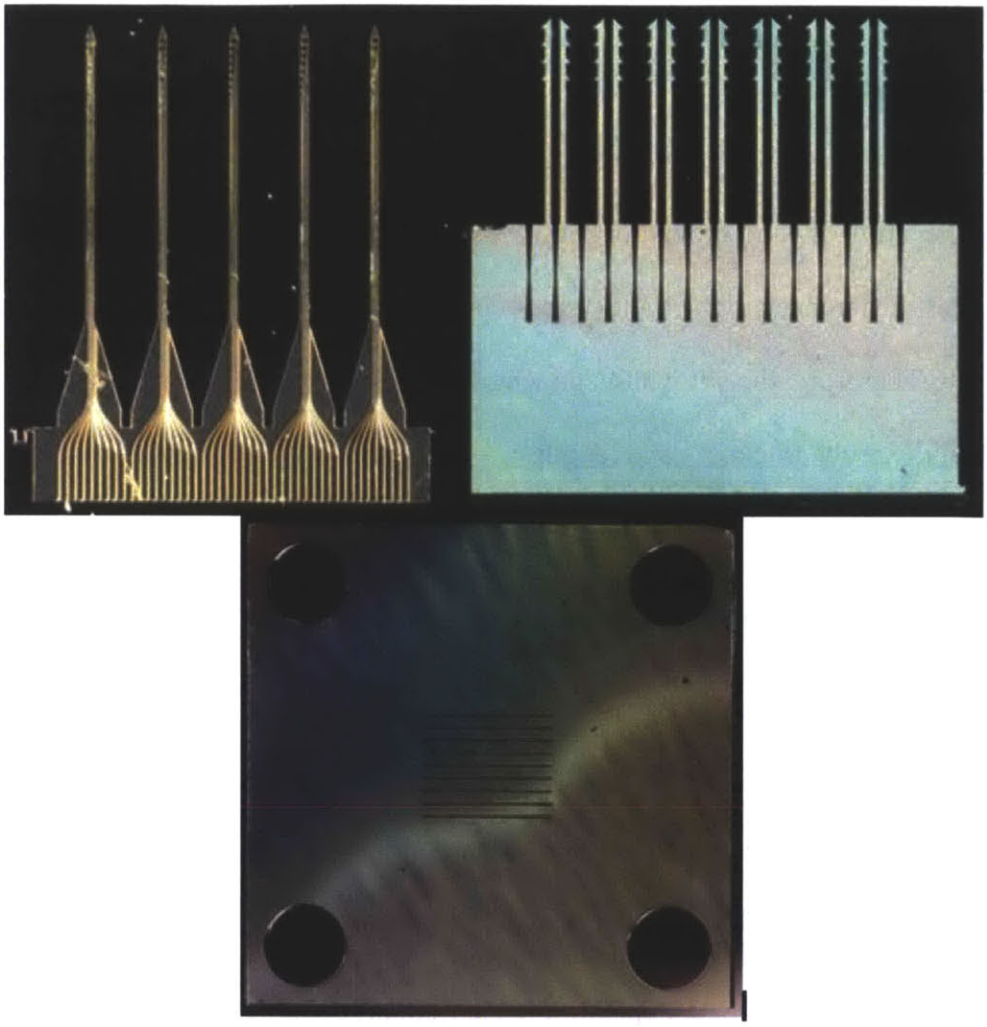

Figure 52 - Multi-shank probe (upper left), alignment piece (upper right), and baseplate (bottom).

The baseplate is a monolithic piece of silicon into which the multi-shank probes are inserted. The slits are shown in Figure 52 above. The large holes in the outer corners of the baseplate are there for attachment to a fiber bundle (as will be described in greater detail in the following chapter). The depth of the slits obviously matches the thickness of the silicon wafer used (675 μm), and the length and width match the length and width of the multi-shank probe. The width was carefully calibrated to provide enough room for minimal

waveguide damage, but small enough to minimize lateral and angular movement of the comb. The same is true of the slit length. To test the slit width effect, the probes were inserted, removed, and subsequently visually inspected for damage. The difference in size between the slit width and probe thickness was varied from 0 μm to 50 μm in steps of 5 μm. The smallest difference at which the probes could be repeatedly inserted without damage was 20 μm. Therefore, the slit width and length were subsequently fabricated to by 20 μm larger than the probe thickness and length.

The fabrication of the alignment and baseplate pieces is a simple process (see Appendix B for a detailed fabrication flow). In summary, a standard wafer bonded to a quartz wafer is etched through using a sulfur-hexafluoride based Bosch etch and a thick (8 μm) silicon dioxide patterned mask. The Bosch etch process involves a fluorine-based plasma chemistry combined with a fluorocarbon sidewall passivation deposition step (Abdolvand & Ayazi, 2008). The pieces are released in solvent.

When the combs are inserted into the baseplate (Figure 53), there is a significant amount of angular variation between combs. What is shown in Figure 54 is a top-side optical micrograph of the multi-shank probe tip positions. This, as well as side-view images, is the main method used to measure the angular variation in comb angular position across an array.

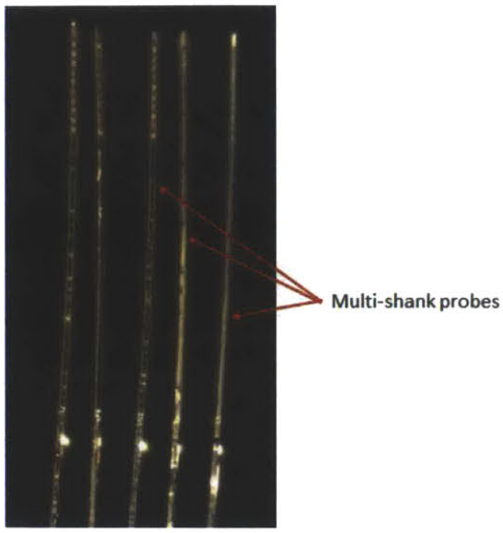

Figure 53 – Side-view of multi-shank probes inserted into baseplate without alignment pieces. Notice the angular variation between probes.

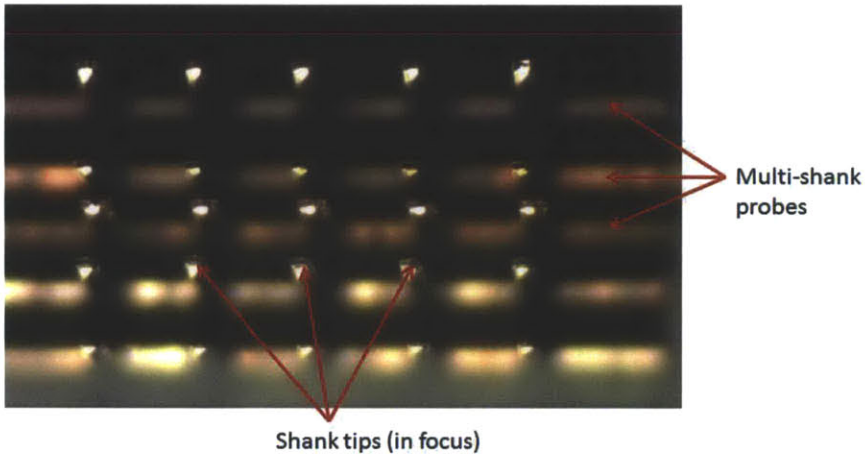

Figure 54 – Top-view of multi-shank probes inserted into baseplate without alignment pieces. The shank tips are placed in the focal plane of the imaging objective.

By measuring the tip lateral positions, we can translate that to comb angular positions. The comb angular position deviation is measured to be 1.8 degrees (standard deviation, n=25). This angular deviation is because of the amount of space given in the slit width. The

targeted difference between slit width and probe thickness is 20 μm. This space is necessary to avoid damaging the waveguides during insertion. The measured difference (using SEM cross-sections) is ~25 μm. Because the probes are 4 mm in length, this translates to a deviation in tip position of ~125 μm. For the purposes of biological experimentation, such positional variation precludes certainty in neural targets and is unacceptable. The purpose of the alignment pieces is to correct for this angular variation. The alignment pieces, as can be seen in Figure 52, have long tapered slits into which the multi-shank probe edges fit tightly. Each alignment piece makes contact with the multi-shank probe along one edge straightening it vertically without damaging the waveguides. The long toothed-tines serve simply to lock the opposing alignment piece into place once inserted. The probe angular position is measured to be 0.9 ± 0.3 degrees (standard deviation, n=10) after the insertion of alignment pieces. The offset of 0.9 degrees in one direction is not due to the alignment pieces, but rather is an artifact of the probe bending. This bending of the probes is visible in Figure 53. The silicon dioxide and silicon oxynitride films deposited induce a stress in the probe substrate that leads to mechanical bending. Although not yet done, this can be compensated for by depositing sacrificial films will opposing stresses. See Figure 55 for a cartoon schematic of assembly method.

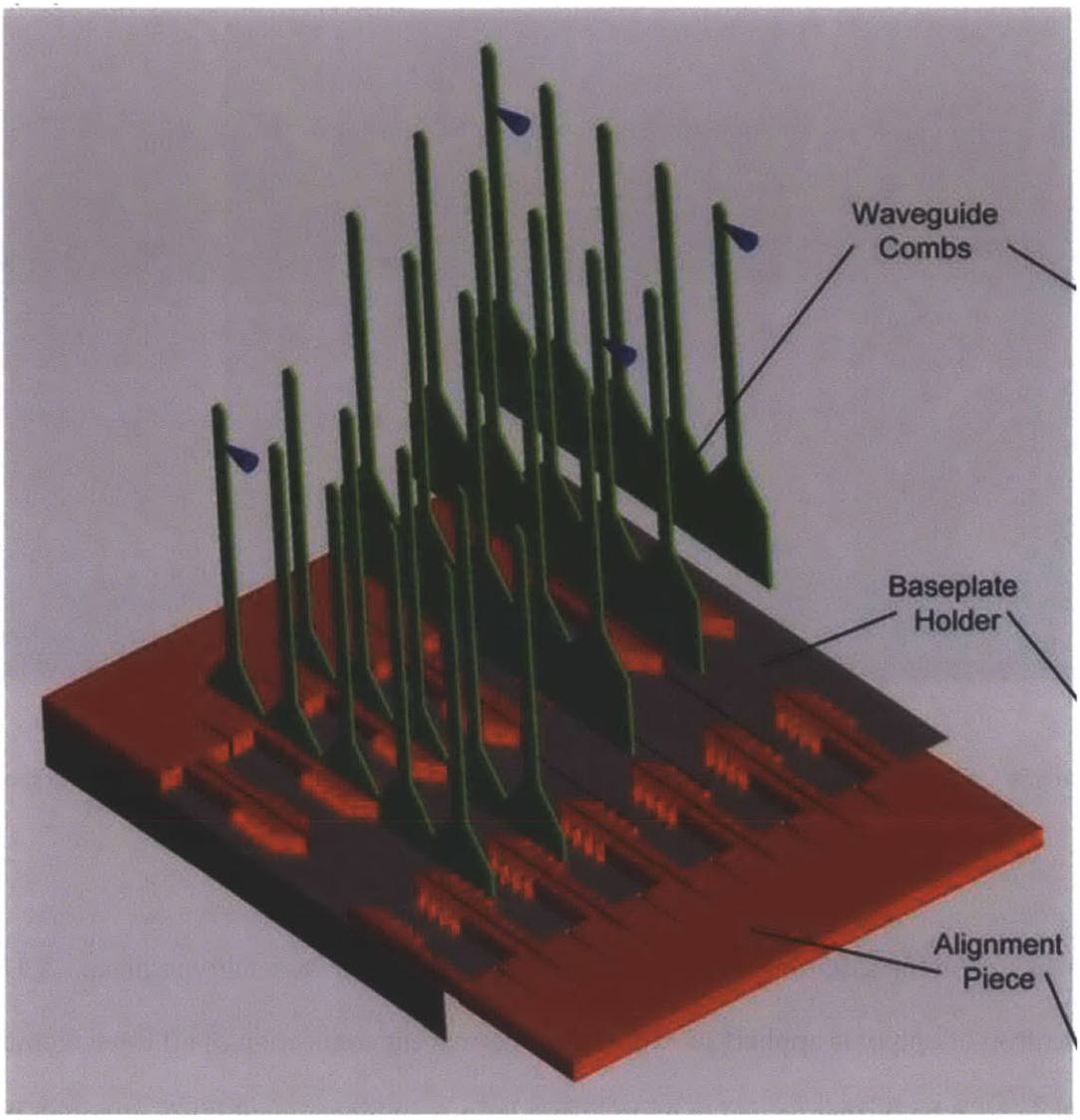

Figure 55 – Cartoon schematic of assembly method. Combs are shown docking into the baseplate holder, and the alignment pieces being fitted into place.

An SEM micrograph of an assembled array is shown in Figure 56. In this figure you can resolve all the major components: the alignment pieces, the baseplate holder, and the stacked multi-shank probes. The SEM also resolves the individual waveguides along the multi-shank probes.

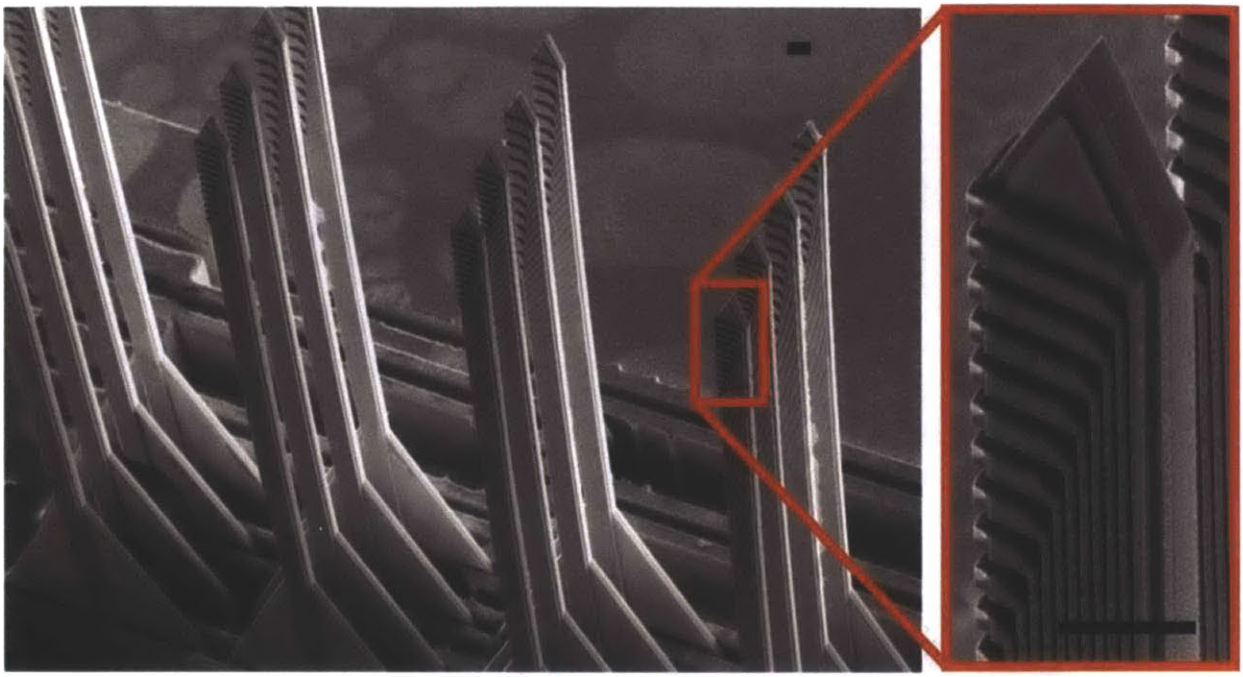

Figure 56 – SEM of 3D array showing multi-shank probes, waveguide details, alignment pieces, and baseplate. All materials (silicon, silicon oxynitride, and titanium) can be resolved.

The final step in the assembly process is to mechanically fix the assembly in place. A UV-curable drop of epoxy is applied an exposed for permanent connection of all three elements. The device can be further coated (e.g., to insure long-term biocompatibility), although the current device is fine for acute to medium term experiments, as non-biocompatible parts are external, and the device is sterilizable.

Chapter 5: Methods for Coupling Light into Assembled Arrays

5.1 Introduction to Chapter

The fabrication and assembly of an array of waveguide integrated probes capable of delivering light to arbitrary 3D patterns in tissue was described in the preceding chapter. In this chapter we address the issue of coupling light to this assembly (Zorzos, Scholvin, Boyden, & Fonstad, 2012). The goal is to couple light into the array in a way that allows for the use of these arrays to be used in neurological experiments and applications. We begin this chapter with a review of the light illumination characteristics needed for these experiments and applications: intensity, wavelengths, temporal wave form, etc.

5.2 Illumination Requirements

In Chapter 2, the issue of illumination requirement was touched upon. Specifically, it was stated that the target output power is 100 μW, which corresponds to an irradiance of 200 mW/mm^2 for an output aperture of 9 μm by 60 μm. As touched upon in Chapter 2, one of the methods pursued to understand how the fluence rate varied spatially in neural tissue was Monte Carlo simulation. The simulations referenced (Chow et al., 2010) was specific to a large optical fiber and was used to validate the 100 μW target output power. Further Monte Carlo simulations were conducted specific to the smaller rectangular output apertures of interest. The simulation is for neural tissue with elsewhere measured optical properties (Kienle et al., 1996), light of 473 nm wavelength, a an output aperture of 10 x 30 μm, an absorption coefficient of 0.4 cm^{-1}, a scattering coefficient of 350 cm^{-1}, and a density of 1000 kg/m^3. Figure 57 shows the results.

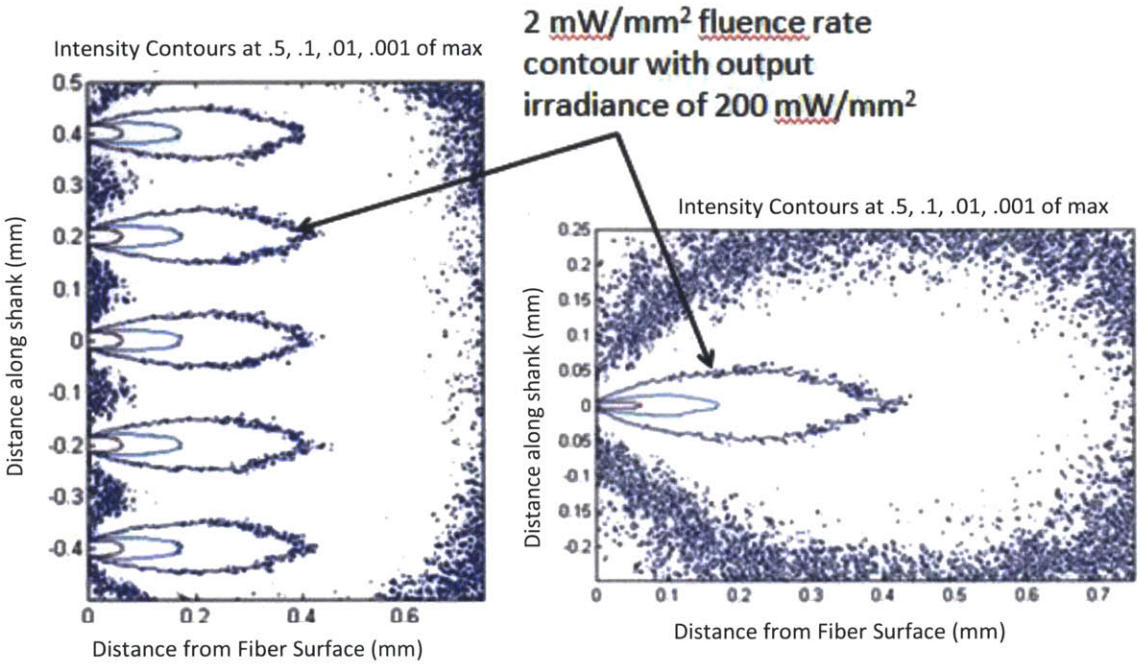

Figure 57 - Monte Carlo simulations, courtesy of Mike Henninger. Irradiance contours give a region of control for a given maximum irradiance at source.

The max fluence rate is at the output aperture (origin point on the plot). There are five apertures simulated simultaneously (pitch of 200 μm); the leftmost plot is of a topside view and the rightmost plot is of a side-view. As can be seen from the plots, the maximum fluence rate occurs at the output apertures. The contours represent stepped-down ratios of 0.5, 0.1, 0.01 (arrows), and 0.001. If the fluence rate at the output aperture is 200 mW/mm^2, then the four contours represent fluence rates of 100 mW/mm^2, 20 mW/mm^2, 2 mW/mm^2, and 0.2 mW/mm^2. The above fluence rate plots translate to plots of regions of control (the minimum irradiance at which opsin activation occurs is ~2 mW/mm^2 for most opsins in use). This is an important result to have before designing probes for experimentation. The

distance from the aperture at which neural activity can be controlled directly influences design constraints. Specifically, the desired goal is to be able to control all neurons in a given volume (full coverage) with no overlap between waveguides. These results were used to compare the optimal spacing of waveguide output apertures to the spacings chosen (along each dimension). Note that the simulations presented in this chapter are for an output power of 55 μW, whereas the targeted output power is 100 μW. Therefore, the fluence rate at any given point will be nearly twice what the simulation indicates. This optimization indicates a spacing of 100 μm as optimal, and that is the final spacing decided upon. Along the other dimensions, the waveguides were forced to be kept spaced somewhat farther apart to avoid too much neural damage. Specifically, between shanks (in the direction parallel to output aperture normal), the results yield an optimal spacing of 625 μm, where the actual spacing was set to 700 μm. Between the combs (in the direction perpendicular to output aperture normal), the results yield an optimal spacing of 200 μm, and the actual spacing was set to 300 μm. Therefore, because the Monte Carlo simulations reveal that the final engineered probe does not provide full coverage.

Now that initial experiments have been conducted (see Chapter 6) taking direct measurements of fluence rate and using 2-photon calcium imaging to directly measure neural activity around waveguide output apertures is being reinvestigated.

5.3 Delivery of Light to Array

5.3.1 Ribbon Fiber

The method of coupling to individual single-shank probes was touched upon in Chapter 3. Ribbon fibers are linear arrays of fibers with variable pitch, mode capacity, size, etc. The ribbon fibers used have a pitch of 250 μm and are single-mode with a mode-field-diameter of 12 μm. The ribbon fiber is on both ends terminated with an MTP connector, a standard connector used in the fiber-optics industry. An MTP fan-out cassette is attached to one end of the ribbon fiber. This cassette connects each individual fiber in the ribbon to an individual LC connection port (Figure 58).

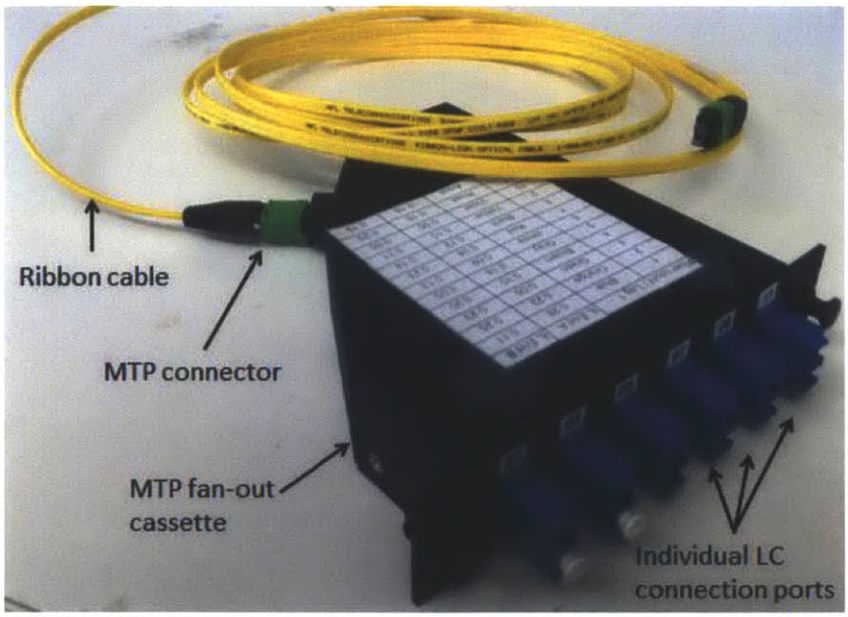

Figure 58 - MTP fan-out cassette with MTP ribbon cable connected. Each of the individual LC connection ports can be addressed individually for coupling to individual fibers in the ribbon.

Each of the individual LC connections ports can be connected to an individual light source for coupling to individual fibers in the ribbon cable.

One of the main components of an MTP connector is a metallic guide assembly, which is used to precisely mate female and male MTP connectors via metallic guide posts. Instead of mounting the single-shank probe directly to the MTP connector, it can be mounted to the guide assembly. This allows for modular attachment and removal of different guides without having to sacrifice ribbon cables. This is accomplished by (1) inserting the guide assembly, (2) aligning the single-shank probe to the ribbon cable (using three lateral degrees of freedom, and a single rotational) with the guide assembly in place, and finally (3) attaching the probe to the guide assembly with a UV-sensitive epoxy. Figure 59 provides an illustration of this coupling scheme.

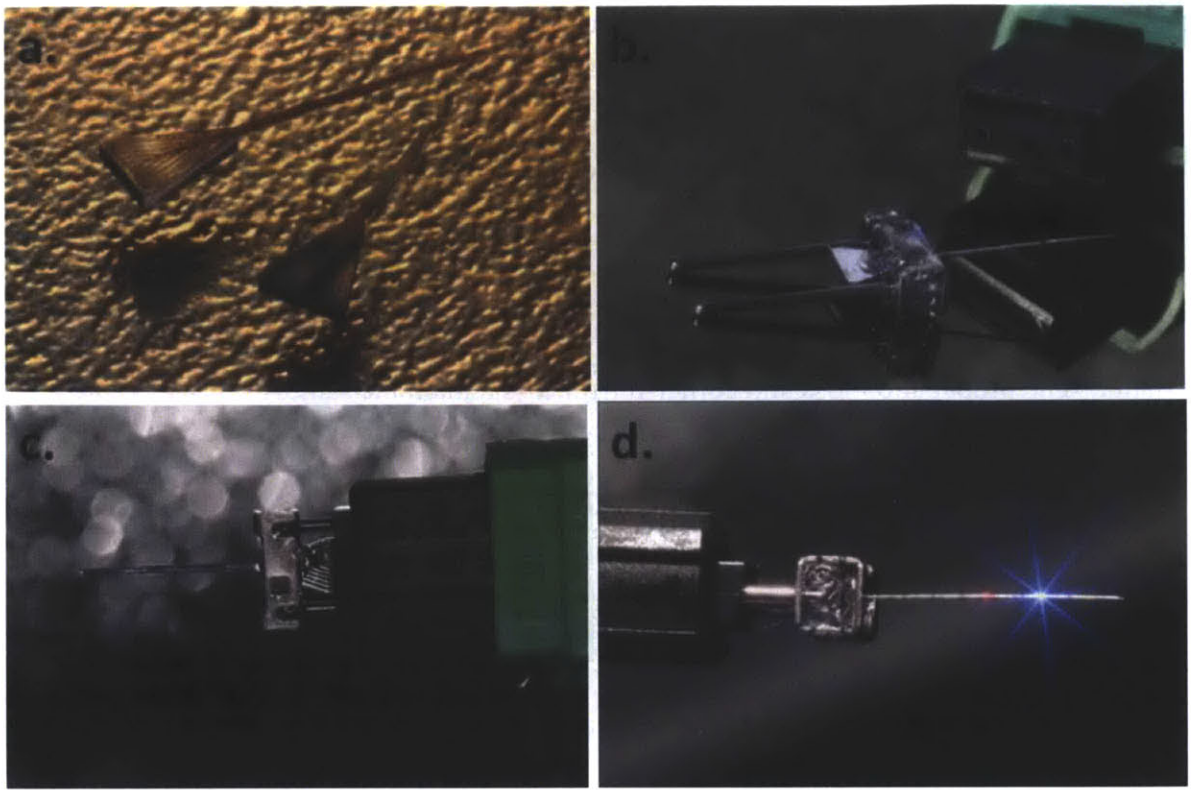

Figure 59 - a) Single-shank probe. b) MTP connector and single-shank probe attached to guide assembly. c) Single-shank probe attached to MTP connector via guide assembly. d) Side view of (c) with 473 nm and 633 nm light couple dto two separate waveguides. Blue light significantly higher power.

Using the cut-back method described in Chapter 3, the input coupling loss was measured to be 3.4 ± 2.2 dB. This is significantly larger, in amplitude and variation, relative to the single fiber butt-coupling used for the individual waveguide tests where it was only 0.4 dB. This difference is due to the larger diameter of the input fiber relative to the waveguide input aperture. For the single fiber measurements the mode field diameter of the input fiber was 5 μm, so the input fiber core was smaller than the waveguide input cross section. The mode field diameter of the fibers in the ribbon cable, however, were 12 μm, so the fiber core was larger than the waveguide input cross section, resulting in the mentioned increase in

coupling loss. A smaller core ribbon cable or a coupling lens array between the ribbon cable and waveguides could be used to reduce the loss. The coupling loss variation (2.2 dB) is due to geometric offset between the probe waveguides and the ribbon cable fibers. Because each waveguide is individually controlled by a laser source, there is enough power to overcome the increased coupling loss and a calibration can compensate for the large variation. The propagation loss and corner-mirror loss remain the same.

5.3.2 Scanning Mirror Galvanometer System

A galvanometer scanning mirror is an assembly of mirrors driven by galvanometer magnetic motors yielding the ability to, at high speeds, steer an individual laser beam (Figure 60).

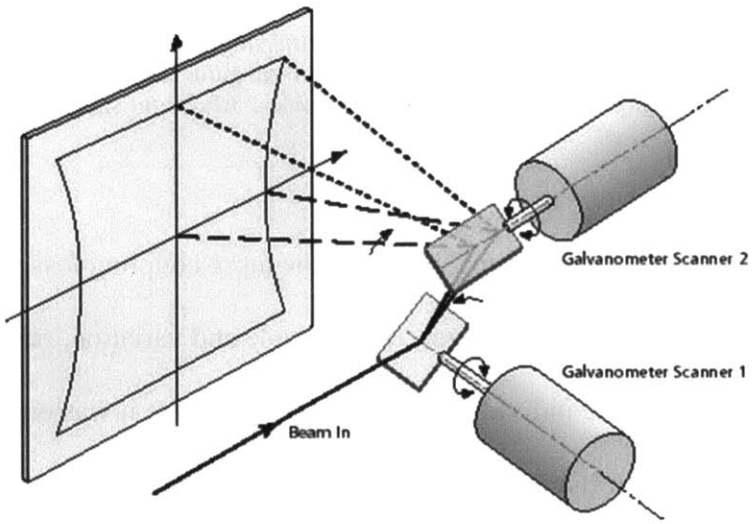

Figure 60 - Scanning mirror galvanometer illustration (Zamisel). Two separately controlled orthogonal mirrors redirect a laser beam.

Because two perpendicular galvanometer mirrors are being used, the incident laser beam can be steered in two dimensions. The overall idea behind using a galvanometer scanning

mirror for coupling to the waveguides is to rapidly raster between waveguides. The main disadvantage to this technique is that no two waveguides can be coupled to simultaneously; they can be switched between rapidly, but not simultaneously. The galvanometer used can cross field, ±20°, in under 100 μs. The coupling scheme in its entirety is shown in Figure 61.

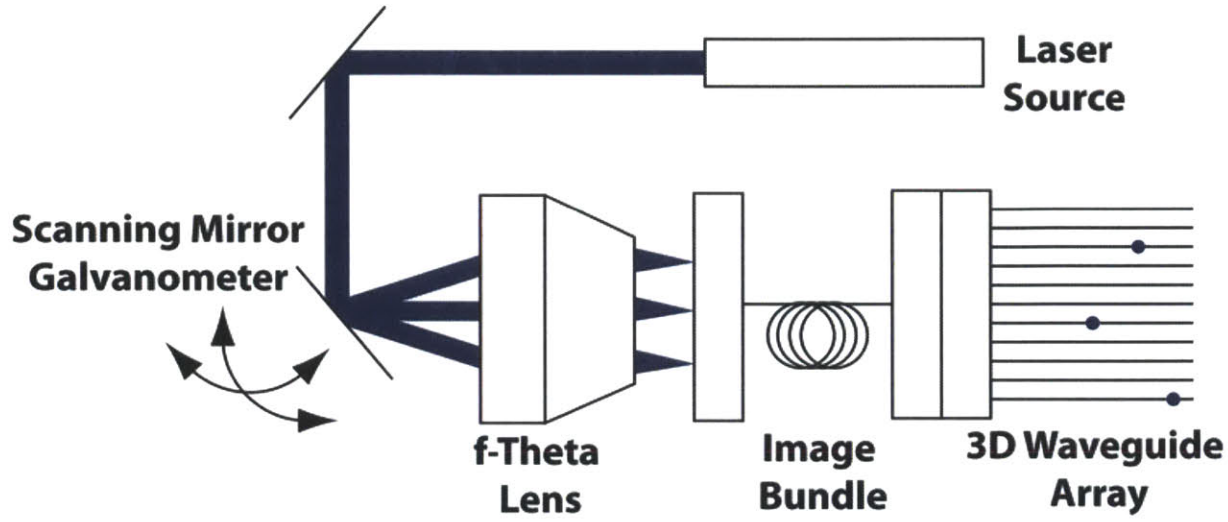

Figure 61 - Scanning mirror galvanometer based coupling setup.

F-theta lenses are commonly used in combination with scanning mirror galvanometers. They are telecentrically designed to have a flat focal plane. Angular incidence is translated to lateral position in the focal plane. Therefore, by changing the scanning mirror galvanometer position, different individual fibers in the image bundle can be selected. Note the spot size for the f-theta lens used is ~7 μm and it has an effective focal length of 18 mm. The individual optical elements in the optical path and their losses are shown in Table 3.

Optical Element	Loss Amplitude (dB)	Loss Standard Deviation (dB)
Mirror 1	0.0	0.0
Scanning mirror galvanometer	0.0	0.0
F-theta lens	0.0	0.0
Image Bundle	5	0.0
Waveguide input coupling with image bundle	3.9	2
Waveguide input coupling without image bundle (directly measured)	3.6	0.5
Waveguide propagation	0.4	0.1
Waveguide corner mirror	1.5	0.4
Total system (with image bundle)	11.9	2.5

Table 3 – Loss (dB) for each element along the scanning mirror galvanometer-based optical path.

As with the DMD system, the total system loss is for the system with an image bundle included. Two separate waveguide input coupling losses are reported: one with the image bundle and one without. The image bundle increases the input coupling loss to the waveguide, has intrinsic loss, and increases the variation for the input coupling loss. When comparing the system with and without an image bundle, the increase in waveguide input coupling loss, however, is not drastic (0.3 dB). This indicates that coupling to the image bundle and directly to the array yields significant loss (3.6-3.9 dB), when compared to the

highly efficient input coupling loss of 0.4 dB when using a butt-coupled single-mode fiber with a mode-field diameter of 5 μm. The free-space coupling method used here is the most-likely reason. Butt-coupling with a single-mode fiber of significantly smaller core size is known to be the most efficient coupling method.

See Figure 62 for an illustration of an example probe array with light coupled to 20 separate waveguides using the DMD-based system. Based on the losses presented, an input power of 1.6 mW will lead to an output power of 0.1 mW (i.e. 100 μW).

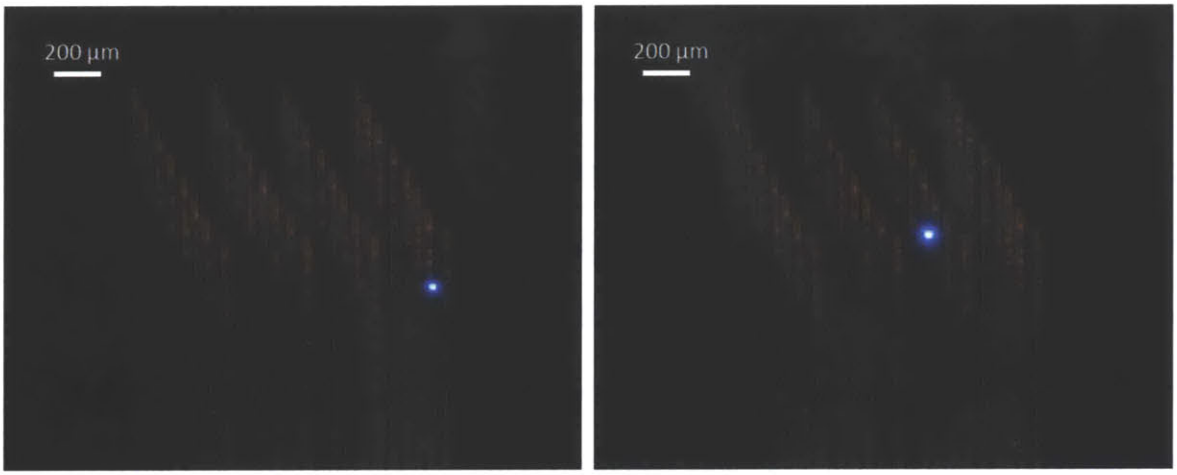

Figure 62 – Same example probe array with light coupled to an individual waveguide using the scanning mirror galvanometer-based coupling system. The galvanometer is oscillating between two different waveguides.

5.3.3 Digital Micro-mirror Device System

A DMD chip is a sub-technology of spatial light modulation (SLM) technologies. It serves to sculpt a light source both in time and space. It does this through the modulation of a massive array of individual micromirrors (pixels), each typically 8 μm square. Each mirror is digitally controlled and separated from neighboring pixels by 1 μm. Each

individual micromirror pixel element is digitally controlled into an 'on' or 'off' state. If a pixel is in the on-state, light is reflected down the optical path to target. If a pixel is in the off-state, light is reflected to a highly optically absorbent material to collect the unwanted light safely. By controlling the on/off-state of each pixel individually, any arbitrary 2D pattern can be applied to the illumination profile. The size of DMD chipsets varies from technology to technology, and which chipset is used depends on the resolution scale desired. For the purposes of this project, a 1024 x 768 chipset is used where each pixel is an 8 μm square. The chipset used is from Logic-PD and is a chipset with controller board. The pixel-micromirrors on/off state is digital in nature; the mirrors oscillates between ±12° relative to perpendicular. Therefore, the incoming illumination must be incident at the correct angle for the on-state reflections to reflect in the desired direction (in our case, perpendicular to the plane of the DMD). The DMD coupling system is shown in its entirety in Figure 63. The purpose of the light source being reflected from the third mirror (shown after the zoom-beam expander in the optical path) is to establish this necessary angle.

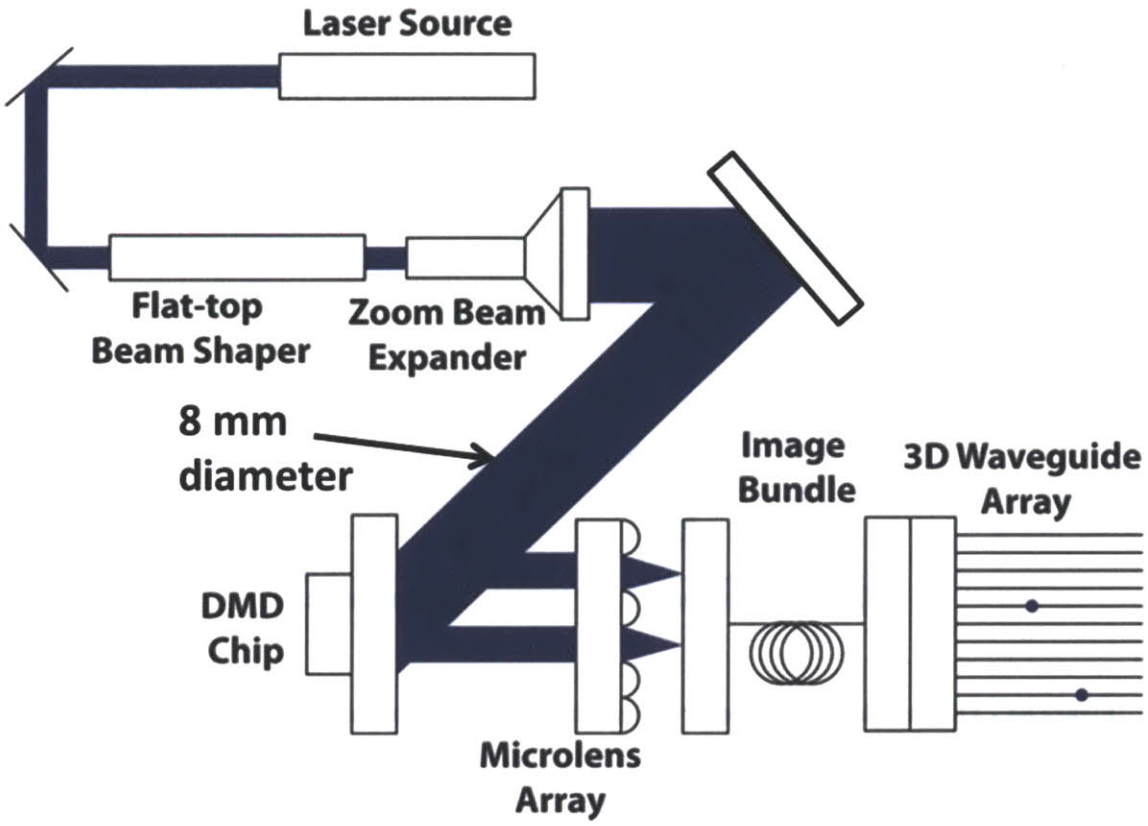

Figure 63 - Digital micromirror device (DMD) based optical coupling system.

Focusing a sufficient optical power down to individual fibers on the order of 10 μm can only be done with a coherent laser source. The laser source also needs to be high-power because the illumination covers all DMD micromirror pixels simultaneously. The source power must theoretically provide enough power for every waveguide to be utilized simultaneously. The laser source used is a 473 nm diode-pumped solid-state (DPSS) laser capable of providing upwards of 1.6W. This wavelength was selected because initial neurological experiments involve the use of the opsin ChR2, which has a peak sensitivity at ~473 nm.

The laser beam passes through a two-element beam shaping apparatus. First, it passes through a gaussian flat-top beam shaper and then through a zoom beam-expander. The Gaussian flat-top beam shaper serves to transform the input Gaussian-profile laser source into a flat-top-profile beam (Figure 64).

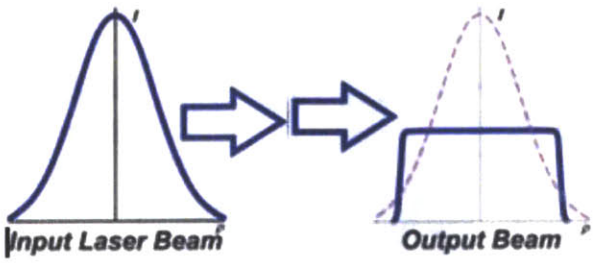

Figure 64 - The gaussian beam shaper transforms the input gaussian shape to a flat-top shape.

This is important to provide a uniform illumination profile across the DMD chipset and hence minimize variation in final output illumination across waveguides. The zoom beam expander is simply a refraction-based telescope used to expand the flat-top profile to optimal diameter. The optimal diameter is the minimum diameter at which all waveguides are covered. This value depends on the array being coupled to. For the current setup, the beam diameter is 8 mm.

For the DMD chip, as discussed, there is a line, with a defined angle, from which the illumination must come for the on-state reflection to be at the desired angle (perpendicular to chip). A set of two 2D kinematic mirror mounts are used for this purpose (Figure 63).

It will become clear after the losses for each of the optical elements is discussed that using the reflected beam from the DMD chip does not provide enough power, even with a

potential laser output of 1.6W. The reason for this deficiency is two-fold: (1) the losses associated with each element are too high, and (2) the illumination source must be spread out over a large portion of the DMD chipset. As most elements in the optical path have been optimized, the way around this power deficiency is to combine bundles of micromirror pixels per waveguide. A microlens array is used to accomplish this (Figure 65).

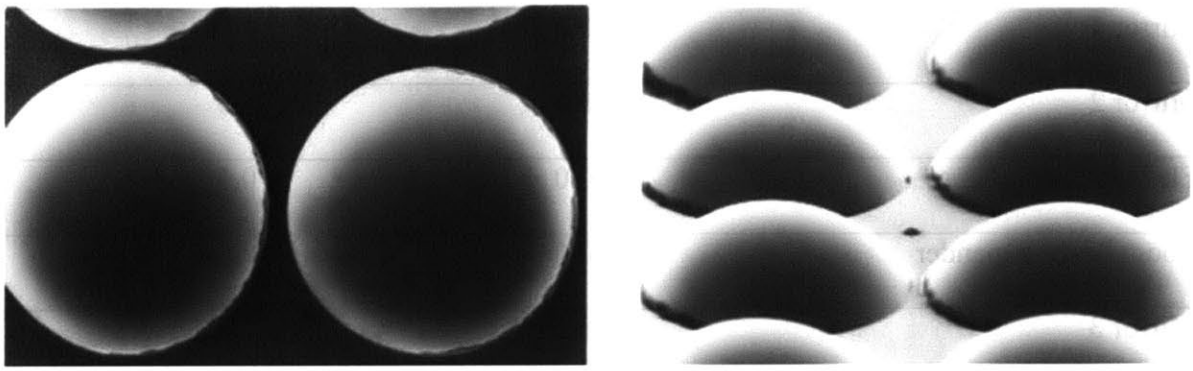

Figure 65 - SEM of microlens array. Lenslets are 290 μm in diameter with a pitch of 300 μm.

Held at a focal distance from the image bundle or probe array, a micro lens array is chosen to spatially match the input apertures of the probe array. The microlenses serve as collection optics, associating bundles of micromirror pixels to individual waveguides. The microlens array used is composed of 300 μm diameter lenslets, with an 8.7 mm focal length, and a divergence angle of 1°. A single lenslet collects the light reflected from ~1100 pixels. Because the lenslet array pitch is set at 300 μm, the highest density of input apertures for the probe array is 300 μm.

The loss mechanisms along the optical path are shown in Table 3. Each element on the table is associated with a part of the optical path shown in Figure 63. For the purposes

of this discussion, the loss for all four mirrors used (aligning through beam shaper/expander and aligning to DMD chip), the flat-top beam shaper, and the zoom beam-expander can be considered negligible.

Optical Element	**Loss Amplitude (dB)**	**Loss Standard Deviation (dB)**
Mirror 1	0.0	0.0
Mirror 2	0.0	0.0
Flat-top beam shaper	0.0	0.0
Zoom beam-expander	0.0	0.0
Mirror 3	0.0	0.0
Mirror 4	0.0	0.0
DMD	8.2	0.3
Microlens Array	0.2	0.0
Image Bundle	3.1	0.0
Waveguide input coupling with image bundle (inferred)	3.9	2
Waveguide input coupling without image bundle (directly measured)	3.1	1.1
Waveguide propagation	0.4	0.1
Waveguide corner mirror	1.5	0.4
Total system (with image bundle)	17.3	1.8

Table 4 – Loss (dB) for each element along the DMD-based optical path. Negligible quantities are represented by the * symbol.

The total system loss is for the system with an image bundle included. Note that two separate waveguide input coupling losses are reported: one with the image bundle and one without. The image bundle increases the input coupling loss to the waveguide, has intrinsic loss, and increases the variation for the input coupling loss. When comparing the system with and without an image bundle, the increase in waveguide input coupling loss, however, is not drastic (0.8 dB). This indicates that coupling to the image bundle and directly to the array yields significant loss (3.1-3.9 dB), when compared to the highly efficient input coupling loss of 0.4 dB when using a butt-coupled single-mode fiber with a mode-field diameter of 5 μm. As with galvanometer setup, the free-space coupling method used here is the most-likely reason behind the large coupling loss.

The fact that the DMD chip is a 2D array of periodically spaced mirrors means diffraction occurs in reflecting the incident beam (Figure 66).

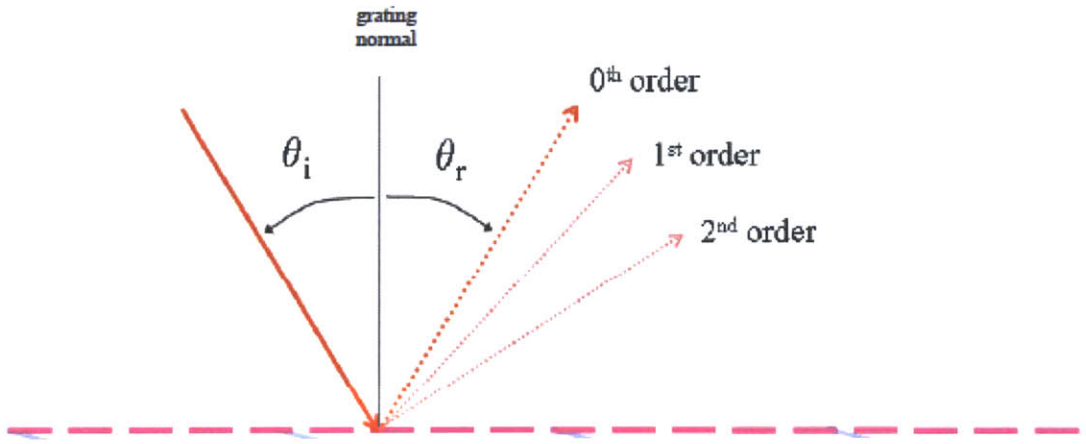

Figure 66 - Diffracted modes from the DMD chipset. The different diffracted orders contain different percentages of the incident beam power, where the 0th order has the highest (why it is the order projected).

As with standard diffraction optics, the dominant diffraction mode is the 0^{th} order mode. This is the mode projected, and contains ~15% of the power (corresponding to the 8.2 dB loss).

See Figure 67 for an illustration of an example probe array with light coupled to 20 separate waveguides using the DMD-based system. Based on the losses presented, an input power of 1.5 W spread out over 300 separate waveguides will lead to an output power of ~100 μW for each waveguide.

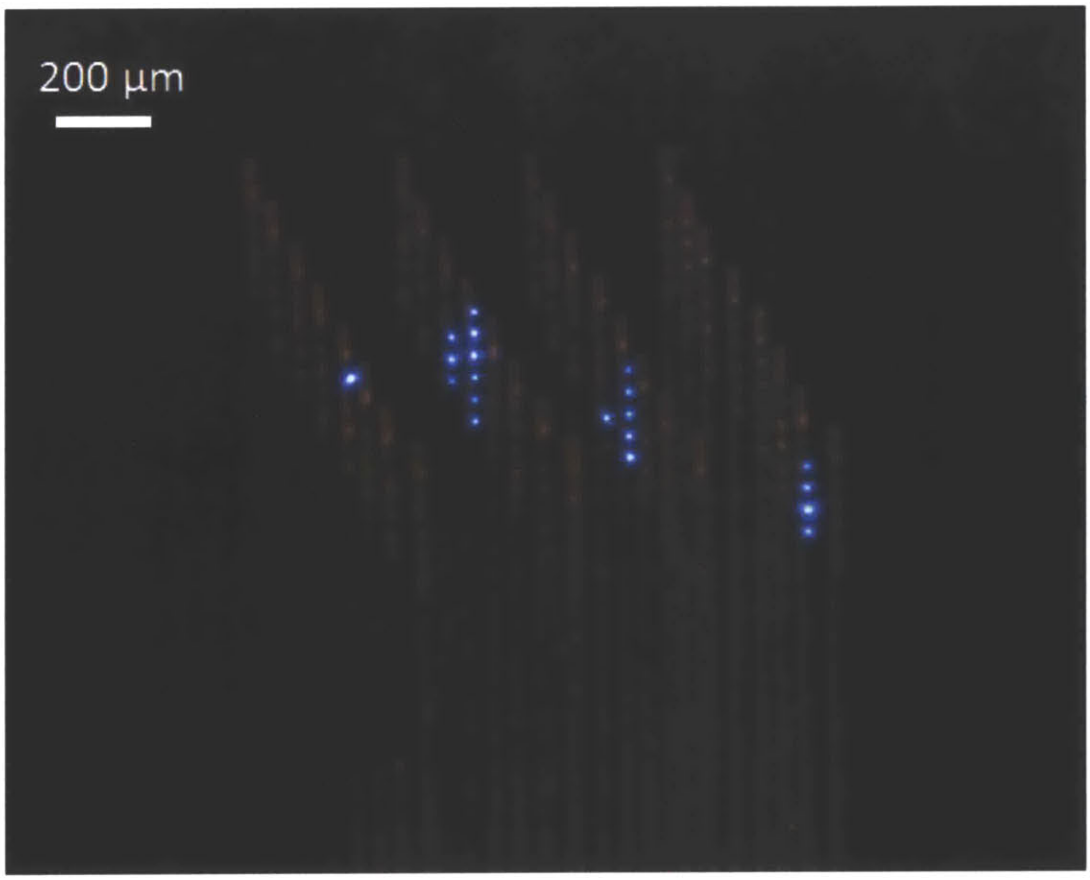

Figure 67 - Example probe array with light couple to 20 separate waveguides simultaneously using the DMD-based coupling system.

As a way of clarifying the DMD-based coupling scheme, let us walk through the optical path taking into account the loss at each step along the path. A laser of 1.6 W Gaussian laser beam is reflected off of two mirrors and passes through beam-shaping optics with zero loss. The transmitted beam has a flat-top profile with diameter 8 mm. After reflecting off of two more mirrors, the beam is reflected off of the DMD chipset, where it encounters a loss of 8.2 dB. The reflected mode is then a 240 mW, 8 mm diameter flat-top profile (a power density of ~4.8 mW/mm^2). Recall, one lenslet collects the light from ~1100 pixels (where each pixel has an area of ~7e-5 mm^2). Therefore, the power passing through each lenslet is ~370 μW. The lenslet provides a loss of 0.2 dB. Therefore, the power transmitted by each lenslet is ~350 μW. Without the image bundle, the sum of the coupling loss, propagation loss, and corner mirror loss is 5 dB. Therefore, the output power per waveguide in that case is ~110 μW. With the image bundle, the sum of the coupling loss, propagation loss, and corner mirror loss is 5.8 dB. The output power per waveguide in that case is ~90 μW. With or without the image bundle in place, the output illumination requirement is met.

5.4 Imaging Fiber Bundles

The backside of the assembled probe array is a 2D matrix of waveguide input apertures, and the task we are describing here is to couple light to each of those waveguides independently, keeping in mind that the array is designed to be used in a biological experiment. Such an experiment necessarily involves attaching the probe array to a stereotaxic stage system and inserting it into tissue. For this to be possible we must be able

to couple light into the array while it is not rigidly fixed in a predetermined positions. The way we accomplish this is to effectively extend the waveguides a long distance, via an imaging fiber bundle, from the probe array to a location off-site where stable and bulky optics can be set up. An imaging fiber bundle is a densely packed bundle of fiber optics. This is not entirely dis-similar to MTP cables as described in the previous chapter, however, on a much larger scale and in two dimensions as opposed to one. Fiber bundles can be composed of single-mode or multi-mode optical fibers. For the purposes of this work, a single-mode array of optical fibers is used. This is to match the input aperture size of the waveguides to the optical fiber mode field diameter. The image bundle fibers have a core of 8 μm, a pitch of 10 μm, and a numerical aperture of 0.63. The image bundle is so densely packed that there is bound to be spatial overlap between at least one fiber optic and any given waveguide (see image below). The challenge then becomes isolating that particular fiber optic on the distal end of the image bundle.

The coupling efficiency between a circular and rectangular waveguide is traditionally called fiber-waveguide coupling in the OIC community. Strictly speaking, to ascertain precise predictions of coupling efficiency, a complete modal analysis of both waveguides is necessary. The propagating field is a complex superposition of these modes. As a starting point, the equation below (Saleh & Teich, 2007) is for the simplified case of a slab index-step waveguide in 1-dimension.

$$E(y,z) = \sum_{m} a_m u_m(y) exp\,(-j\beta_m z)$$

Where E is the field profile, z is the propagation direction, y is the cross sectional dimension, a_m is the mode amplitude, um is the mode profile, and β is the mode propagation constant. The amplitude of each mode (a_m) is governed by the "modal overlap" between the source distribution and the input fiber (barring any subsequent perturbations). So, if we take an arbitrary 1-dimensional source field distribution, s(y), then (a_m), and subsequently the total coupling efficiency, is determined by the degree of similarity between s(y) and $u_m(y)$. For this particular problem, the coupling between two step-index waveguides of different materials/shapes in three dimensions, a numerical analysis is necessary to get accurate coupling coefficients. For the purposes of this discussion, the numerical analysis is foregone for direct measurement of the coupling efficiency. The ideal fiber-optic coupling system is an array of fibers, each with a core size smaller than the waveguide input aperture (10 μm X 20 μm), where the total number of fibers equals the total number of input apertures AND there is no lateral offset between each fiber and its corresponding waveguide. There are companies that can do this, but the cost (in time and money) is large. The secondary solution, as already described, is a Schott image bundle. Because only on the order of 1000 fibers are used, inherent to this system is an unnecessary bulk. Aside from that, we must note that although the pitch is specified to be 10 μm, there is randomness in fiber position. The reason for this lies in the manufacturing process. Schott starts with a template "multifiber" which is wound into the larger format bundle. Within each multifiber the pitch is precisely 10 μm, but between each multifiber there is a variance exceeding 5 μm in both dimensions. If 10 um were the consistent pitch between fibers, then any non-uniformities in coupling efficiency would be due to some parameter other than geometric offset. However, with the variance in pitch exceeding 5 μm, no such statements can be made, and it has to be

assumed that the 8 μm fibers from the image bundle will be "randomly" placed relative to the input apertures. In the wide-direction (20 μm direction) of the waveguide, it is guaranteed that a whole fiber lies in the aperture. In the thick-direction (9 μm direction) of the waveguide, it is possible that only half of the fiber lies in the input aperture (see Figure 68).

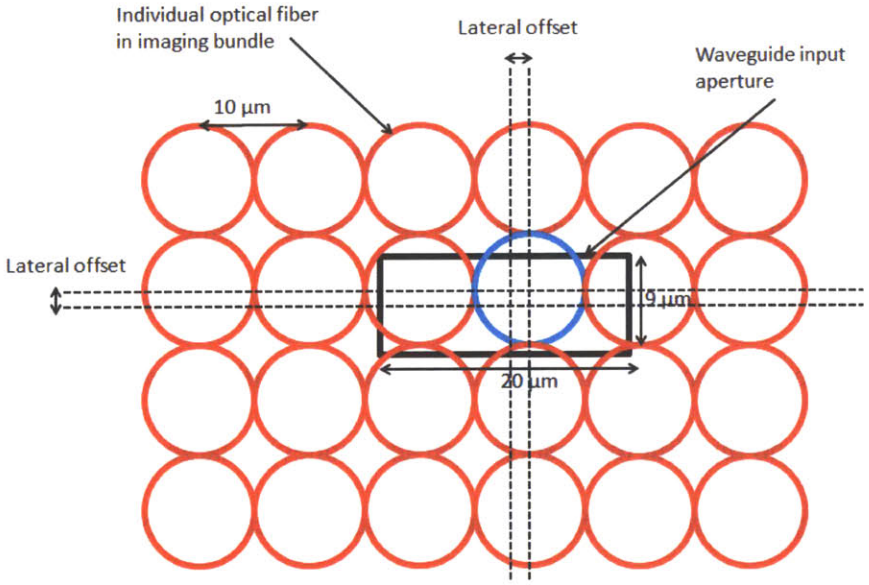

Figure 68 - Lateral offset of waveguide relative to fiber in image bundle. The multi-fiber imaging array has significantly more fibers thank there are waveguides in a 3D probe. Each waveguide is not guaranteed to center on an optical fiber in the imaging bundle, which contributes to a large variation in the coupling between the two.

5.5 Alternatives to Imaging Fiber Bundles

As discussed, there are issues associated with butt coupling the quasi-regular lattice image bundle to the probe array. Beyond this coupling issue associated with using the fiber

bundle, there is another reason to further engineer the system to avoid its use. The fiber image bundle has, depending on the format size, between $0.5x10^6$ and $1x10^6$ fibers. One fiber in the image bundle is associated with one waveguide in the probe array. If a probe array contains one thousand waveguides, that means only one in one thousand fibers in the image bundle are utilized. This is a large waste of bulk. The excess fibers add to the bulk of the connecting fiber assembly, and this precludes the use of the technology, as it is, in behavioral free-moving experiments. The obvious solution is to down-size the number of fibers in the image bundle to match the number of waveguides in the probe array. The key to achieving this is to spatially match the pitch (in both dimensions) of the waveguide input apertures to the layout of the fibers in the smaller 'fiber array'. Such fiber arrays do exist and can, in a custom-format, be made available (e.g. Silicon Lightwave Technology, Schott, and IDIL fibres). The manufacturing time and cost is large, however. Although difficult and costly, it is significantly easier to simply stack the 'multifibers' (described earlier in the chapter) in a dense format, as is the case for normal large-format image bundles. If a commercial solution is not soon made available, a potential area of future research could be in developing custom fiber arrays as described.

Although the issue of implanting light sources directly has been addressed, there is an alternative which could potentially provide a solution to the problems associated with image bundles and avoid heating concerns. Directly coupling an array of laser sources to the input apertures would eliminate the need for any connecting fiber optics, *and* it would avoid the heating issues involved with direct source implantation. With that said, having the light sources close to the brain may lead to unique heating issues. Recall the necessary source must be not-extended (a point source in nature). There are two source technologies

relatively well developed which could potentially fit the necessary parameters: vertical-cavity surface-emitting lasers (VCSELs) and edge-emitting laser diodes. These sources could be fabricated in several ways. First, all the processing could be done on the appropriate III-V substrate. The laser diodes (VCSELs or edge-emitting) would first be fabricated and then the waveguide integrated in later steps. The main disadvantages to this option would be the need to adapt the already established waveguide processing flow and the high-cost associated with wasting so much expensive III-V substrate. The second option would be to fabricate linear arrays, or 2D arrays, of laser diodes and subsequently directly coupling those to the multi-shank probes or the entire probe array. Most likely, if arrays of edge-emitting diodes were to be used, then directly coupling to multi-shank probes would make the most sense, and if VCSEL arrays were to be used, then directly coupling to the entire probe array would make most sense. With that said, however, one could imagine hybrid technologies and integration schemes which would mix-and-match. The third and final option is to create pill-form laser diodes and further develop integration methods for integrating the diodes directly to the input regions (Famenini, 2012).

Chapter 6: Conclusion

6.1 Preliminary Biological Experiments

6.1.1 Motivation

The main part of this dissertation is the development and characterization of a specific technology. The last 9-12 months of this thesis work has involved the application of the described technology. This serves three main purposes. First, by stopping the engineering development and implementing the technology, this allows for a design-reflection and future improvement. In using the technology, it becomes *significantly* more apparent how the technology can be improved, both from an engineer's standpoint and a biologist's. If this technology is going to have maximal impact, then that is an important point. The tool must be easily usable both by trained engineers as well as biologists and neuroscientists. The second reason to stop the technological development and perform

biological experiments is scientific in nature. This technology is a fundamentally new tool engendering new ways of performing neuroscientific experiments. We are interested in scientific discovery as well as tool development, so this is a natural pursuit. The third, and final, purpose behind pushing into biological experimentation is the power of demonstration. Even with a cogent and strong argument behind the technology, it is only after its efficacy and usefulness have been demonstrated *in context* that the larger biological/neuroscientific community will become interested enough to adopt the technology as a new experimental paradigm. Obviously, this is not a hard rule, simply an observation made over the course of this work.

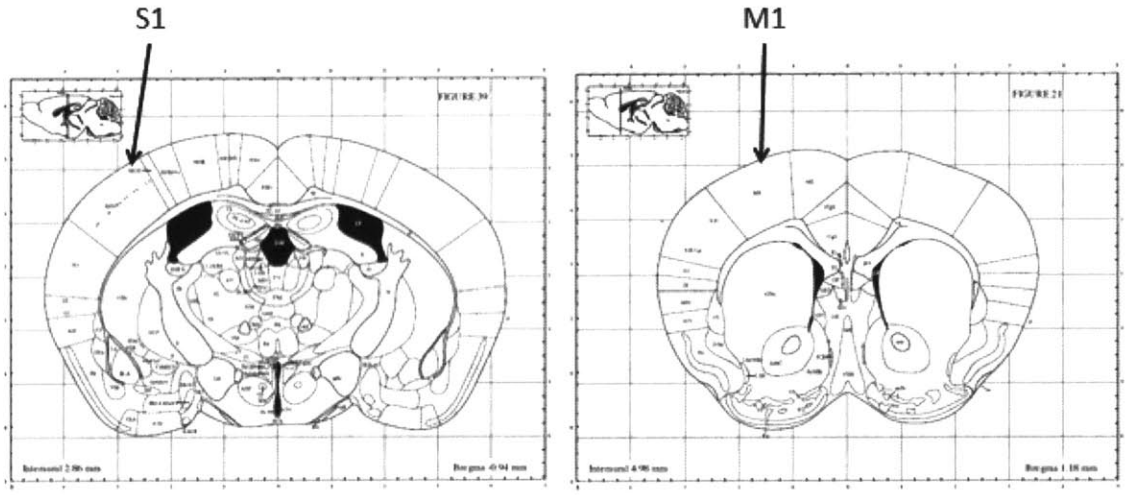

Figure 69 – Mouse atlas diagrams with S1 and M1 labeled (Sunkin et al., 2013).

The experimental method involves simultaneously delivering light in S1 (via the probe array) while recording neural activity in M1. The patterns delivered to S1 can be compared to the patterns recorded in M1 (Figure 69).

6.1.2 Experimental setup

The scale of the primary somatosensory cortex can be seen in Figure 69. The probe array assembled is designed to fully cover this region. The pitch between multi-shank probes is 300 μm, and the pitch between individual shanks along a single multi-shank probe is 700 μm. The array dimensions are 4×5, yielding coverage of (0.9 mm × 2.8 mm). This guarantees full coverage of S1. There are 10 waveguides along each shank, yielding a total of 200 delivery points in the array. This can be scaled up (as demonstrated in previous chapters). The coupling method chosen is the galvanometer-based setup. The experimental setup is shown in Figure 70.

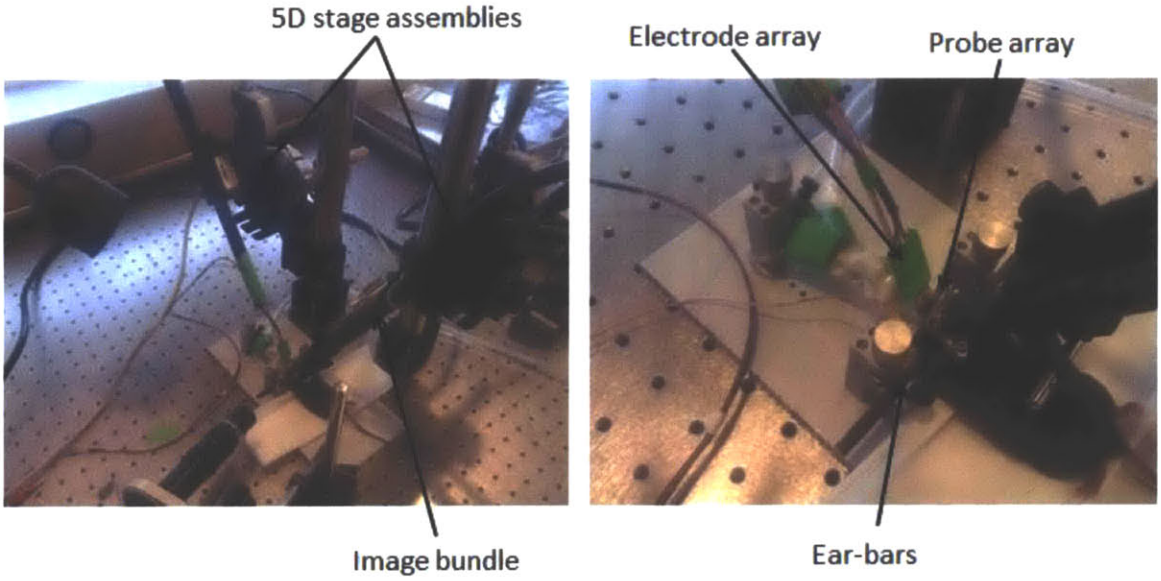

Figure 70 - Experimental setup showing custom-made stage assemblies, electrode array, and probe array

The silicon electrode array used was purchased from Neuronexus. The electrodes are circular and standard PtIr coated with areas of 177 μm^2. Two formats were used: a linear

array of 16 electrodes with a pitch of 100 µm and a 4×4 tetrode style format. Both formats are shown in Figure 71.

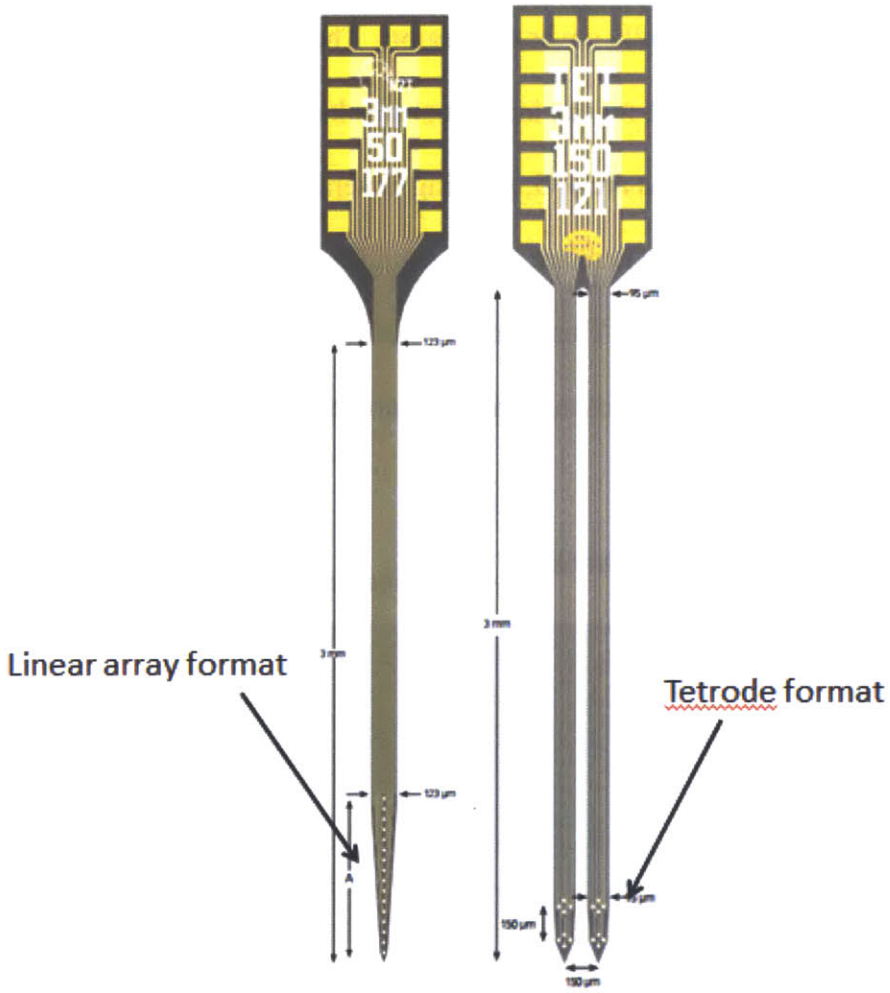

Figure 71 - Both neuronexus formats used: linear and tetrode (courtesy of Neuronexus).

The electrode is connected to an Intan evaluation system. The evaluation system is composed of a small amplifier board and a USB interface board (Figure 72).

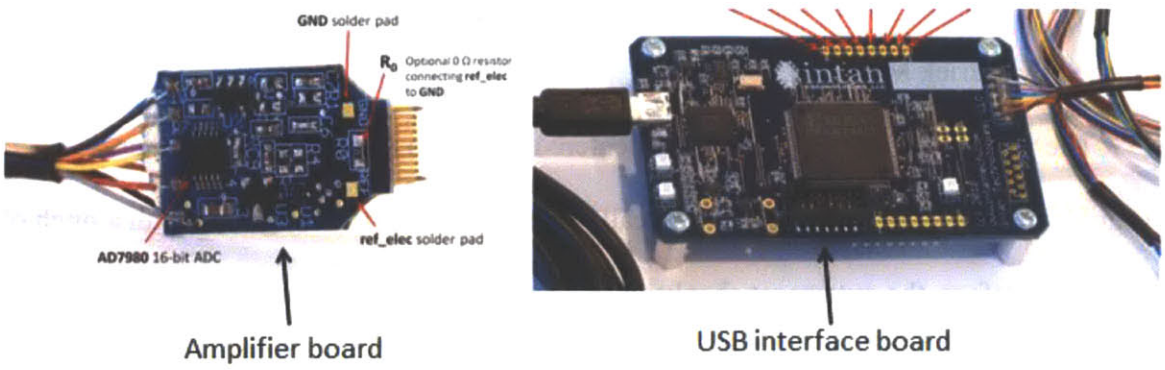

Figure 72 – Intan USB interface board and amplifier board to which the neuronexus electrode array is attached.

The system directly writes the signal to disk at a sampling rate of 25 kHz. The recording software used is also developed through Intan.

Both the probe array and the silicon electrode are mounted to custom-made 5D stage assemblies. The stage assemblies are assembled entirely from off-the-shelf Thor parts. There are three orthogonal manual stage assemblies, a rotational degree of freedom (rotating the axis of insertion), and a motorized linear stage along the axis of insertion.

Cell-specific promoters and customized viruses for genetic targeting were utilized, as well as the use of germline transgenesis for permanent gene transfer. These 'transgenic mice', as they will be referred to throughout this work, avoid many of the costs and difficulties associated with using viruses for opsin expression. Both expression methods were used in this work.

A large craniotomy is performed over the S1 region for access by the probe array, and a small hole craniotomy is performed over the M1 region for access by the silicon electrode probe. The mouse cranium is held in place by gluing a single shank to the cranium

and holding it in place with a bar assembly. All virus injections and craniotomies were performed by Patrick Monahan.

The waveguide array is implanted, centered on S1, so that the topmost outer waveguide is just below brain surface. Recall, each shank has 10 waveguides with a pitch of 100 μm. Therefore, the outermost shanks of the waveguide array span ~1 mm and go ~1 mm deep. The centermost shanks, span the same distance, but penetrate deeper. This variation in penetration depth is due to the curvature of the brain. The waveguide layout for the array is rectangular in nature, which does not fit with the curvature of the cortex. In future iterations of the technology, the waveguide layout can be designed to match the curvature of whatever region is being addressed. Another consideration during implantation is dimpling of the brain. Although the array is designed to occupy a minimum amount of space, there is still a tissue-probe friction which leads to a dimpling of the brain. There are several potential solutions to this problem. First, in designing the waveguide probe, the shanks can be designed to be different lengths. During implantation, then, instead of many shanks impacting the brain surface simultaneously (increasing force), only one would make contact at any given time. This would allow for separate penetration, and a lower force at any given time. This method was conceived of by Matt Wilson and Jorg Scholvin. Although this addresses the issue of penetration force, there is still a friction force associated with probe-tissue relative movement after penetration. The smaller the displaced volume, the less this friction force will be. So, that is one solution, to simply make the shank bodies smaller. Another solution is to alter the dynamics of insertion. For a large portion of the history of neuroscience, it was believed slow implantation is best for recordings. However, there is a growing consensus that, due to the viscoelastic properties of neural tissue,

extremely fast implantation is beneficial (Jensen, Yoshida, & Hofmann, 2006). Instead of slowly lowering the probe into place over a long period of time, ballistically (or otherwise) driving the probe is superior. Because these procedures have not been optimized by the lab, and are currently underway, the dimpling issue is one to keep in mind.

The ground and reference electrodes are tied together and connected subcutaneously near the edge of the craniotomy. The silicon probe is implanted so that the electrodes span the cortex. The silicon probe is adjusted to maximize the number of neurons which can be isolated. Both the silicon probe and the waveguide array are allowed to settle for a minimum of 30 minutes prior to starting the light delivery.

With the electrodes and waveguide in place, the delivery protocol is started while recording. Two separate delivery sequences are delivered: first, a random sequence, and then a sequential delivery. The random sequence delivery involves taking 200 random samples from the set of waveguides with replacement. Each sample is a 6 ms pulse with an output irradiance of ~150 mW/mm^2, with no latency time between samples. Therefore, each trial is 1.2 seconds in duration. The latency time between trials is 2 seconds (where no light is being delivered). Each trial is a new random sampling; 1400 trials are repeated. The sequential delivery involves delivering pulse trains of different frequency to each waveguide separately. The frequencies delivered are 2 Hz, 4Hz, 10 Hz, 20 Hz, and 40 Hz. To make sure each frequency pulse train is delivered to each waveguide five times, 5000 separate trials are delivered. The laser and galvanometer control program for delivering these two separate sequences was written in MATLAB by Tim Buschman. Figure 73 shows the waveguide array (and electrode shank) during a delivery sequence.

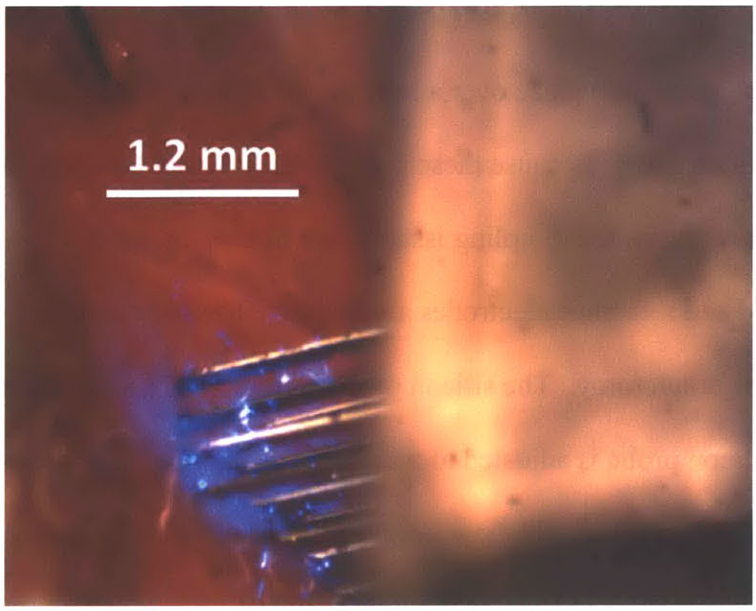

Figure 73 - Inserted Probe array and electrode array (upper left) during a light delivery trial.

6.1.3 Pre-processing

Before getting to a description of the analyses and results, the pre-processing steps should be described. Also, it should here be noted that I conducted the pre-processing and subsequent analyses in close collaboration with Tim Buschman.

The first pre-processing step is to notch filter out any unwanted frequencies dominating the signal. In this case, the predominant frequency to be filtered out is 60 Hz noise. The signal is then high-pass filtered (Chebyshev). The analysis conducted to-date is largely working with single-unit activity.

The next pre-processing step is to re-reference the signal to the overall average. Recall, the silicon probes being used have 16 recording sites. The 16 separate signals are then combined into trode format. In the case of the tetrode-layout silicon probes, this is a

natural step. In the case of the linear-layout silicon probes, this is not an obvious step, but still performed.

After combing the signals into trodes (tetrodes), each individual spike waveform is extracted. The signal is thresholded at four standard deviations, and the signal is extracted 1 ms prior and 1 ms after the event maximum. This event is taken as a single unit spike.

The final step (prior to the analysis on single-unit activity) is to sort the spikes. The measured activity on any given electrode is multi-unit activity. To separate the detected units into separate single-units, a spike sorting method is used (principal component analysis). The spikes are plotted in principal component space and clustered according to their direction of maximum variance.

6.1.4 Preliminary Analysis

As stated previously, although the pre-processing was done on all data taken, the analysis done to-date is on the random-sequence delivery data alone, not the sequential delivery. Furthermore, the analysis only involves the high-frequency multi-unit activity.

Figure 74 is a plot showing the z-score of activity relative to baseline in the case of a transgenic mouse expressing channelrhodopsin-2 for a linear array electrode.

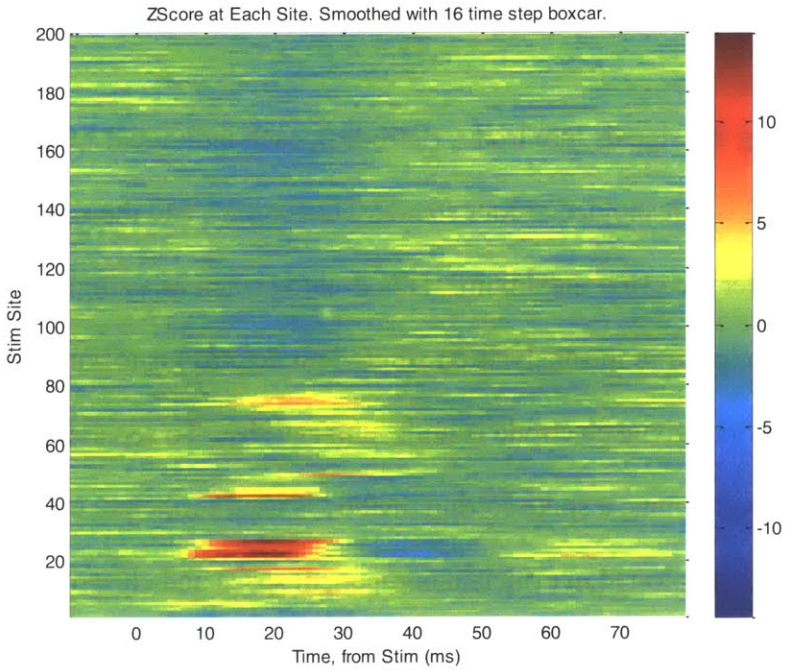

Figure 74 - Zscore of spiking activity relative to baseline for each stimulation site relative to stimulation onset.

The color plot is activity represented by z-score relative to baseline, where baseline is the inter-trial interval with no light delivery. The different stimulation sites are represented on the vertical axis, in this case 200 different sites. The horizontal axis is time, in ms, relative to stimulation onset, where the stimulation pulse is 6 ms.

As a way of combing through the bulk of the data to assess whether there is a statistically relevant effect, the percent explained variance (PEV) is used. The PEV is a measurement of what percent the variation in a data set can be accounted for by a particular model. By repeatedly randomizing the model and calculating the PEV, we establish a null hypothesis to which the PEV for the data set can be compared (Figure 75).

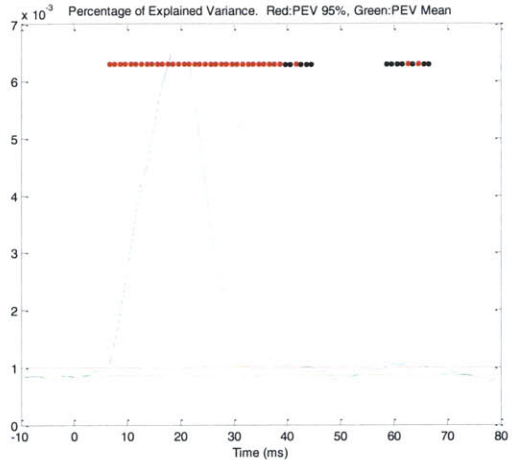

Figure 75 - PEV as a function of time for a single day and trode. 95% and 99% are plotted in green and red respectively.

The red dots in the above figure show where the p-value goes above 99%, and the black where it goes above 99%. In doing this PEV analysis, it is obvious there is a strong statistically relevant effect centered at ~20 ms after stimulation onset, and a weaker, but still relevant, effect centered ~65 ms after stimulation onset. Figure 76 shows a summary plot of all experimental trials and all trodes, where the color plot is of a thresholded p-value. This is a good way of visualizing both if there was a statistically relevant effect, and also when that effect occurred for all experiments conducted.

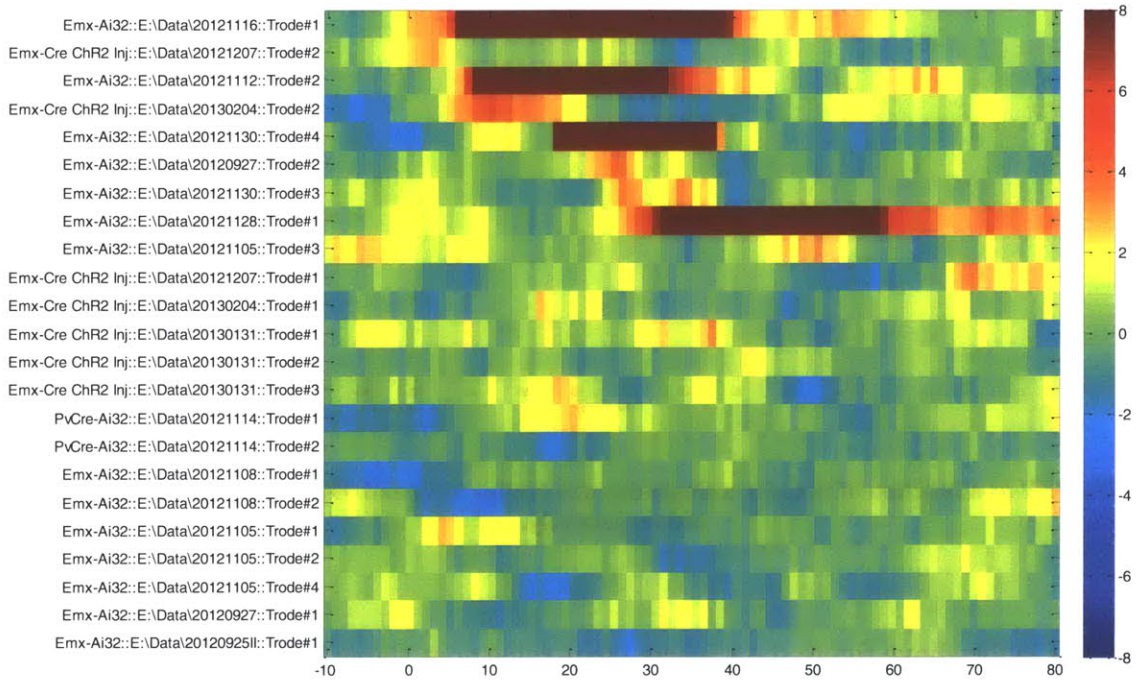

Figure 76 – Thresholded PEV plotted for all trodes and all trials conducted.

6.2 Concluding Remarks

6.2.1 Summary

This dissertation work has involved the development, characterization, and initial utilization of a technology capable of delivering light to arbitrary 3D targets in neural tissue. The work progressed from initial theoretical considerations and heating simulation results, through preliminary waveguide fabrication and testing, to waveguide integration on probe

geometries. The coupling schemes used to couple to the assembled 3D geometries were then discussed and characterized. Finally, the arrays were demonstrated in biological testing.

Silicon oxynitride core, silicon dioxide cladding waveguides were fabricated with a propagation loss of ~0.4 dB/cm and an input coupling loss of 0.4 ± 0.3 dB (for a butt-coupled individual single mode fiber butt). The core had a cross section of 9 x 7 μm and an index of refraction of 1.53. Negligible bending losses were measured for bend radii of 500 μm. Right-angle corner mirrors were fabricated at the outputs of the waveguides to minimize space needed to perform a 90° bend. The corner mirror losses were measured to be 1.5 ±0.4 dB.

Silicon MEMS techniques were developed to fabricate both single-shank and multi-shank probe geometries with integrated waveguides. The single-shank probes had waveguides with an input pitch of 250 μm and shank pitch of 10 μm. The multi-shank probes had an input pitch of 300 μm and a shank pitch of 10 μm. Methods were developed to assemble the multi-shank probes into a 3D format, using a baseplate holder and two alignment pieces. The final structure was measured to have multi-shank probes at 0.9 ± 0.3 degrees relative to the baseplate.

Three coupling schemes were developed to couple light to both single- and multi-shank probes. For individual probes not assembled in a 3D format, ribbon cables were used. Modular connection schemes were developed based on MTP-based technologies. Input coupling losses were measured to be 3.4 ± 2.2 dB. For probes which are assembled in a 3D format, two methods were developed: DMD-based and galvanometer-based. The losses associated with the DMD-based system were 17.3 ± 1.8 dB. With a 1.5W 473 nm laser source, 100 μW is capable of being delivered from 300 separate waveguides. The losses

associated with the galvanometer-based system were 11.9 ± 2.5 dB. With a 1.6 mW 473 nm laser source, 100 μW is capable of being delivered from a waveguide. Fiber bundles were characterized and their inherent disadvantages discussed.

Finally, initial neuroscience experiments were performed on microbial-opsin expressing mice.

6.2.2. Recommendations and Future Directions

The technology developed performed with the necessary performance characteristics outlined in Chapter 2. With that said, there are many improvements which can be made. This is an important function of this dissertation: to not only develop the technology, but provide a launching-point from which fruitful future research can readily be conducted.

The most immediate aspect of the technology which can be improved upon is the image bundle, or, more specifically, its removal. As discussed previously, as only a minor subset of the image bundle is being utilized, the vast majority of the fibers are wasted. This is detrimental both from an optical performance standpoint as well as a biological standpoint. In moving to a much smaller fiber array with regular spacing where each fiber correlates to an individual waveguide in the probe array, the coupling scheme will be greatly improved. For one, as the fibers would be regularly spaced, the coupling to the probe array would be greatly improved. Also, because the fiber count would be greatly reduced, the bulk of the connecting bundle would be correspondingly reduced. This could allow for, perhaps, freely-moving behavioral experiments.

A second potential improvement is with regards to the coupling scheme. Specifically, instead of taking an individual laser source and sculpting or redirecting it to individual waveguides, fabricate multiple chip-level laser sources each associated with an individual waveguide. Directly coupling an array of laser sources to the input apertures would eliminate the need for any connecting fiber optics, *and* it would avoid the heating issues involved with direct source implantation. With that said, having the light sources close to the brain may lead to unique heating issues. Recall the necessary source must be not-extended (a point source in nature). There are two source technologies relatively well developed which could potentially fit the necessary parameters: vertical-cavity surface-emitting lasers (VCSELs) and edge-emitting laser diodes. These sources could be fabricated in several ways. First, all the processing could be done on the appropriate III-V substrate. The laser diodes (VCSELs or edge-emitting) would first be fabricated and then the waveguide integrated in later steps. The main disadvantages to this option would be the need to adapt the already established waveguide processing flow and the high-cost associated with wasting so much expensive III-V substrate. The second option would be to fabricate linear arrays, or 2D arrays, of laser diodes and subsequently directly coupling those to the multi-shank probes or the entire probe array. Most likely, if arrays of edge-emitting diodes were to be used, then directly coupling to multi-shank probes would make the most sense, and if VCSEL arrays were to be used, then directly coupling to the entire probe array would make most sense. With that said, however, one could imagine hybrid technologies and integration schemes which would mix-and-match. The third and final option is to create pill-form laser diodes and further develop integration methods for integrating the diodes directly to the input regions.

As discussed previously, there are inherent issues with direct source implantation. However, if possible, there are powerful advantages to this approach. Most importantly, the connection to the probe array would be electrical in nature. The possibility of direct source implantation has been demonstrated with both simulation and empirical testing recently (Kim et al., 2013; McAlinden et al., 2013). The key to their success is careful control of delivery duty cycles. Although there are other potential issues with direct source implantation (inadvertent electrical stimulation, contamination of recording electrode, toxicity, etc.) it is worth noting there are sets of experiments subsequently made possible. In particular, because fiber optic coupling is a non-issue (see Chapter 5), and electrical power/signal connections are all that is necessary, it is the case that large-scale freely-moving optogenetics-based behavioral experiments would be made much easier. It will probably be the case, as these technologies develop, at least in the mid-term time-scale, that one technology will not satisfy all delivery and experimental paradigms. Given a certain scale, desired illumination paradigm, etc., one particular technology will have its advantages and disadvantages. The finite-element model developed in Chapter 2 can be used to quantitatively assess whether source implantation is a possibility, and, if so, what restrictions are placed on delivery power, frequency, duty cycle, etc.

Although abandoned towards the beginning of this project, there are some strong advantages to using polymer-based waveguides. There is a series of research demonstrating the extent to which scar tissue forms around neural implants is governed by the mismatch between the Young's modulus of the implant and the modulus of tissue (Polikov et al., 2005). Although not yet conclusive, if this proves to be true, polymers tend to have a lower modulus, and would therefore induce less damage at equivalent spatial scales.

What have been presented in this chapter are logical next steps for this technology in the context of neuroscience. However, there are several potentially synergistic technological applications worth mentioning which are outside of the scope of the applications immediately considered in this thesis. First, as was alluded to in Chapter 3, there is the possibility of optical detection using these waveguide arrays. With fluorescent tagging of neural activity, the optical waveguides could act to collect light from deep-brain targets, engendering a way of acquiring optical readout of electrical activity. There is also the possibility of using optical-electrical layers at the waveguide output as a transducer materials, again engendering optical readout of electrical activity (however, without the advantages of genetic targeting). There is also research being done on implanting photodiode arrays into fluorescently-tagged neural tissue for, opto-electrical decomposition and readout (Henninger, 2011). This technology requires a fluorescence illumination source to function. The waveguide arrays presented in this thesis could either be integrated with the photodiode arrays in the fabrication steps or the assembly steps. Spatial control of illumination provides an extra degree of freedom allowing for easier decomposition of neural activity. Furthermore, any application where illumination of deep tissue targets (organs, tumors, etc.) with 3D resolution is desirable (for the purposes of imaging, heating, stimulating, lesioning, etc.) could benefit from this work.

Appendix A: Detailed fabrication flow for on-chip waveguides

The following is a detailed fabrication flow for the waveguide fabrication (all the way through to single- or multi-shank probe fabrication). All tools used are a part of MIT's Microsystems Technology Laboratory (MTL).

(1) Clean virgin SOI wafers w/ 8 min piranha and 90 sec 50:1 HF dip

(2) 3um oxide on concept1 (PECVD tool)

(3) 10um oxynitride (pz-az 5um oxynitride) on concept1

(4) Mask1 (waveguides) pattern thick resist (HMDS(3), static dispense, spread at 1.5k for 9sec, spin at 2k for 60sec, prebake on hotplate1 for 3min at 110c, expose 5s X 4reps X 5sec break, develop in 300MIF for 3.5-4.5 min, postbake in 95C oven for 30min). It is important that the separation between waveguides be at least 3um on the mask; any less and the resist will not clear. Make sure trenches are clear here.

(5) AME (oxide/nitride etching tool) etch for eleven-twelve 5min etch cycles w/ original ZORZOS recipe (monitor and look for steady decrease of 5 points per 50 seconds which levels off when done). Obvious when clear with visual inspection. Check that trench bottom is at nearly same height as silicon substrate.

(6) Piranha for 8min (some PR film remained on sidewalls).

(7) ICL asher for 4min (clear).

(8) B3 @ 1000C for 3 hours. (nitrogen ambient anneal)

(9) 3um oxide on dcvd. ("OXIDE 3UM CHA") Start second wafer in parallel here. (PECVD)

(10) 500nm Ti on endura. (sputtering tool)

(11) Mask2 (pattern defining inputs and exits of waveguides) pattern double thick resist (*static dispense P4620 for ~60 sec, spread slowly <500rpm, let sit for 60 sec, spread at 1 kRPM for 60sec, 5kRPM for 10sec with cutip EBR, bake in 90C oven for 30min, repeat P4620 resist coating, bake in 90C oven for 60min, expose 7X15 sec w/ 15sec rest time and 80 um separation, develop in 405 until completely clear (~4-5 minutes, verify on fluoroscope), postbake in 90C oven for 30 minutes*)

(12) TRL weak asher for 1 min.

(13) Etch titanium in 1:1:20 HF:H2O2:H20 for 3 minutes (5kA should etch in 20-30 seconds, but overetch is for certainty)

(14) Strip thick resist in acetone/isopropanol

(15) Mask3 (halo pattern defining whole probe) pattern double thick resist (same recipe as before)

(16) Etch titanium in same manner as before

(17) Etch bottom oxide in 1:7 BOE solution for 20minutes (verify with indicator region, look for uniform/smooth silver-blue color)

(18) Leave frontside thick PR on

(19) Descum and etch on sts tool. Any of the main etch recipes will work.

(20) Leave frontside PR on.

(21) Mask4 (backside opening to thin probes) pattern double thick resist on backside (same recipe as before).

(22) Attach wafer to Si handle at 2kRPM resist spreading (share postbake of resist with mount curing)

(23) Etch in sts using jbetch recipe (do not be afraid to use SF614 to clear up black silicon because of the substantial oxide stop layer). Or whatever recipe is working.

(24) HF (49%) vapor etch BOX layer for 10 min. Distance between wafer and HF layer: 2cm (tape width).

(25) Release/clean in acetone/microstrip.

Appendix B: Detailed fabrication flow for ITO electrodes

Although still in development, the following is the most recent form of the ITO electrode (light proof electrode fabrication).

Start with wafer coated w/ ITO. Current stack: Si wafer/3um oxide(concept1)/~300nm ITO.

1) Pattern AZP4620 resist mask (ITO patterning)
    - HMDS recipe 3
    - Static dispense, spread at 1500 rpm for 9sec, level at 3K for 60sec, followed by mechanical EBR w/ cutip (EBR optional)
    - Prebake at 90C in convection oven for 60min
    - Expose for 16sec on EV-LC (wait for wafers to cool slightly before putting on aligner chuck)
    - Develop in AZ440 developer until clear, ~2.5-3.5min (shallow bath to increase shear velocity)
    - Hardbake in 95C convection oven for 30min (depending on nature of following etch)
2) Etch ITO on plasmaquest using recipe ITOETCH.rcp. (H2:15, CH4: 5, Ar: 20 ,7 mT, ECR: 275 ,RF:50, Temp: 80C). Start w/ 11 min etch and move up until clear. Verify clear with probe station impedance measurement. Inspect on microscope and fluoroscope. At this point, the photoresist is rather severely burnt. I also notice a

"puffing of the resist." (read notes, feb 1, 2011, for discussion as to why this is a problem)

3) Overnight soak in Microstrip. Stack wafers on carrier. When complete, sonicate on 9 for five minutes in fresh bath of Microstrip. Rinse thoroughly in DI and N2 dry. Inspect under microscope and fluoroscope.
4) Nanostrip treatment to remove remaining resist. 5 minute soak in nanostrip. DI rinse and dry. Inspect under microscope and fluoroscope.
5) Deposit 800nm SiO2 on STSCVD. Use HFSIO recipe for 12min48sec (N20:1420,N2:390,SiH4:10,platen:300C,showerhead:250C,50W @ 13.56 MHz, 900 mT).
6) Pattern AZP4620 resist mask (electrode via and contact pad)
    - HMDS recipe 3
    - Static dispense, spread at 1500 rpm for 9sec, level at 3K for 60sec, followed by mechanical EBR w/ cutip (EBR optional)
    - Prebake at 90C in convection oven for 60min
    - Expose for 16sec on EV-LC (wait for wafers to cool slightly before putting on aligner chuck)
    - Develop in AZ440 developer until clear, ~3-5min (shallow bath to increase shear velocity)
    - Hardbake in 95C convection oven for 30min (depending on nature of following etch)
7) Etch top oxide on plasmaquest using ARMAN.rcp (O2:5,He:15,CF4:40,ECR:200W,RF:__,Temp:25C). Start with assumed ~80nm/min

etch rate (11min etch), and move up in 1 min increments. Verify with microscope and probe station.

8) Strip AZ4620 resist. Overnight soak in Microstrip. Stack wafers on carrier. When complete, sonicate on 9 for several minutes in fresh bath of Microstrip. Rinse thoroughly in DI and N2 dry. Verify strip with microscope and fluoroscope.

9) Pattern AZ5214 resist mask (for gold liftoff)

   - Dynamic dispense (500 rpm for 6sec), spread at 750 rpm for 6sec, level at 3K for 30sec, followed by mechanical EBR w/ cutip (EBR optional)
   - Prebake on hotplate1 at 80C for 5min (make sure in thermal conductive contact)
   - Expose for 1.5sec on EV-LC (wait for wafers to cool slightly before putting on aligner chuck)
   - Bake on hotplate1 at 105C for 2 min
   - Flood expose for 60sec on EV-LC
   - Develop in AZ422 developer for ~1-1:30 (shallow bath to increase shear velocity)

10) Deposit 15nm Ti, 150nm Au on EbeamFP.

11) Soak in acetone for 4-5 hours (or overnight). Squirt away as much metal as possible in original bath. Sonicate in fresh acetone 1-2 min, followed by sonication in fresh isopropanol 1-2 min. DI rinse and dry.

12) Pattern AZP4620 double-thick resist mask (probe halo)

   - HMDS recipe 3

- First coat-Static dispense, level at 1000 rpm for 60sec, EBR at 5K for 10sec
- Bake at 90C in convection oven for 30min
- Second coat-Static dispense, level at 1000 rpm for 60sec, EBR at 5K for 10sec
- Bake at 90C in convection oven for 60min
- Expose for 7X15sec w/ 15 sec rest on EV-LC (wait for wafers to cool slightly before putting on aligner chuck). 60um separation.
- Develop in AZ440 developer until clear, ~9min
- Hardbake in 95C convection oven for 30min (depending on nature of following etch)

13) Etch bottom oxide (3um) on plasmaquest using ARMAN.rcp (O2:5,He:15,CF4:40,ECR:200W,RF:__,Temp:25C). Start with assumed ~80nm/min etch rate (~40min etch), and move up in 4 min increments. Verify with microscope and probe station.

14) Assess whether there is enough resist left to etch Si for ~1-2 hours on STS1.

15) Etch in sts1 using MIT56 for 1-2 hours.

16) Pattern backside with double-thick P4620 resist.

17) Attach wafer to Si handle at 2kRPM resist spreading (share postbake of resist with mount curing)

18) Etch in sts using jbetch recipe (do not be afraid to use SF614 to clear up black silicon because of the substantial oxide stop layer). Or whatever recipe is working.

19) Release/clean in acetone/microstrip.

Appendix C: Experimental SOP for preliminary biological experiments

The following is the standard-operating-procedure followed for the preliminary intra-cortical experiments conducted in 46-2143A (written with the help of Tim Buschman):

1. Waveguide Fabrication
    1.1. Anthony Zorzos
2. Waveguide Assembly
    2.1. Anthony Zorzos
3. Waveguide Coupling
    3.1. Anthony Zorzos
    3.2. Copy calibration files to *C:\Anthony Zorzos\MATLAB\BSM\FiberArray*
4. Preparing for experiment:
    4.1. Restart computer at the beginning of the day.
    4.2. Restock supplies, check O2 level and ISO level.
5. Surgery
    5.1. Retrieve mouse
    5.2. Anatomical targets:
        5.2.1. S1, relative to Bregma
            5.2.1.1. A/P: -1.2 mm
            5.2.1.2. M/L: +3.2 mm
        5.2.2. S2, relative to Bregma
            5.2.2.1. A/P: +0.25 mm

5.2.2.2. M/L: +4.25 mm

5.2.3. M1, relative to Bregma

5.2.3.1. A/P:

5.2.3.2. M/L:

5.3. 1cc LRS SQ

6. Laser

6.1. Turn on main laser power. Warm up for 15 minutes before use.

6.2. Open Labview and run *LaserControl.vi* in folder *C:\Anthony Zorzos\LabView2011*

6.3. VI variables to change:

6.3.1. Physical Channels = Dev2/ao2

6.3.2. Waveform Type = Square Wave

6.3.3. Frequency = 1

6.3.4. Low Voltage = 0

6.3.5. High Voltage = 1.6

6.3.6. Duty Cycle (%) = 100

6.4. Run Labview VI and then stop program. Laser will remain on for rest of experiment (the 1.6V signal is maintained).

6.5. Close Labview (don't save when asked).

7. Insertion

7.1. Attach mouse to head-post holder (location marked).

7.2. Isoflurane

7.2.1. Ensure nose cone fits tightly around animals nose. No need to cover mouth.

7.2.2. ISO at 0.8-1% level to maintain anesthesia

7.2.3. O2 rate should be ~0.8-1.2 mmHg/min.

7.3. Bring waveguide and recording stage assemblies into position

7.3.1. Labeled position on table for magnetic bases

7.3.2. Approximate values for **waveguide**: ___angle of arm, ___ micrometer position, ___ height on 1" post)

7.3.3. Approximate values for **neuronexus**: ___angle of arm, ___ micrometer position, ___ height on 1" post)

7.4. Thorlabs software is used to move waveguide array and recording probes.

7.5. Bring tip of neuronexus probe to zero depth position

7.6. Insert waveguide array, targeting S1 (and surrounding regions)

7.6.1. Waveguide array should run parallel to horizontal meridian so that shanks within a comb lie along the A/P axes and shanks between combs are on the M/L axis.

7.6.2. Lower waveguide until the lowest shank is just at cortical surface.

7.6.3. Take photo for documentation.

7.6.4. Lower wave guide into cortex. Generally 0.05mm steps (adjusted under settings of Thorlabs software) with a velocity of ___ mm/s.

7.6.5. Target to span cortex with all shanks. Deepest penetration should be ~ 1mm (i.e. top waveguide at surface).

7.6.6. Verify visually waveguide array is fully inserted (or what portion is inserted). Visual verification can be aided by running delivery during insertion (see below).

7.6.7. Take photo for documentation.

7.7. Insert electrode probe to target M1

7.7.1. Depth depends on the type of electrode using.

7.7.1.1. Laminar electrodes should aim to span the cortex (i.e. highest point should be at surface).

7.7.1.2. Tetrode electrodes should target L4/L6, roughly 400-700 um from surface

7.7.1.3. Spiking activity is recorded with Intan software

8. Sotware Protocol for **Random Sequence**

8.1. Matlab

8.1.1. Restart MATLAB ('quit' and then re-open).

8.1.2. Change Matlab directory to folder *C:\Anthony Zorzos\MATLAB\BSM\FiberArray*

8.1.2.1. At command prompt type "cd('*C:\Anthony Zorzos\MATLAB\BSM\FiberArray*')"

8.1.3. Make sure calibration file is in this folder.

8.1.4. Run BSMGUI.

8.1.5. Load *LightArray_StimWhiteNoiseSinglePosition.xml* by clicking the browse button ('…'). File is in folder *C:\Anthony Zorzos\MATLAB\BSM\FiberArray*

8.1.6. Change subject name ('MouseN') where N is latest iteration.

8.1.7. Adjust save-filename by hitting enter in the blank field (this will cause it to auto-fill)

8.1.8. Adjust number of trials to 1400 (this might need to be changed for different light arrays; will give 7 instances of each possible pair of stimulation sites when Nsites = 200).

8.1.9. Set some user-defined variables by selecting from drop-down list (every time) and then filling in field below.

8.1.9.1. StimSites should be equal to the number of stimulation sites (currently 200)

8.1.9.2. GalvoFilename should be set to the file generated during calibration (see above) so that the laser is pointed correctly to each waveguide (currently file is '20121030').

8.1.10. Other user-defined variables should already be set correctly:

8.1.10.1. PrepareTime=500

8.1.10.2. LeadTime=.5

8.1.10.3. TrailTime=.25

8.1.10.4. TotalStimTime=1

8.1.10.5. PointStimTime=.006

8.1.10.6. GalvoOffsite=[-5 5]

8.1.10.7. MaxEncodeV=5

8.1.10.8. AORate=10000

8.2. Intan software

8.2.1. Verify that recording time is set to 999 minutes

8.2.2. Set name of recording file (e.g. 'mouseN_whitenoise') and make sure it is saving to correct location.

8.3. When ready, begin recording in Intan, **wait 10 seconds**, and then run state machine through Matlab.

8.4. When BSM is complete you should **wait at least 10 seconds** and then hit 'Stop' in Intan.

8.4.1. You can both pause and stop the Matlab program early if need-be. Be aware that stopping/pausing often takes a trial or two before being executed.

8.5. Make sure the BSM file generated by Matlab is copied to the same directory as the Intan data files.

9. Sotware Protocol for **Sequential Delivery**

9.1. Matlab

9.1.1. Restart MATLAB ('quit' and then re-open).

9.1.2. Change Matlab directory to folder *C:\Anthony Zorzos\MATLAB\BSM\FiberArray*

9.1.2.1. At command prompt type "cd('*C:\Anthony Zorzos\MATLAB\BSM\FiberArray*')"

9.1.3. Create the condition map file for the day.

9.1.3.1. Edit the file 'Galvo_SiteToV.m'

9.1.3.1.1. This can be done from command line by typing "edit('Galvo_SiteToV.m');"

9.1.3.1.2. Change the line "file_base = '20120808';" to the latest calibration file for the galvanometer (currently '20121030')

9.1.3.2. Run the command

"LightArray_StimLocFreq_CreateConditionMap([2 4 10 20 40], [1:Nsites])" where Nsites is the number of sites for the current lightarray (e.g. 200). Command should be run at command prompt in Matlab.

9.1.4. Update # of conditions in XML file

9.1.5. Run 'BSMGUI' at command prompt

9.1.6. Load *LightArray_StimLocFreq.xml* by clicking the browse button ('…'). File is in folder *C:\Anthony Zorzos\MATLAB\BSM\FiberArray*

9.1.7. Change subject name ('MouseN') where N is latest iteration.

9.1.8. Change save-filename by hitting enter in the blank field (this will cause it to auto-fill)

9.1.9. Adjust number of trials to 25 times the number of sites (so for 200 sites, this should be 5000).

9.1.10. User-defined variables should already be set correctly:

9.1.10.1. MinStims=10

9.1.10.2. StimWidth=5

9.1.10.3. AORate=10000

9.1.10.4. LeadTime=500

9.1.10.5. TrailTime=250

9.1.10.6. LaserV=1.6

9.1.10.7. EncodeMaxV=4.5

9.2. Intan software

9.2.1. Verify that recording time is set to 999 minutes

9.2.2. Set name of recording file (e.g. 'DATE_StimLocFreq') and make sure it is saving to correct location.

9.3. When ready, begin recording in Intan, **wait 10 seconds**, and then run state machine through Matlab.

9.4. When BSM is complete you should **wait at least 10 seconds** and then hit 'Stop' in Intan.

9.4.1. You can both pause and stop the Matlab program early if need-be. Be aware that stopping/pausing often takes a trial or two before being executed.

9.5. Make sure the BSM file generated by Matlab is copied to the same directory as the Intan data files.

10. Remove both probes. Let neuronexus probe soak in H_2O_2 overnight. Angle waveguide array into H_2O_2 for ~2min and remove…let dry.

11. Copy all files from day to processing computer via external hard drive.

12. Add directory to list in *D:\BSM\FiberArray\BatchProcessLightArray.m*. Alter *stim_num* and *shanks_per_comb* parameters accordingly.

13. Run *BathchProcessLightArray.m*.

14. When experiment complete, immerse array in peroxide solution for 2 minutes followed by immersion in ethanol (similar treatment for electrodes).

Appendix D: Light-proof Electrodes

One of the many advantages to using optogenetic stimulation over electrical stimulation is that it allows for simultaneous electrical recording. Electrical stimulation overwhelms local recording electrodes and consequently cannot be used. Local electrical recordings in an optically illuminated region of tissue, however, is not without complications. Specifically, there is known 'optical artifact,' whereby an artificial signal is generated in response to pulsed illumination (Figure 77) (Han et al., 2011).

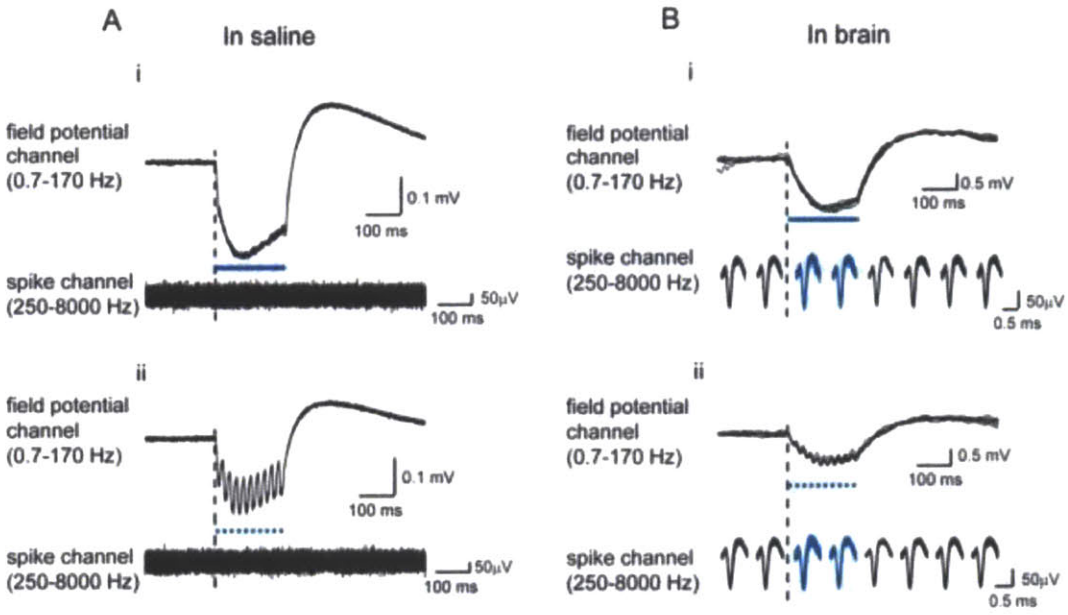

Figure 77 – Adapted from (Han et al., 2011), these traces show an optical artifact being induced in a tungsten electrode for pulsed 473 blue light (blue line). Notice the effect being filtered out at higher frequencies. See (Han et al., 2011) for detailed description of experimental setup.

As can be seen in Figure 77, in both a saline and brain medium, tungsten electrodes show optical artifacts in response to pulsed 473 nm illumination. The illumination irradiance is in ranges normally used in optogenetic experiments. Obviously, the superimposed artifact contaminates the electrical recording signal. Depending on the frequency of stimulation and frequency range of interest, this artifact may be able to be filtered out. There are frequency regimes, however, where this is not a possibility.

Several work-around solutions have been proposed over the last few years, including post-hoc subtraction of the artifact, distancing electrode and illumination field, and optically shielding the electrode. Although all these potential solutions have merit, and can be utilized for certain experimental situations, the solution we proposed involves avoiding the artifact altogether through the fabrication of 'light-proof' electrodes. The idea is simply: fabricate an electrode out of a material that has minimal interaction with light. The material we chose to purse was indium-tin-oxide (ITO). ITO is a transparent (in the visible regime) conductor used widely in the display industry (Rao, 2004). The transparency in the visible regime guarantees minimal light-interaction (i.e. light-proof), and the fact that it is electrically conductive makes it a potential electrode material.

This project is not complete and requires a certain amount of quantification and testing. This appendix simply serves as a summary of the problem, and a *qualitative* description of the solution path we've taken to-date. A description of what remains to be done will be presented.

The first step taken was already described: verify the presence of the optical artifact in saline and neural tissue for metal electrodes for standard irradiance values, pulse

durations and, and pulse frequencies. The second step was to fabricate simple ITO-based electrodes on glass and verify the complete absence of optical artifact. As the substrate and electrode are close to completely transparent (i.e. no light interaction), as was expected, the optical artifact was completely non-existent.

As glass is quite a difficult substrate to fabricate on (because of etching considerations), we moved to fabricating ITO electrodes on silicon. The electrodes were fabricated in a format similar to Michigan-style probes. Specifically, there were 16 electrode sites, each 20 μm squares and connected along 2 μm interconnects to large contact pads. No metal was used in this fabrication; the electrodes, interconnects, and contact pads were entirely made of ITO. A strong optical artifact, however, was measured. It became apparent that, although the ITO itself was not interacting with the illumination field, the silicon substrate was. Courtesy of Dr. Jorg Scholvin, who pointed out the dependence of hole-pair lifetime on silicon doping levels, we were able to eliminate the silicon substrate contribution to an optical artifact. Specifically, because higher silicon doping levels decrease hole-pair lifetime, and the optical artifact is most-likely due to hole-pair generation, by highly doping the silicon, the hole-pair lifetime is too slow to cause any significant effect.

The first neural recordings were done with the help of Mike Henninger, Giovanni T. Franzesi, and Suhasa Kodandaramaiah. The probes layout was identical to that described above. We were not able to successfully record single-unit with any of the ITO electrodes. Shown in Figure 78 is explanation as to why this was.

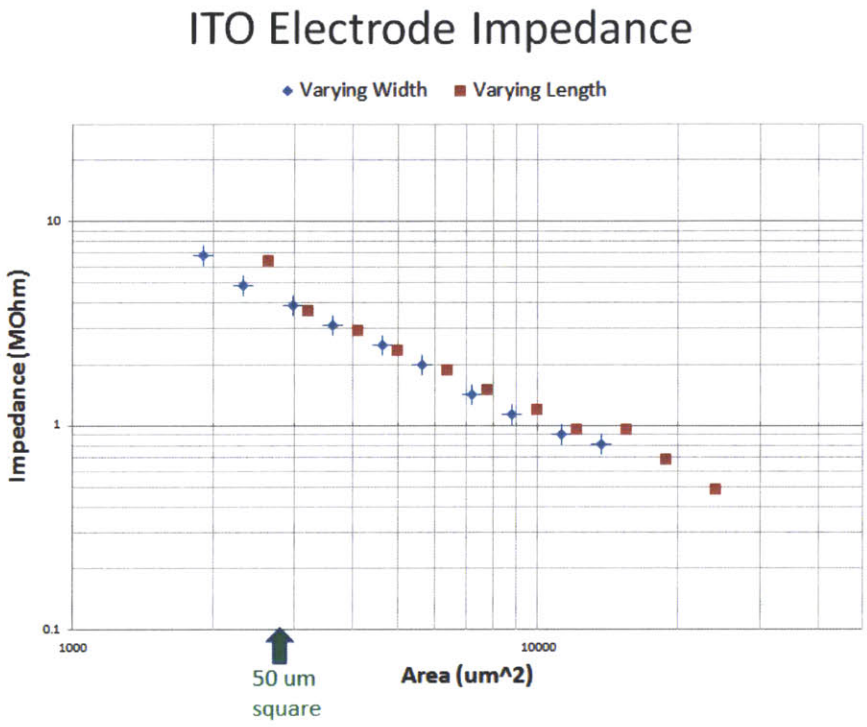

Figure 78 – Measurement of interface impedance for ITO electrodes in saline as a function of electrode area. Electrodes are rectangular; the width and length are being varied independently.

Figure 78 shows the measured impedance in saline for ITO electrodes of varying area, and it shows the measured impedance (at 1000 Hz) associated with a 50 μm square is ~7 MOhm. It can be inferred that the impedance for a 20 μm square is well in excess of 10 MOhm. It is a well-known principle of neural recordings that the impedance of electrodes should not exceed ~3 MOhm. As the Johnson-noise is impedance dependent (increases with

impedance), at impedances above ~3 MOhm the signal-to-noise ratio becomes too low to isolate high-frequency single-unit activity (Lempka et al., 2011). Obviously, the electrode impedance is dependent on size. Making the electrode larger will lower the impedance. However, if it is too large, the electrode will not be able to decipher individual neural events. Therefore, there are some materials which simply cannot provide the necessary impedance values for a given size electrode. The ITO film we were working with seemed to fit that category. Therefore, we decided to fabricate a probe where at each recording site there was an ITO electrode for light-proof low-frequency-potential (LFP) electrical recordings *and* a metallic (gold) electrode for recording higher frequency single unit activity (Figure 79).

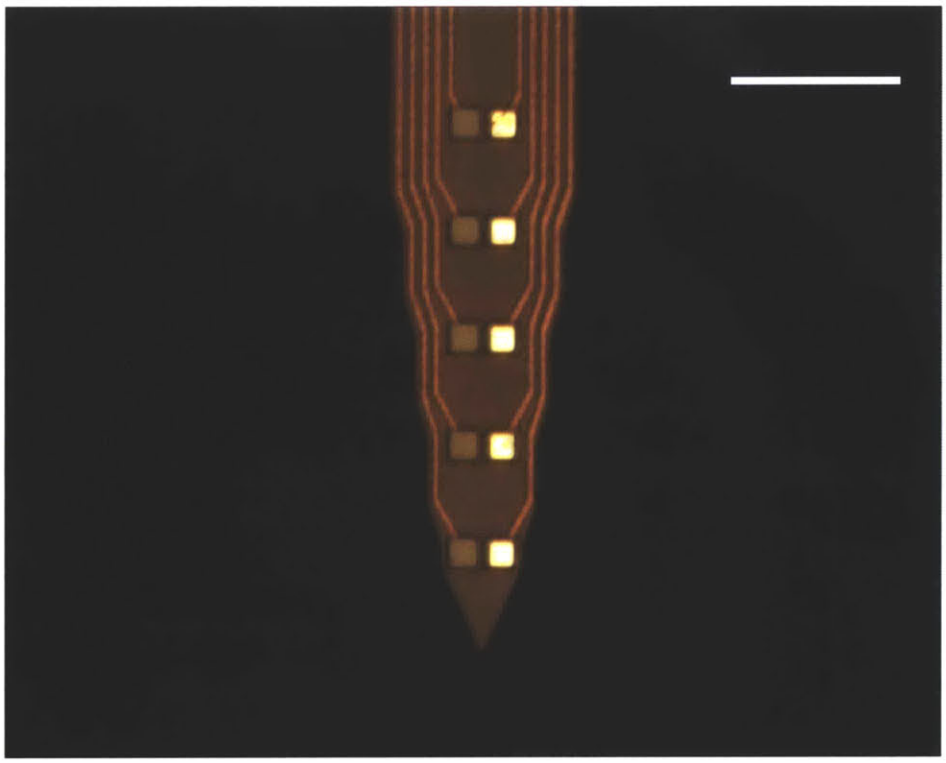

Figure 79 – Micro-electrode array with ITO and gold electrode pads at each recording site. Each electrode 20 µm square. Vertical pitch of 60 µm. Scale bar: 80 µm.

The ITO electrode provides optical artifact-free LFP electrical recordings, and the gold pad provides the recording of high-frequency neural spikes where the optical artifact can be frequency filtered out. Figure 80 shows both the single-unit activity recordings of the gold electrode (above) and the LFP activity of the ITO electrode (below).

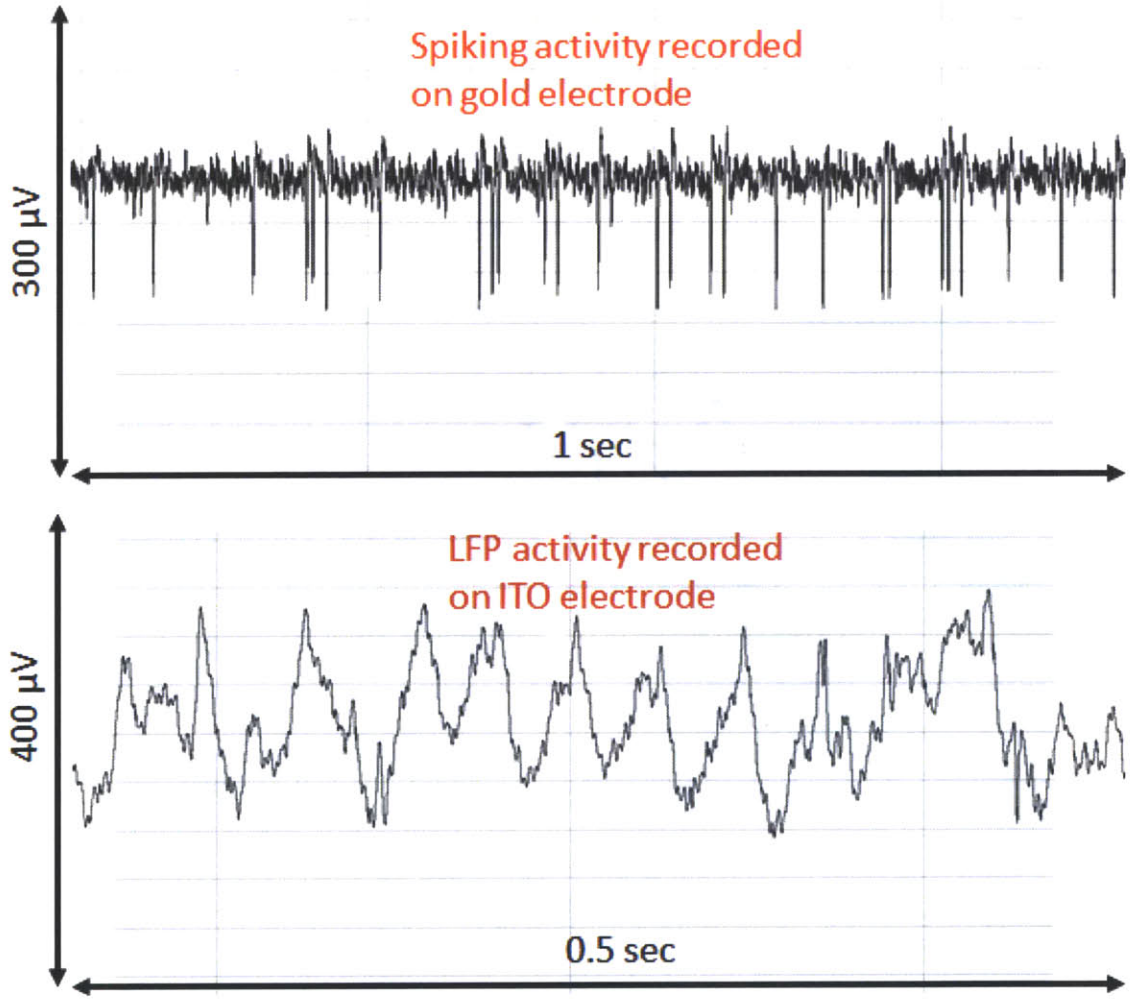

Figure 80 – Above: example single-unit activity recordings using gold electrode. Below: example LFP electrical activity recordings using ITO electrode.

As stated this is a highly preliminary study being *qualitatively* presented and there is a great deal of work remaining to be done. First, a set of quantitative measurements of the optical artifact for electrodes of various material compositions on various substrates for different powers, wavelengths, and pulse durations should be conducted. Second, a study of impedance characteristics of ITO films of different composition and doping levels should be conducted. This may reveal a regime of ITO compositions which provide an acceptable balance of transparency and surface impedance characteristics so that gold electrode sites could be avoided. In parallel, a study on various fabrication-based optical shielding methods (Dr. Jorg Scholvin) can be pursued. Finally, perhaps there are other transparent conductors which may serve the purposes of this project better. ITO was chosen because it is the most common transparent conductor, however other choices may be superior, such as zinc oxide, carbon nanotube films, or PEDOT.

Bibliography

Abdolvand, R., & Ayazi, F. (2008). An advanced reactive ion etching process for very high aspect-ratio sub-micron wide trenches in silicon. *Sensors and Actuators a-Physical, 144*(1), 109-116. doi: DOI 10.1016/j.sna.2007.12.026

Agrawal, G. P. (2010). *Fiber-optic communication systems* (4th ed.). New York: Wiley.

Almeida, V. R., Barrios, C. A., Panepucci, R. R., & Lipson, M. (2004). All-optical control of light on a silicon chip. *Nature, 431*(7012), 1081-1084. doi: Doi 10.1038/Nature02921

Andersen, P., & Moser, E. I. (1995). Brain temperature and hippocampal function. *Hippocampus, 5*(6), 491-498. doi: DOI 10.1002/hipo.450050602

Aravanis, A. M., Wang, L. P., Zhang, F., Meltzer, L. A., Mogri, M. Z., Schneider, M. B., & Deisseroth, K. (2007). An optical neural interface: in vivo control of rodent motor cortex with integrated fiberoptic and optogenetic technology. *Journal of Neural Engineering, 4*(3), S143-S156. doi: Doi 10.1088/1741-2560/4/3/S02

Archard, D., Giles, K., Price, A., Burgess, S., & Buchanan, K. (2010). Low Temperature PECVD of Dielectric Films for TSV Applications. *2010 Proceedings 60th Electronic Components and Technology Conference (Ectc)*, 764-768. doi: Doi 10.1109/Ectc.2010.5490746

Barkley, E. (2007). *he integration of InP /InGaAsP ridge waveguide structures with dielectric waveguides on silicon.*

Boyden, E. S. (2011). A history of optogenetics: the development of tools for controlling brain circuits with light. *F1000 Biol Rep, 3*, 11. doi: 10.3410/B3-11

Boyden, E. S., Zhang, F., Bamberg, E., Nagel, G., & Deisseroth, K. (2005). Millisecond-timescale, genetically targeted optical control of neural activity. *Nat Neurosci, 8*(9), 1263-1268. doi: 10.1038/nn1525

Buzsáki, G. (2006). *Rhythms of the brain*. Oxford ; New York: Oxford University Press.

Chow, B. Y., Han, X., Dobry, A. S., Qian, X., Chuong, A. S., Li, M., . . . Boyden, E. S. (2010). High-performance genetically targetable optical neural silencing by light-driven proton pumps. *Nature, 463*(7277), 98-102. doi: 10.1038/nature08652

Chung, S. J., Kim, K. S., Lin, T. C., Shen, Y. Z., Markowicz, P., He, G. S., & Prasad, P. N. (2002). Nanophotonics: Nanoscale optical interactions. *Molecular Crystals and Liquid Crystals, 374*, 59-66.

DeCusatis, C. (2008). *Handbook of fiber optic data communication : a practical guide to optical networking* (3rd ed.). Amsterdam ; Boston: Elsevier.

Denisse, C. M. M., Troost, K. Z., Habraken, F. H. P. M., Vanderweg, W. F., & Hendriks, M. (1986). Annealing of Plasma Silicon Oxynitride Films. *Journal of Applied Physics, 60*(7), 2543-2547. doi: Doi 10.1063/1.337118

DiLorenzo, D. J., & Bronzino, J. D. (2008). *Neuroengineering*. Boca Raton: CRC Press.

Elwassif, M. M., Kong, Q. J., Vazquez, M., & Bikson, M. (2006). Bio-heat transfer model of deep brain stimulation-induced temperature changes. *Journal of Neural Engineering, 3*(4), 306-315. doi: Doi 10.1088/1741-2560/3/4/008

Engel, A. K., Fries, P., & Singer, W. (2001). Dynamic predictions: oscillations and synchrony in top-down processing. *Nat Rev Neurosci, 2*(10), 704-716. doi: 10.1038/35094565

Espinola, R. L., Ahmad, R. U., Pizzuto, F., Steel, M. J., & Osgood, R. M. (2001). A study of high-index-contrast 90 degrees waveguide bend structures. *Opt Express, 8*(9), 517-528.

Famenini, S. (2012). *Coaxial Recess Intergration Of InGaAs Edge Emitting Laser Diodes With Waveguides*

On Silicon Substrates: A Complete Solution To Laser Intergraion On IC.

Frontiers Research Foundation. (2008). Frontiers in neuroengineering.

Gradinaru, V., Mogri, M., Thompson, K. R., Henderson, J. M., & Deisseroth, K. (2009). Optical Deconstruction of Parkinsonian Neural Circuitry. *Science, 324*(5925), 354-359. doi: DOI 10.1126/science.1167093

Gramotnev, D. K., & Bozhevolnyi, S. I. (2010). Plasmonics beyond the diffraction limit. *Nature Photonics, 4*(2), 83-91. doi: DOI 10.1038/nphoton.2009.282

Han, X., & Boyden, E. S. (2007). Multiple-color optical activation, silencing, and desynchronization of neural activity, with single-spike temporal resolution. *PLoS One, 2*(3), e299. doi: 10.1371/journal.pone.0000299

Han, X., Chow, B. Y., Zhou, H., Klapoetke, N. C., Chuong, A., Rajimehr, R., . . . Boyden, E. S. (2011). A high-light sensitivity optical neural silencer: development and application to optogenetic control of non-human primate cortex. *Front Syst Neurosci, 5*, 18. doi: 10.3389/fnsys.2011.00018

Henninger, M. A. (2011). A novel concept for an implantable probe for deep-brain optical measurement of the activity of large populations of neurons.

Hong, G., Holmes, A. S., & Heaton, M. E. (2004). SU8 resist plasma etching and its optimisation. *Microsystem Technologies-Micro-and Nanosystems-Information Storage and Processing Systems, 10*(5), 357-359. doi: DOI 10.1007/s00542-004-0413-4

Hunsperger, R. G. (1991). *Integrated optics: theory and technology* (3rd ed.). Berlin ; New York: Springer-Verlag.

Jang, J. H., Zhao, W., Bae, J. W., Selvanathan, D., Rommel, S. L., Adesida, I., . . . Abeles, J. H. (2003). Direct measurement of nanoscale sidewall roughness of optical waveguides using an atomic force microscope. *Applied Physics Letters, 83*(20), 4116-4118. doi: Doi 10.1063/1.1627480

Jensen, W., Yoshida, K., & Hofmann, U. G. (2006). In-vivo implant mechanics of flexible, silicon-based ACREO microelectrode arrays in rat cerebral cortex. *IEEE Trans Biomed Eng, 53*(5), 934-940. doi: 10.1109/TBME.2006.872824

Johansson, J. D. (2010). Spectroscopic method for determination of the absorption coefficient in brain tissue. *J Biomed Opt, 15*(5), 057005. doi: 10.1117/1.3495719

Kandel, E. R. (2012). *Principles of neural science* (5th ed.). New York: McGraw-Hill.

Kasap, S. O. (2013). *Optoelectronics and photonics : principles and practices* (2nd ed.). Boston: Pearson.

Katz, B. F. (2008). *Neuroengineering the future : virtual minds and the creation of immortality*. Hingham, Mass.: Infinity Science Press.

Keiser, G. (2011). *Optical fiber communications* (4th ed.). New York, NY: McGraw-Hill Companies.

Kienle, A., Lilge, L., Patterson, M. S., Hibst, R., Steiner, R., & Wilson, B. C. (1996). Spatially resolved absolute diffuse reflectance measurements for noninvasive determination of the optical scattering and absorption coefficients of biological tissue. *Appl Opt, 35*(13), 2304-2314. doi: Doi 10.1364/Ao.35.002304

Kim, T. I., McCall, J. G., Jung, Y. H., Huang, X., Siuda, E. R., Li, Y., . . . Bruchas, M. R. (2013). Injectable, cellular-scale optoelectronics with applications for wireless optogenetics. *Science, 340*(6129), 211-216. doi: 10.1126/science.1232437

Kimura, S., & Takami, K. (1988). Photoresist Thickness Measurement Using Laser-Induced Fluorescence. *Appl Opt, 27*(17), 3675-3678.

Lee, K. K., Lim, D. R., Luan, H. C., Agarwal, A., Foresi, J., & Kimerling, L. C. (2000). Effect of size and roughness on light transmission in a Si/SiO2 waveguide: Experiments and model. *Applied Physics Letters, 77*(11), 1617-1619. doi: Doi 10.1063/1.1308532

Lempka, S. F., Johnson, M. D., Moffitt, M. A., Otto, K. J., Kipke, D. R., & McIntyre, C. C. (2011). Theoretical analysis of intracortical microelectrode recordings. *Journal of Neural Engineering, 8*(4). doi: Artn 045006

Doi 10.1088/1741-2560/8/4/045006

Lin, Y. B., Lin, J. S., Chen, R. S., & Li, C. R. (2009). Design of High Transmission Broadband 90-Degree Bend by Reducing Field Mismatch at Corner for Two Dimensional Cubic Photonic Crystals. *Aoe 2008: Asia Optical Fiber Communication and Optoelectronic Exposition and Conference.*

London, J. M., Loomis, A. H., Ahadian, J. F., & Fonstad, C. G. (1999). Preparation of silicon-on-gallium arsenide wafers for monolithic optoelectronic integration. *Ieee Photonics Technology Letters, 11*(8), 958-960. doi: Doi 10.1109/68.775312

Ma, H., Jen, A. K. Y., & Dalton, L. R. (2002). Polymer-based optical waveguides: Materials, processing, and devices. *Advanced Materials, 14*(19), 1339-1365. doi: Doi 10.1002/1521-4095(20021002)14:19<1339::Aid-Adma1339>3.0.Co;2-O

Madisen, L., Mao, T., Koch, H., Zhuo, J. M., Berenyi, A., Fujisawa, S., . . . Zeng, H. (2012). A toolbox of Cre-dependent optogenetic transgenic mice for light-induced activation and silencing. *Nat Neurosci, 15*(5), 793-802. doi: 10.1038/nn.3078

Madou, M. J. (2012). *Fundamentals of microfabrication and nanotechnology* (3rd ed.). Boca Raton, FL: CRC Press.

Marcuse, D. (1976). Curvature Loss Formula for Optical Fibers. *Journal of the Optical Society of America, 66*(3), 216-220. doi: Doi 10.1364/Josa.66.000216

Maurits, N. M. (2012). From neurology to methodology and back an introduction to clinical neuroengineering. from http://dx.doi.org/10.1007/978-1-4614-1132-1 MIT Access Only

McAlinden, N., Massoubre, D., Richardson, E., Gu, E., Sakata, S., Dawson, M. D., & Mathieson, K. (2013). Thermal and optical characterization of micro-LED probes for in vivo optogenetic neural stimulation. *Opt Lett, 38*(6), 992-994. doi: 10.1364/OL.38.000992

Michael, A. C., & Borland, L. M. (2007). *Electrochemical methods for neuroscience*. Boca Raton: CRC Press/Taylor & Francis.

Miller, E. K., & Buschman, T. J. (2013). Cortical circuits for the control of attention. *Curr Opin Neurobiol, 23*(2), 216-222. doi: 10.1016/j.conb.2012.11.011

Nishi, H., Tsuchizawa, T., Watanabe, T., Shinojima, H., Yamada, K., & Itabashi, S. (2010). Compact and Polarization-Independent Variable Optical Attenuator Based on a Silicon Wire Waveguide with a Carrier Injection Structure. *Japanese Journal of Applied Physics, 49*(4). doi: Artn 04dg20

Doi 10.1143/Jjap.49.04dg20

Nyborg, W. L. (1988). Solutions of the Bio-Heat Transfer Equation. *Physics in Medicine and Biology, 33*(7), 785-792. doi: Doi 10.1088/0031-9155/33/7/002

Offrein, B. J., Germann, R., Bona, G. L., Horst, F., & Salemink, H. W. M. (1998). Tunable optical add/drop components in silicon-oxynitride waveguide structures. *24th European Conference on Optical Communication, Vol 1-3*, 325-326.

Oh, M. C., Chu, W. S., Kim, K. J., & Kim, J. W. (2011). Polymer waveguide integrated-optic current transducers. *Opt Express, 19*(10), 9392-9400.

Ohno, Y. (2004). Color rendering and luminous efficacy of white LED spectra. *Fourth International Conference on Solid State Lighting, 5530*, 88-98. doi: Doi 10.1117/12.565757

Oron, D., Papagiakoumou, E., Anselmi, F., & Emiliani, V. (2012). Two-photon optogenetics. *Optogenetics: Tools for Controlling and Monitoring Neuronal Activity, 196*, 119-143. doi: Doi 10.1016/B978-0-444-59426-6.00007-0

Paschotta, R. (2011). Fibers. *Rp-photonics.* from http://www.rp-photonics.com/fibers.html

PhotonicsOnline. from http://photonicswiki.org/index.php?title=File:Circular_dielect_wg.png

Polikov, V. S., Tresco, P. A., & Reichert, W. M. (2005). Response of brain tissue to chronically implanted neural electrodes. *Journal of Neuroscience Methods, 148*(1), 1-18. doi: DOI 10.1016/j.jneumeth.2005.08.015

Rao, K. N. (2004). Optical and electrical properties of indium-tin oxide films. *Indian Journal of Pure & Applied Physics, 42*(3), 201-204.

Rieke, F. (1997). *Spikes : exploring the neural code*. Cambridge, Mass.: MIT Press.

Ristic, S., Bhardwaj, A., Rodwell, M. J., Coldren, L. A., & Johansson, L. A. (2010). An Optical Phase-Locked Loop Photonic Integrated Circuit. *Journal of Lightwave Technology, 28*(4), 526-538. doi: Doi 10.1109/Jlt.2009.2030341

Sakai, S., Ueno, K., Ishizuka, T., & Yawo, H. (2013). Parallel and patterned optogenetic manipulation of neurons in the brain slice using a DMD-based projector. *Neurosci Res, 75*(1), 59-64. doi: 10.1016/j.neures.2012.03.009

Saleh, B. E. A., & Teich, M. C. (2007). *Fundamentals of photonics* (2nd ed.). Hoboken, N.J.: Wiley Interscience.

Seidemann, V., Rabe, J., Feldmann, M., & Buttgenbach, S. (2002). SU8-micromechanical structures with in situ fabricated movable parts. *Microsystem Technologies, 8*(4-5), 348-350. doi: DOI 10.1007/s00542-002-0171-0

Skorka, O., Meyler, B., & Salzman, J. (2004). Propagation loss in GaN-based ridge waveguides. *Applied Physics Letters, 84*(19), 3801-3803. doi: Doi 10.1063/1.1741025

Sunkin, S. M., Ng, L., Lau, C., Dolbeare, T., Gilbert, T. L., Thompson, C. L., . . . Dang, C. (2013). Allen Brain Atlas: an integrated spatio-temporal portal for exploring the central nervous system. *Nucleic Acids Research, 41*(D1), D996-D1008. doi: Doi 10.1093/Nar/Gks1042

Tian, P. F., McKendry, J. J. D., Gong, Z., Guilhabert, B., Watson, I. M., Gu, E. D., . . . Dawson, M. D. (2012). Size-dependent efficiency and efficiency droop of blue InGaN micro-light emitting diodes. *Applied Physics Letters, 101*(23). doi: Artn 231110

Doi 10.1063/1.4769835

Wentz, C. T., Bernstein, J. G., Monahan, P., Guerra, A., Rodriguez, A., & Boyden, E. S. (2011). A wirelessly powered and controlled device for optical neural control of freely-behaving animals. *Journal of Neural Engineering, 8*(4). doi: Artn 046021

Doi 10.1088/1741-2560/8/4/046021

Wong, H., Filip, V., Wong, C. K., & Chung, P. S. (2007). Silicon integrated photonics begins to revolutionize. *Microelectronics Reliability, 47*(1), 1-10. doi: DOI 10.1016/j.microlrel.2006.01.002

Worhoff, K., Klein, E., Hussein, G., & Driessen, A. (2008). Silicon oxynitride based photonics. *Icton 2008: Proceedings of 2008 10th Anniversary International Conference on Transparent Optical Networks, Vol 3*, 266-269.

Zamisel. Laser Scanners. 2013, from http://www.zamisel.com/SSpostavka2.html

Zhang, A. L., & Chan, K. T. (2003). Characterization of the optical loss of an integrated silicon oxynitride optical switch structure. *Applied Physics Letters, 83*(13), 2524-2526. doi: Doi 10.1063/1.1614416

Zhang, F., Aravanis, A. M., Adamantidis, A., de Lecea, L., & Deisseroth, K. (2007). Circuit-breakers: optical technologies for probing neural signals and systems. *Nat Rev Neurosci, 8*(8), 577-581. doi: 10.1038/nrn2192

Zhang, F., Wang, L. P., Brauner, M., Liewald, J. F., Kay, K., Watzke, N., . . . Deisseroth, K. (2007). Multimodal fast optical interrogation of neural circuitry. *Nature, 446*(7136), 633-639. doi: 10.1038/nature05744

Zorzos, A. N., Boyden, E. S., & Fonstad, C. G. (2010). Multiwaveguide implantable probe for light delivery to sets of distributed brain targets. *Opt Lett, 35*(24), 4133-4135. doi: 10.1364/OL.35.004133

Zorzos, A. N., Scholvin, J., Boyden, E. S., & Fonstad, C. G. (2012). Three-dimensional multiwaveguide probe array for light delivery to distributed brain circuits. *Opt Lett, 37*(23), 4841-4843. doi: 10.1364/OL.37.004841